Characterization tools on epitaxial growth control

Armando Lourenço
Universidade de Aveiro
June 2023

PVD (Physical Vapour Deposition) can be described using four stages

1º - Vapour phase creation

(Thermal, kinetic or electromagnetic energy transfer).

2º - Transport of the vapor to the substrate

3º - Film growth on the substrate

(Surface construction)

4º - Film Analysis

(*in-situ or ex-situ*)

- This is an empirical approach to the deposition process
- We can use it because it´s possible to create the conditions where these stages are weakly dependent on the others
- It´s easier to control the whole deposition process if we can isolate and treat as independent the fundamental parameters of each stage

Usually we classify the vapour phase creation in two main groups

- ***Thermal Evaporation***

  Materials are heated in vacuum until its pressure is higher than the environment pressure

  Ex: Evaporation, e-Beam evaporation, MBE (Molecular Beam Epitaxy)

- ***Sputtering***
  - **Ionic sputtering**: *high energy ions collide with a surface and sputter atoms from that surface*

    Ex: Diode, Magnetron, Ion-beam
  - **Laser sputtering (PLD, Laser Ablation)**: *high energy and very short* (~ 25 ns) *laser pulses are focused on a surface*

PLD – Pulsed Laser Deposition

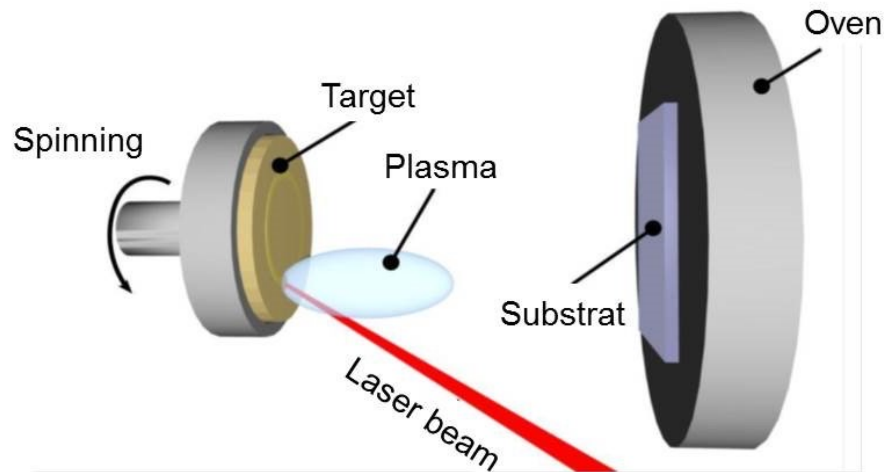

Laser pulse focused on target

- $\lambda = 246$ nm (Kr:F laser)
- $\Delta t \approx 25$ ns
- $F \approx 5 \ \mathrm{J/cm^2}$
- $P \approx 2{\times}10^8 \ \mathrm{W/cm^2}$

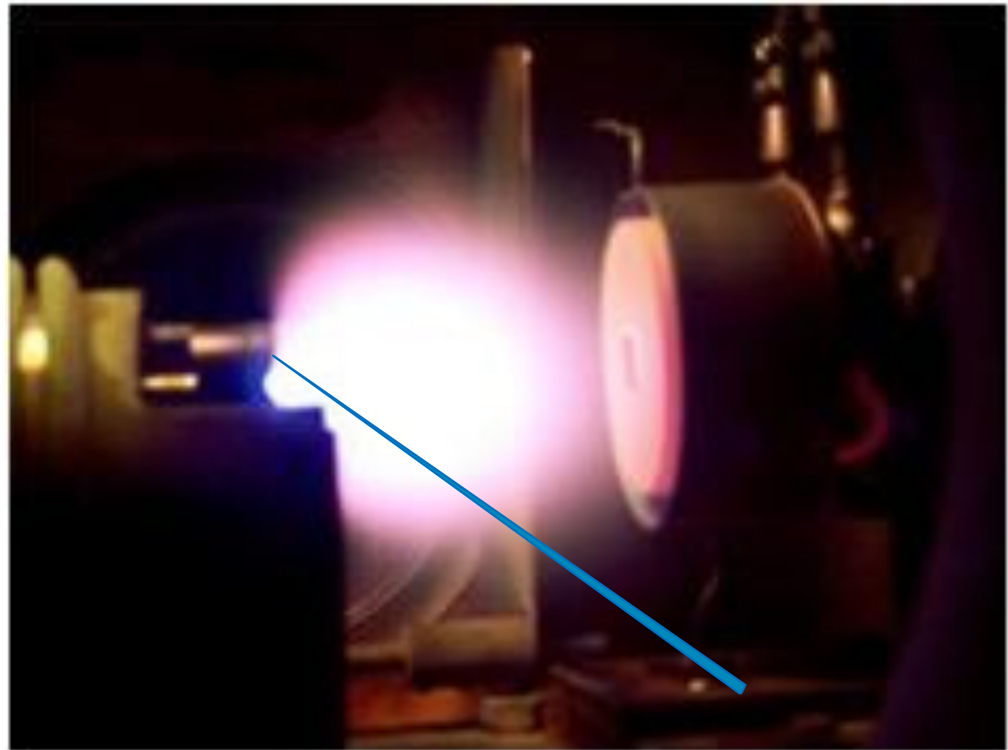

PLD – Pulsed Laser Deposition

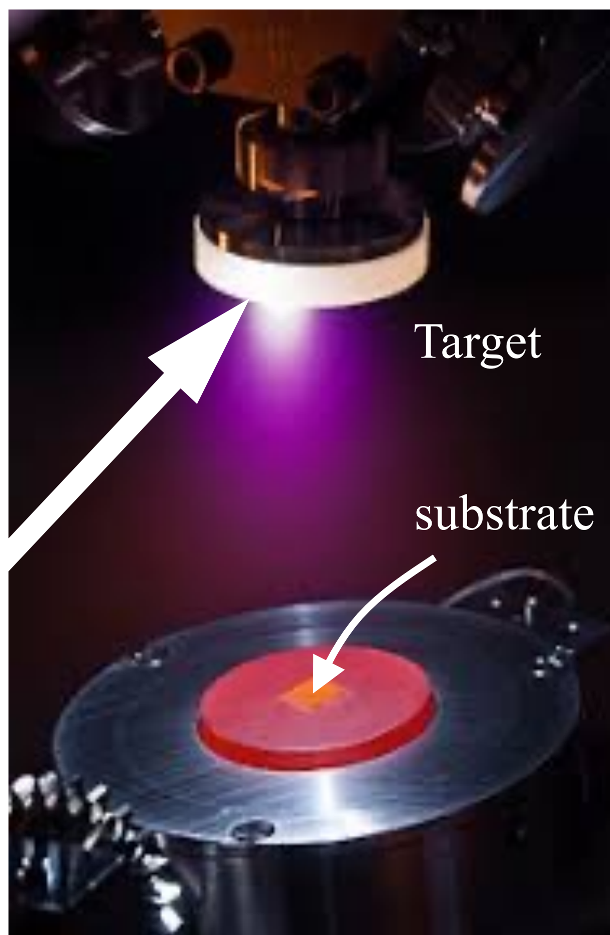

David B. Geohegan, *Appl. Phys. Lett.* **60**, 2732 (1992)

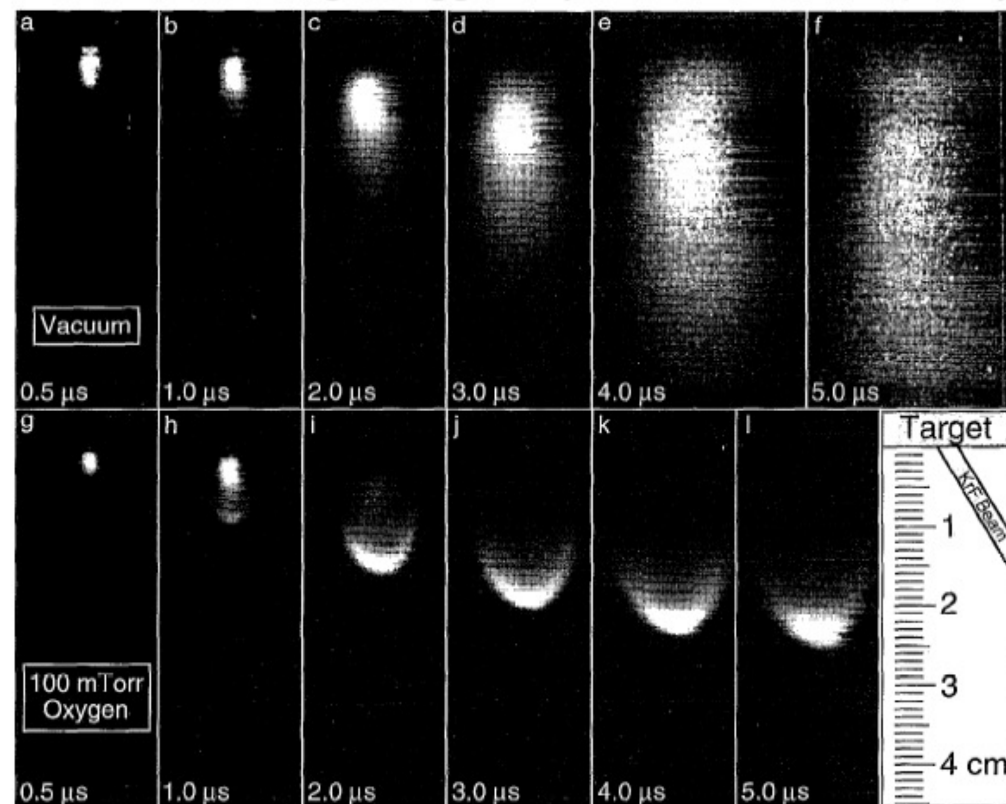

FIG. 1. ICCD photographs of the visible plasma emission (exposure times 20 ns) following 1.0 J cm^{-2} KrF/YBCO ablation into [(a)–(f)] 1×10^{-6} Torr and [(g)–(l)] 100 mTorr oxygen at the indicated delay times from the arrival of the laser pulse. The 0.2 cm×0.2 cm 248-nm laser pulse irradiated the YBCO target at an angle of 30° as shown.

Ionic sputtering

Ionic bombardment

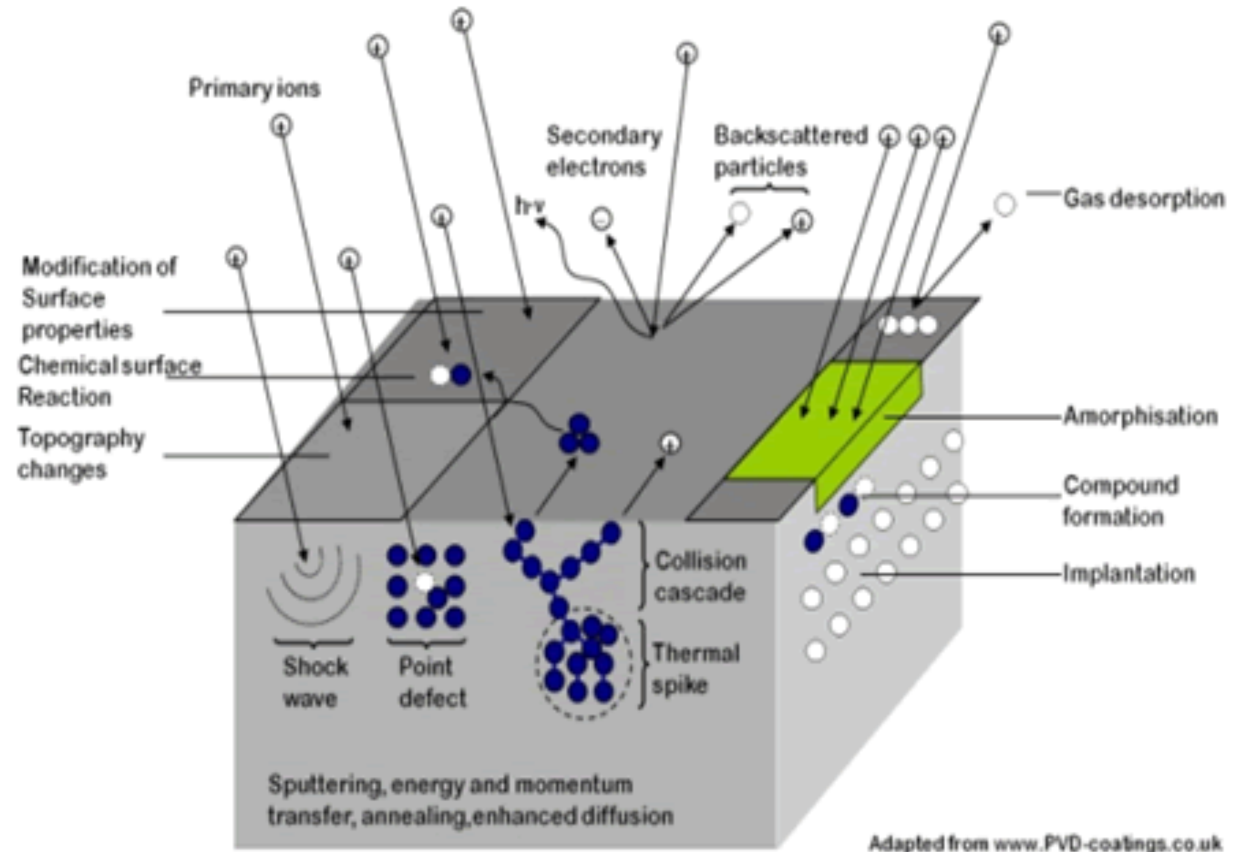

Ionic sputtering

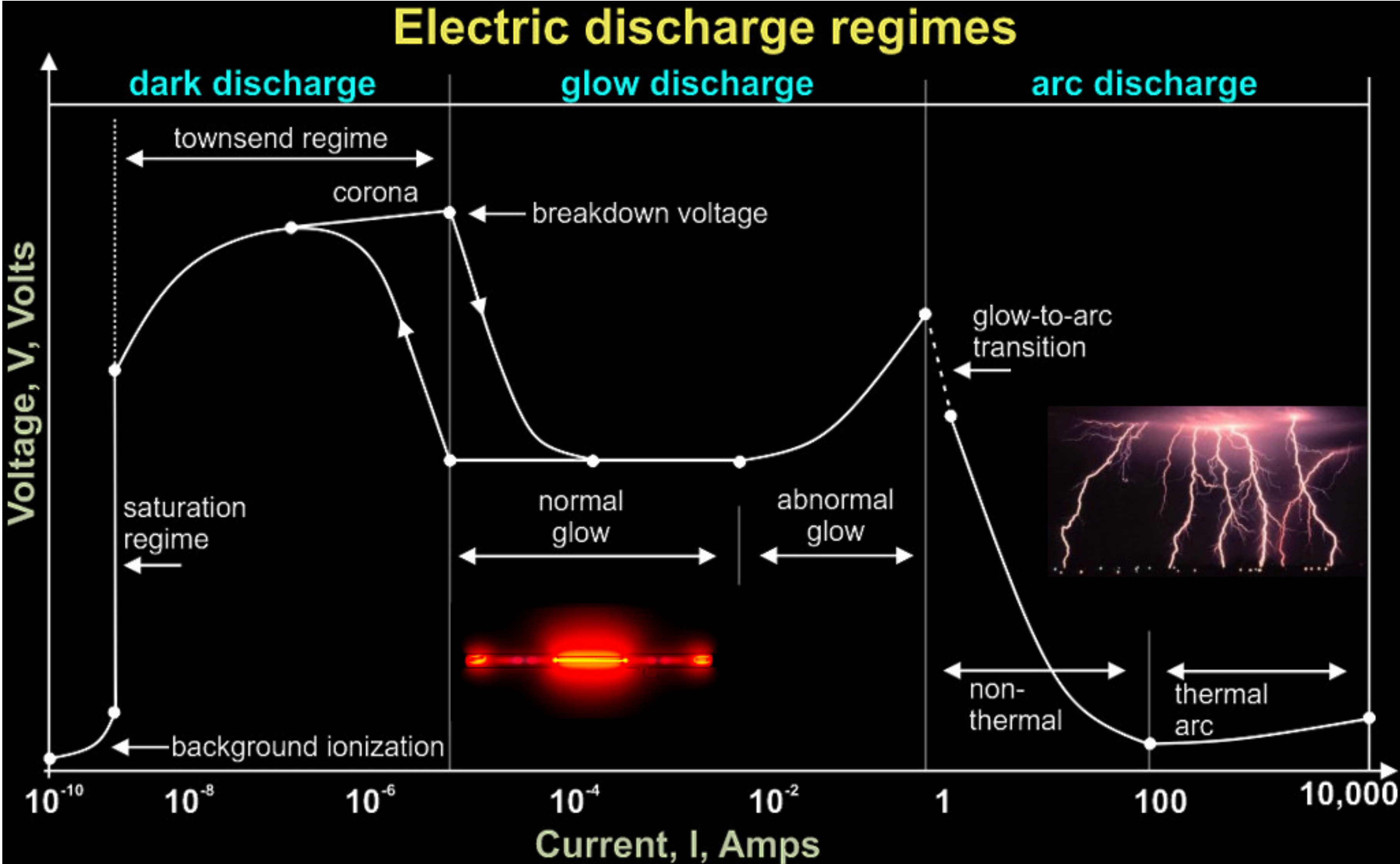

1. Vapour Phase
rf - Ionic sputtering

- We use 13,56 MHz to create a glow discharge in a low pressure gas (~10^{-3} mbar)
- To minimize unwanted chemical reactions we use a inert gas (Ar, Kr or Xe)
- Due to the much lower ion mobility, compered to electron mobility) the rf negative cycle is not neutralized ⇒ a negative voltage appears at the target surface ⇒ this is the accelerating potential needed for ionic bombardment
- *rf rectifying effect*
- *This means that we can sputter insulators as well as metals*

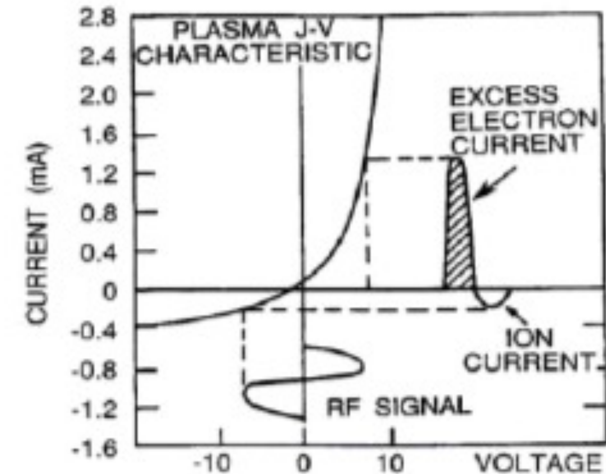

(a)

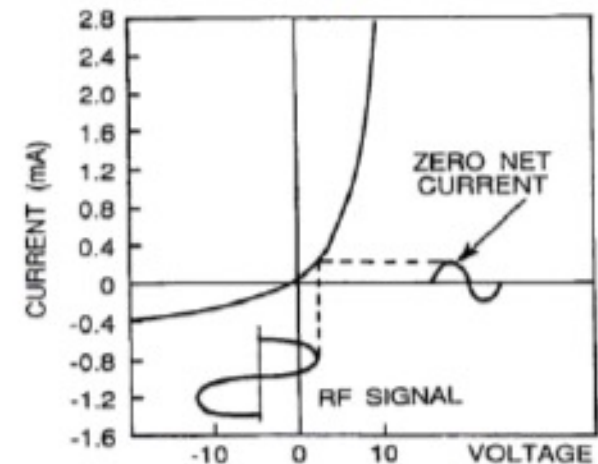

(b)

rf - Ionic sputtering

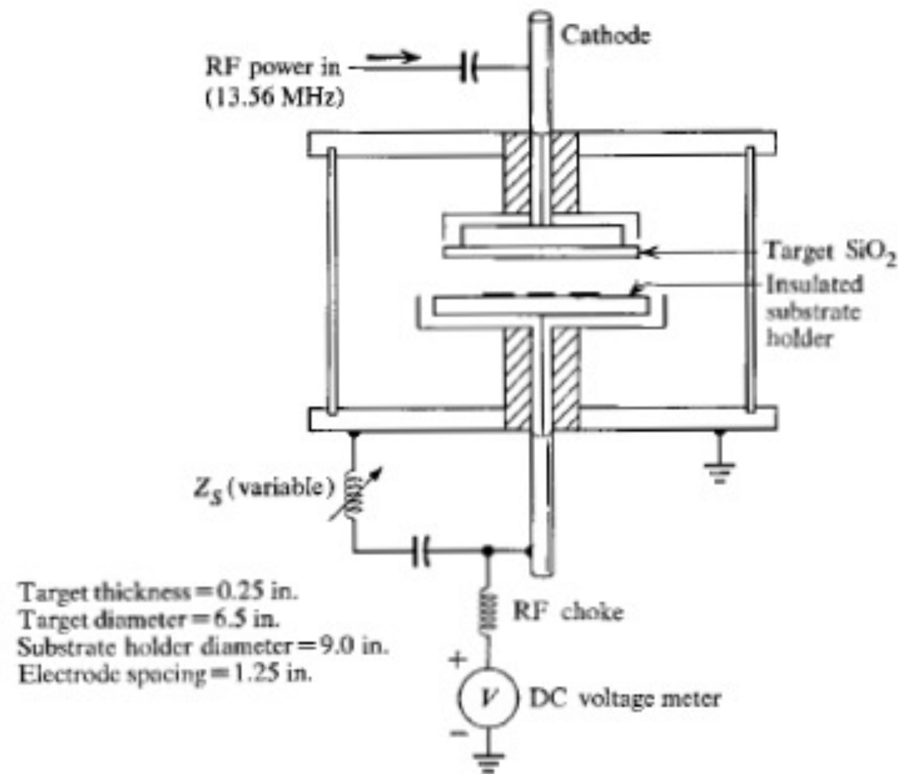

Figure 1 Experimental system for rf sputtering with substrate tuning.

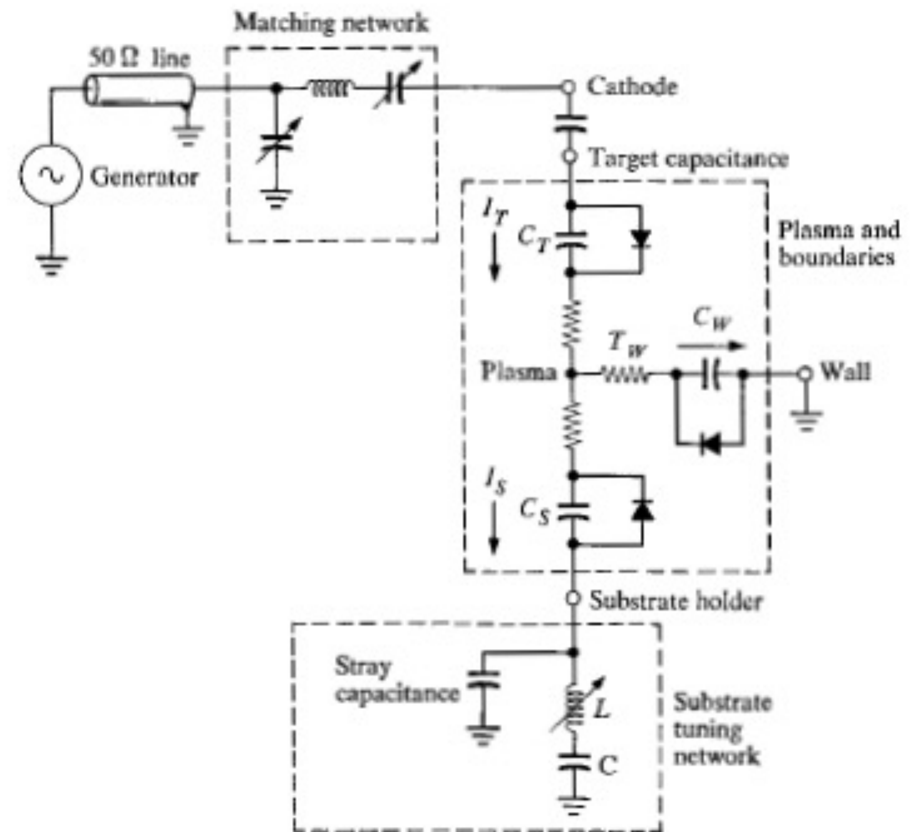

Figure 2 Electrical model for experimental system.

J.S. Logan, *IBM J. Res. Develop.*, March 1970

rf - Ionic sputtering – planar magnetron

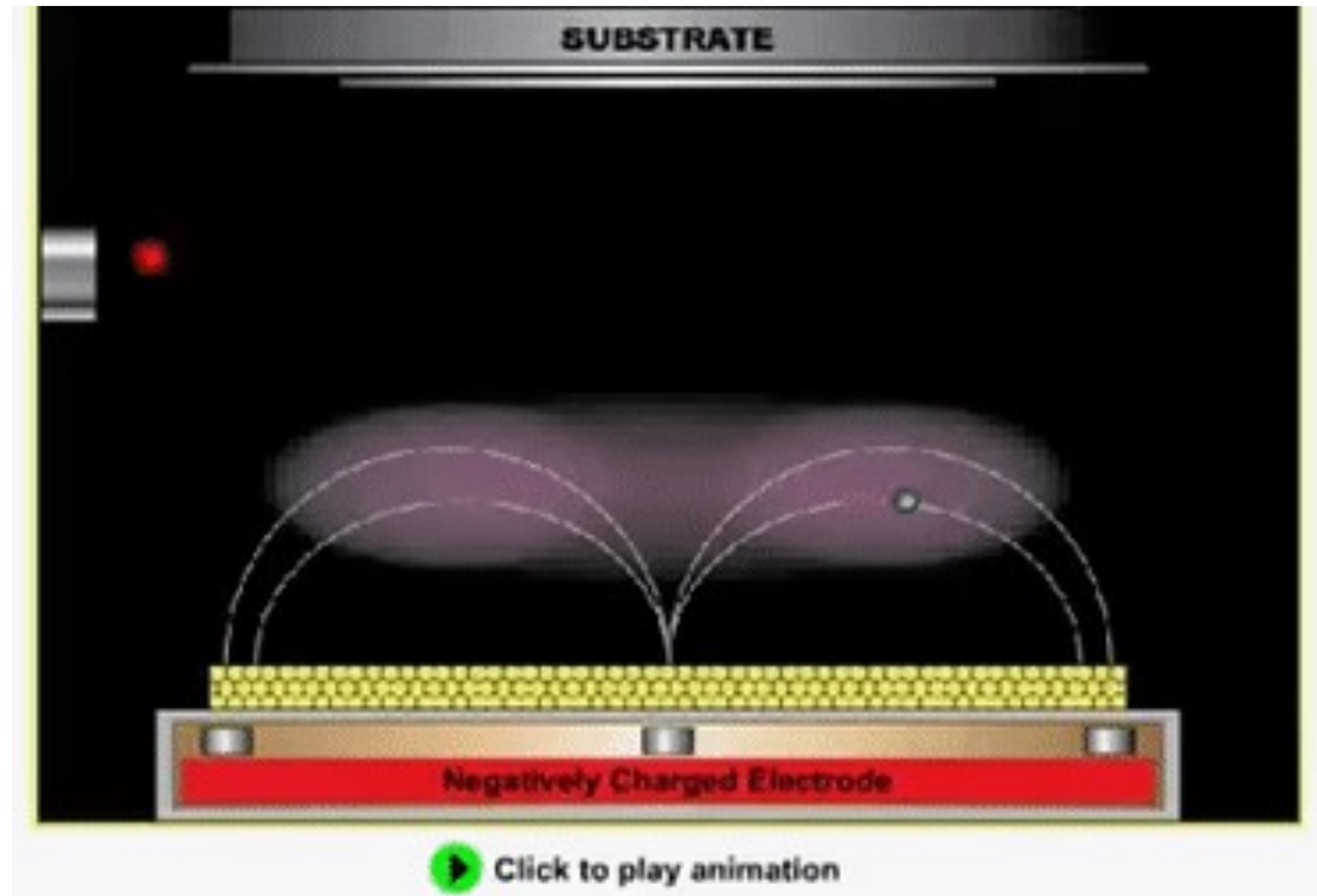

rf - Ionic sputtering

Sputtering yield

$$Y = \frac{emited\ particles}{incident\ ion} = \alpha \frac{Mm}{(M+m)^2} \frac{E_m}{U_M}$$

were M = *target atom mass*
m = *incident ion mass*
E_m = *ion kinetic energy*
U_M = *target binding energy*
α = *constant (geometry dependent)*

- *Sputtered atoms energy* ~ 30 - 40 eV
- *velocity* ~ 3 – 6 E5 cm/s
- *Co-deposition is possible*

1. Vapour Phase
rf - Ionic sputtering – planar magnetron

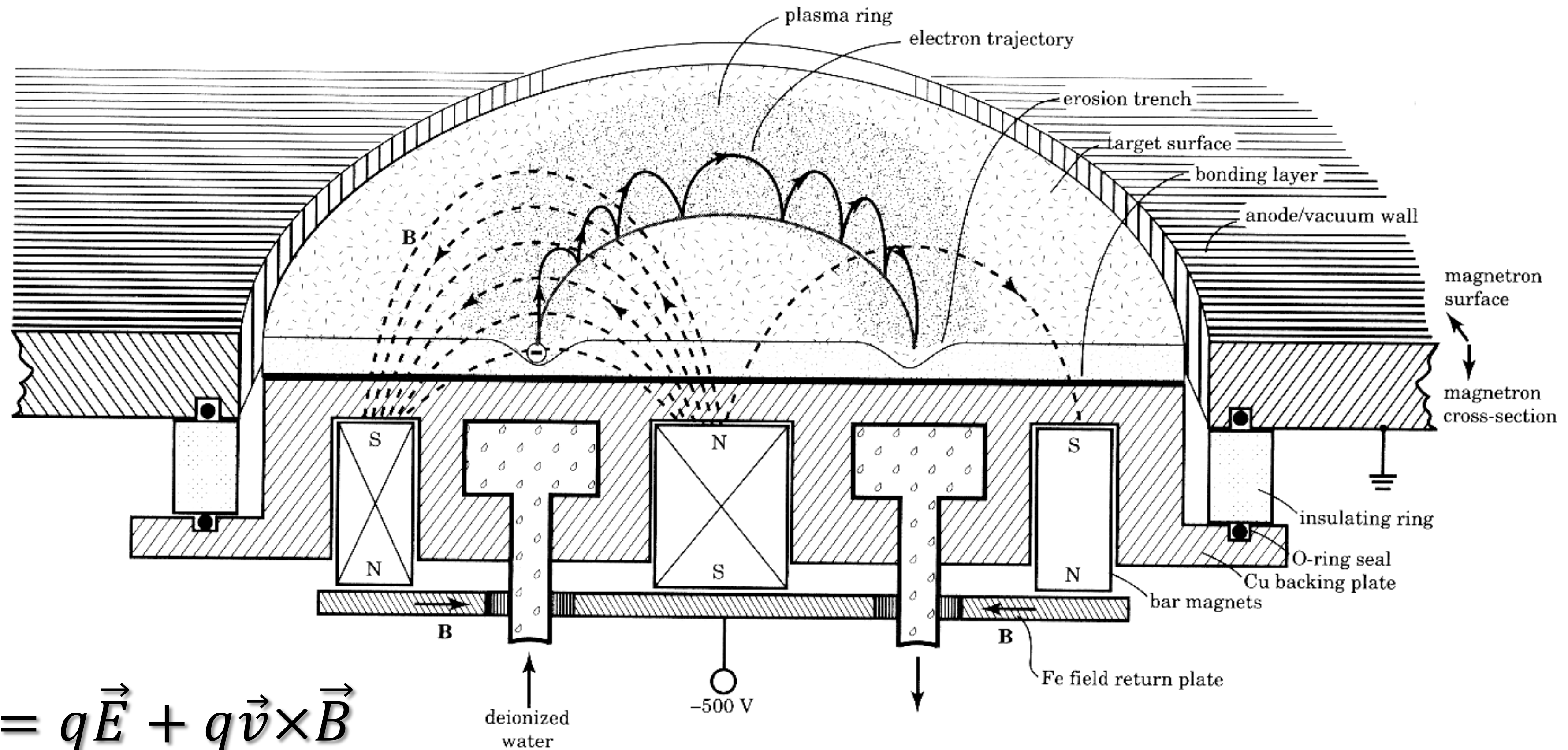

$$\vec{F} = q\vec{E} + q\vec{v}\times\vec{B}$$

Figure 9.10 Planar-magnetron structure and behavior. The electron-orbit radius is shown much larger than actual size for clarity.

Donald L. Smith, *Thin-Film Deposition*, McGraw-Hill, Boston (Ma), USA, 1995.

1. Vapour Phase

rf - Ionic sputtering – planar magnetron

$$\vec{F} = q\vec{E} + q\vec{v}\times\vec{B}$$

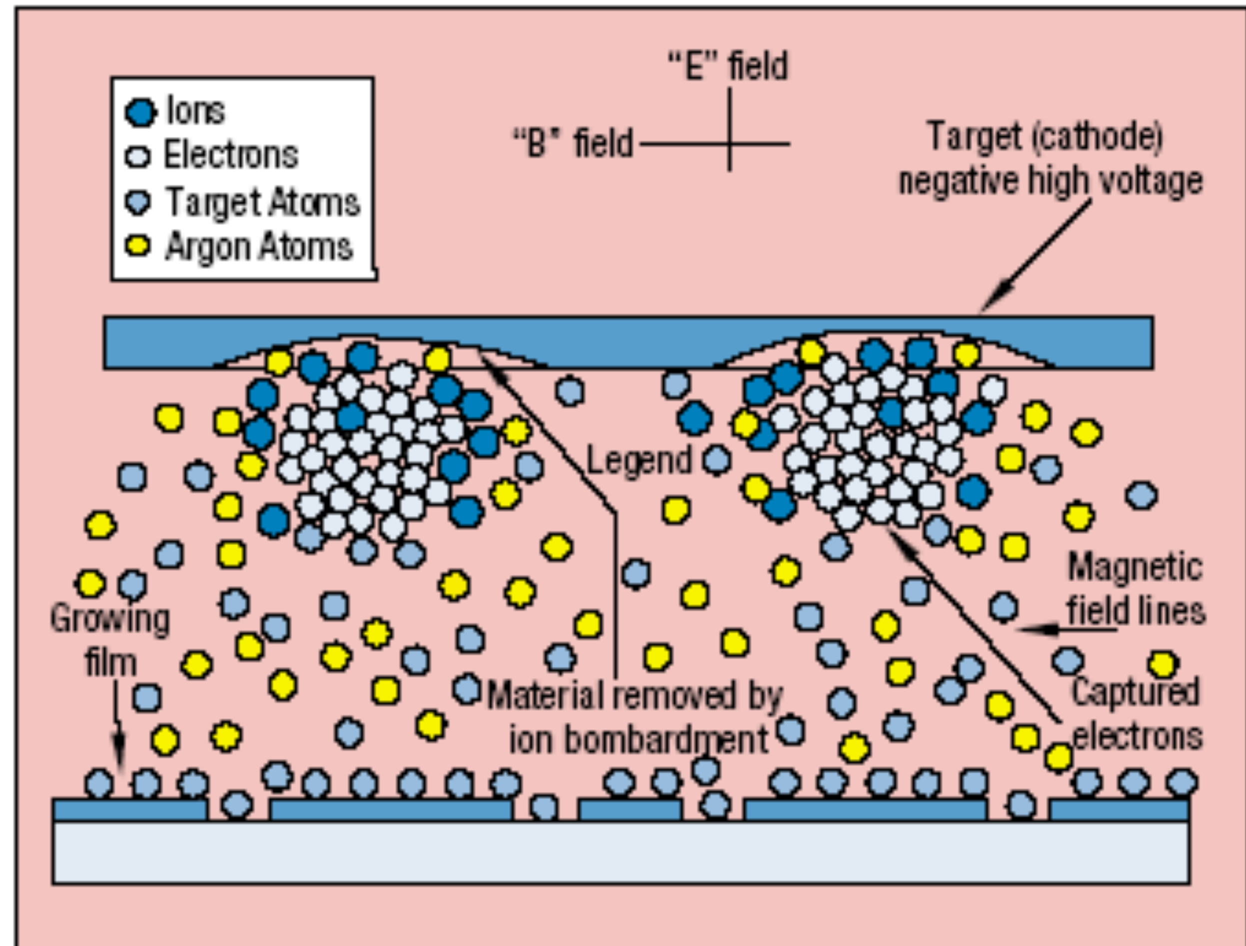

Mass transfer

Plasma Sources Sci. Technol. 29 (2020) 113001

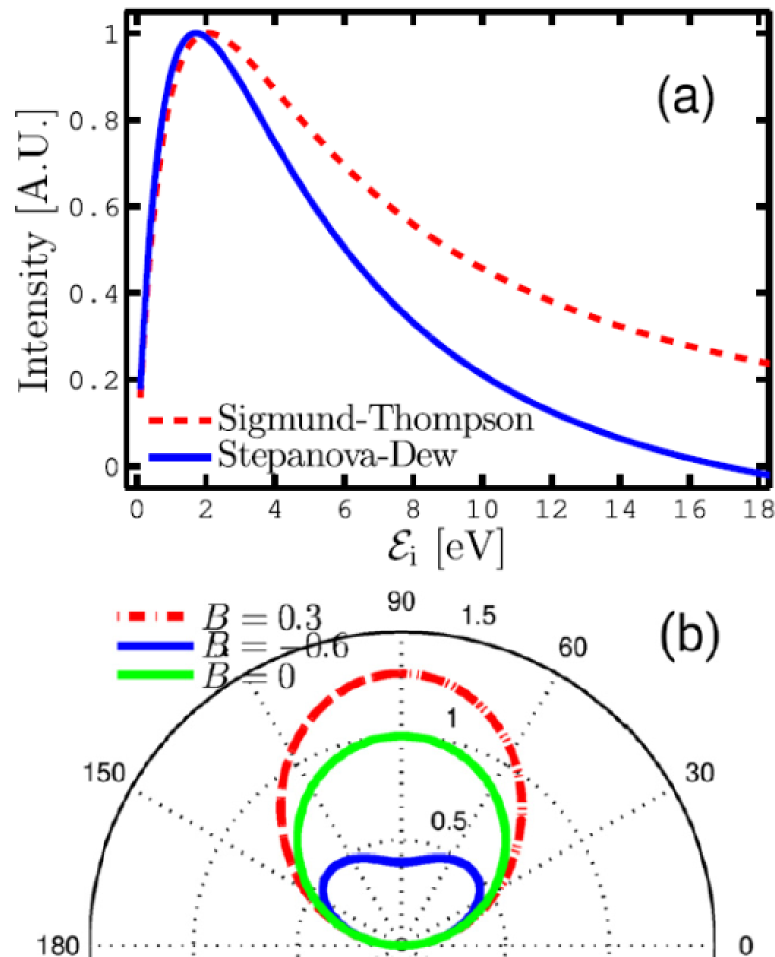

Figure 19. (a) The Sigmund–Thompson and the Stepanova–Dew energy distributions for titanium with binding energy of 3.30 eV and the cut-off energy set to 17 eV and the constants were chosen as $n = 1$ and $m = 0.2$. (b) The sputter angular distribution for ions under normal incidence calculated by equation (36).

- Energy distribution of the sputtered ions from a planar magnetron under normal incidence

- Angular distribution of the sputtered ions

$$Y(\varepsilon, \theta) \propto \cos\theta\,(1 + B\cos^2\theta)$$

ε - incident ion energy

B - Calibration factor

Film growth

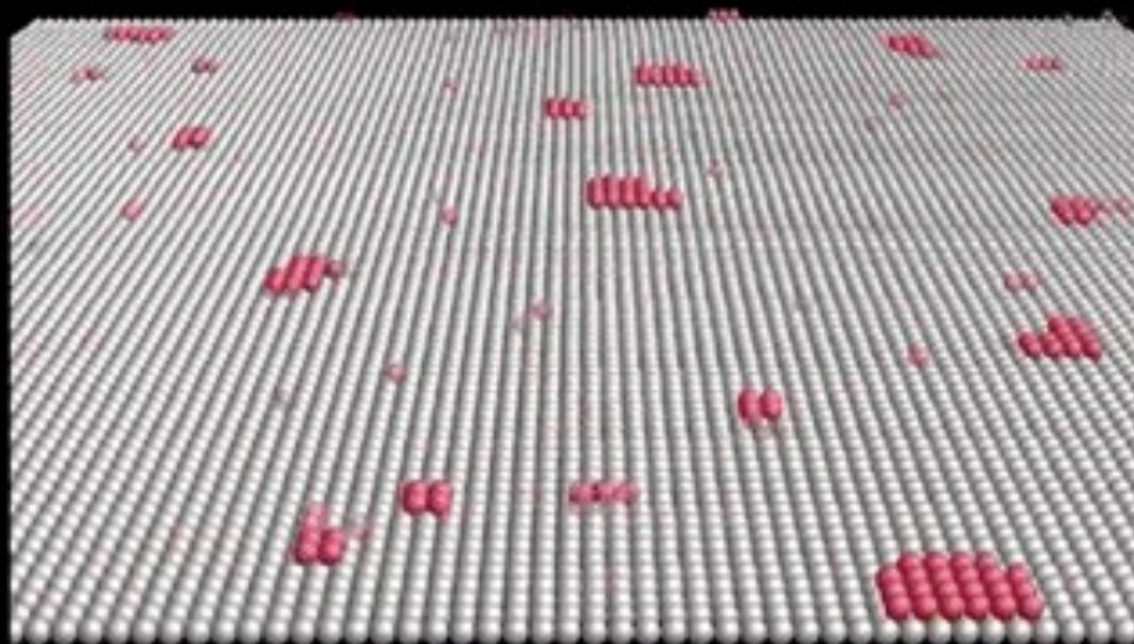

Thin Film Analysis

"ex-situ"

- Structural (XRD, RBS)
- Optical (PL, Raman, Elipsometry)
- Microscopy (SEM, TEM, AFM, PFM, MFM)
- Electrical
- Magnetic

Growth of (110) $YBa_2Cu_3O_{7-\delta}$ thin films

Phase diagram $YBa_2Cu_3O_{7-\delta}$
orthorrombic $\delta \approx 0.05 \rightarrow T_c = 92$ K

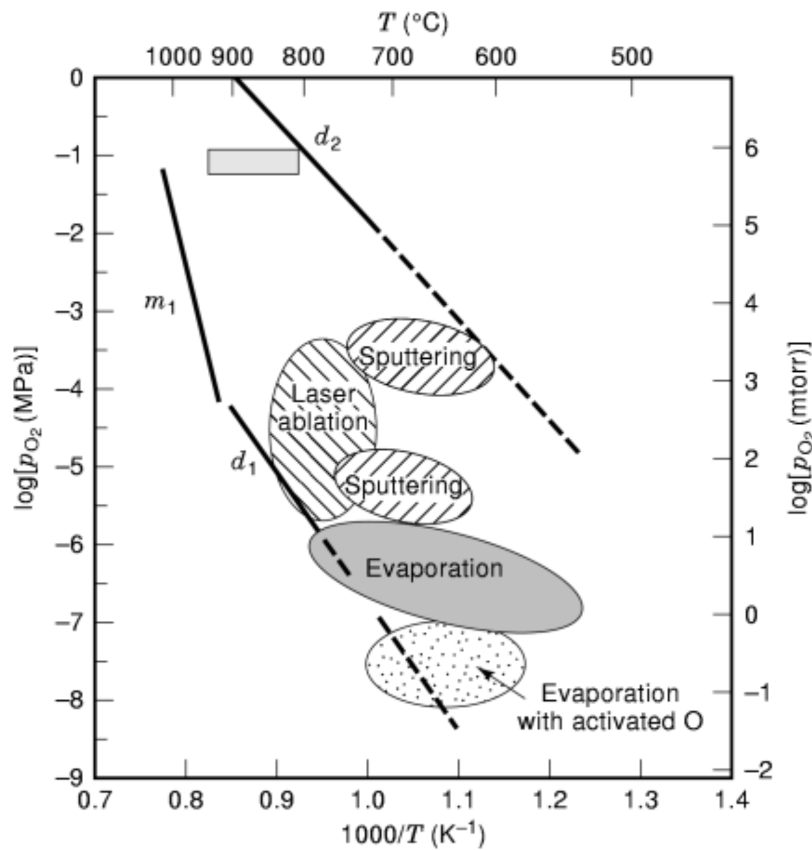

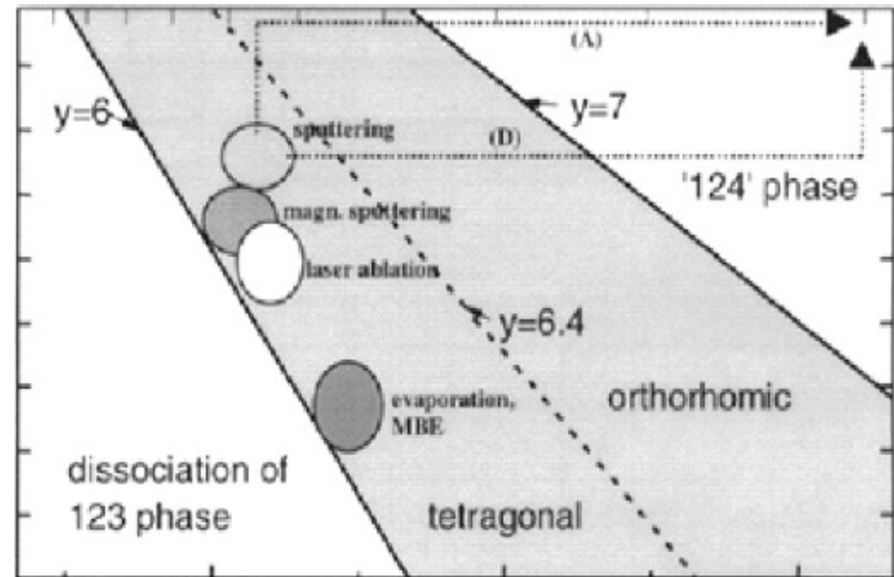

Growth of (110) $YBa_2Cu_3O_{7-\delta}$ thin films

What substrate

We have to look at several properties and characteristics including

- Lattice mismatch
- Surface cut and topography availables
- Thermal properties (for example, are there any phase transitions within the temperature range to be used during the deposition process?)
- Chemical compatibility
- Electrical and magnetic properties

Substrate used $SrTiO_3$

Growth of (110) $YBa_2Cu_3O_{7-\delta}$ thin films

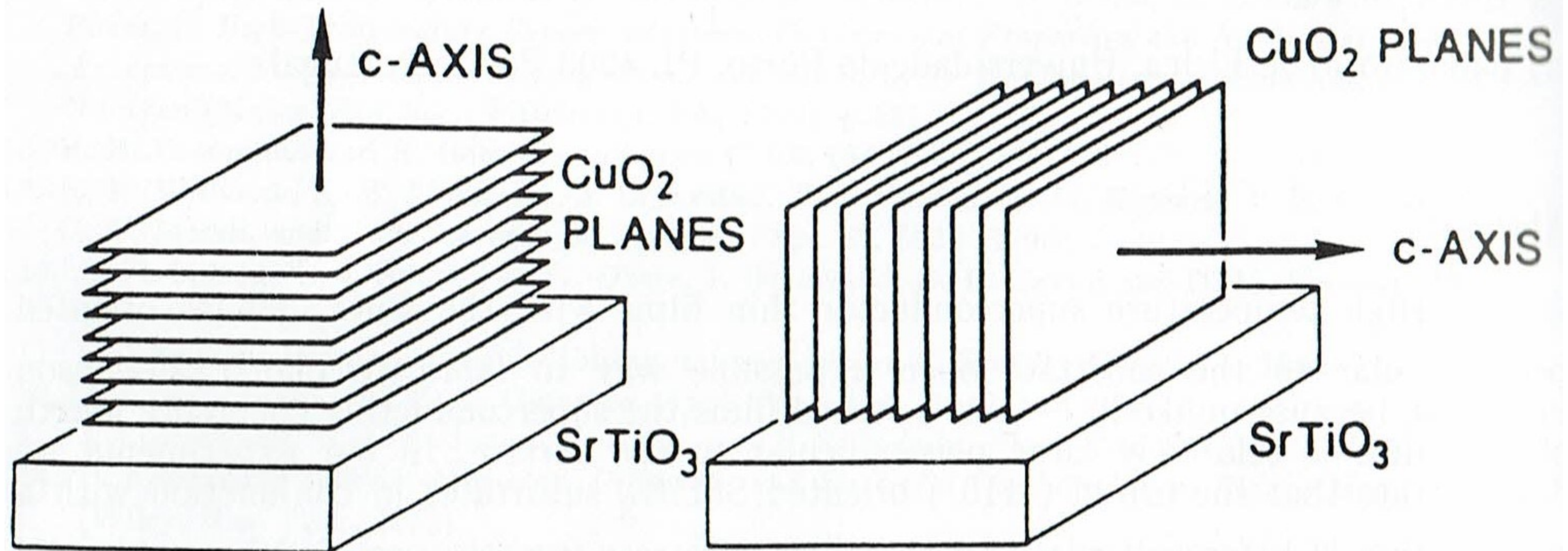

Fig1: Schematic representation of the orientation of the CuO_2 YBCO planes with respect to the film plane a.) for the c–axis perpendicular and b.) for the c– axis in the film plane.

Growth of (110) $YBa_2Cu_3O_{7-\delta}$ thin films

direction and perpendicular to that a [110] direction. Since along the [001] direction the lattice mismatch between film and substrate

$$(3a_{SrTiO_3} - c_{YBCO}) / c_{YBCO} = 1.3 \cdot 10^{-3}$$

is rather small a preferential growth with the c – axis macroscopically aligned is generated. Fig. 2 shows the orientations of the crystal axes in the substrates of different cuts schematically.

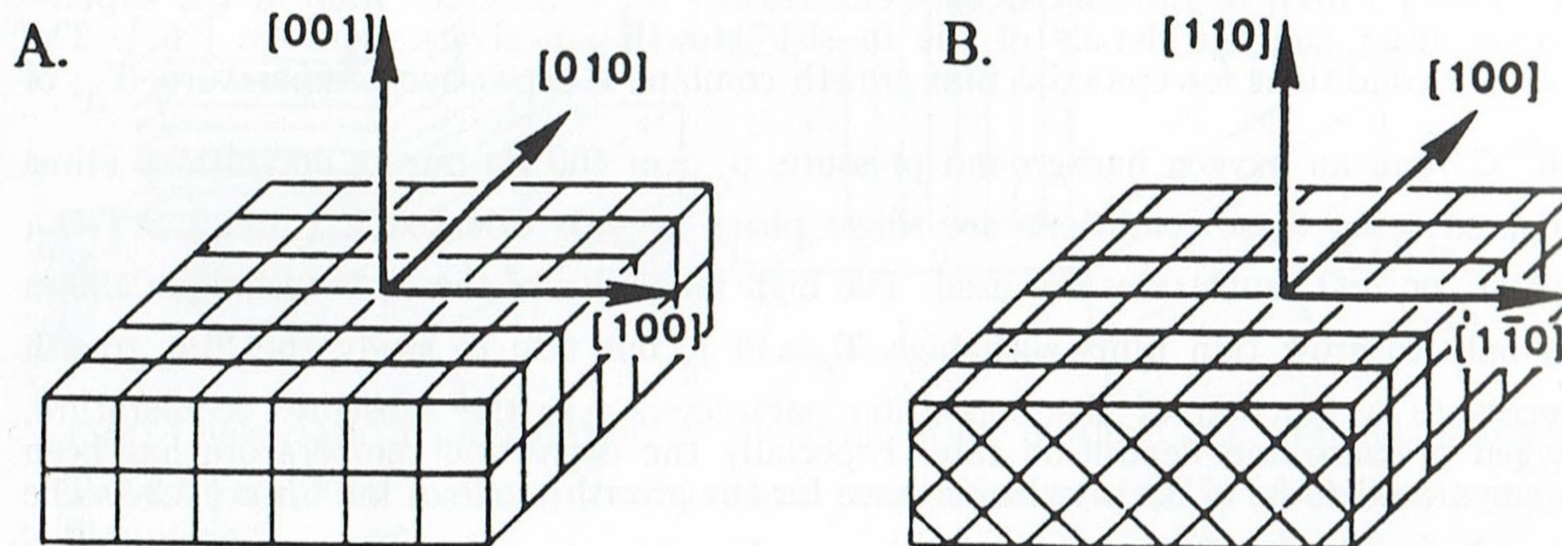

Fig. 2: Crystal orientations in a (100) cut [a] and in a (110) cut [b].

Growth of (110) $YBa_2Cu_3O_{7-\delta}$ thin films

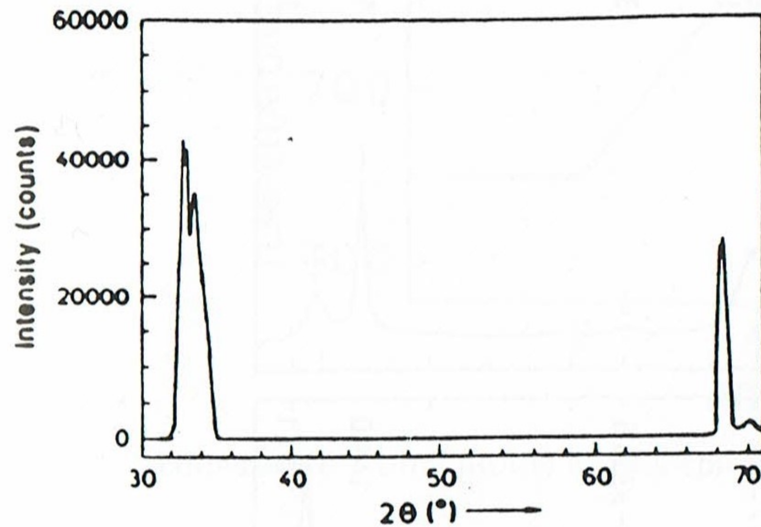

Fig. 3: X ray diffraction pattern of a YBCO film on (110) strontiumtitanate $T_d = 780^oC$.

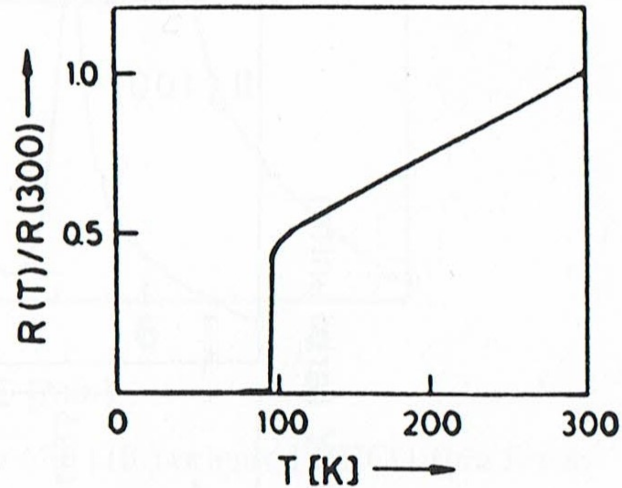

Fig. 4 Transition curve of the film in Fig.3.

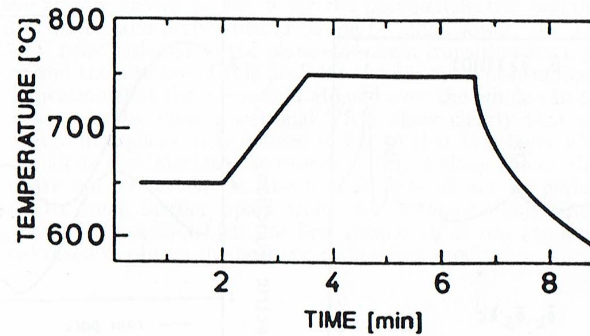

Fig. 6: Temperature / time profile for the epitaxy of (110) oriented YBCO thin films.

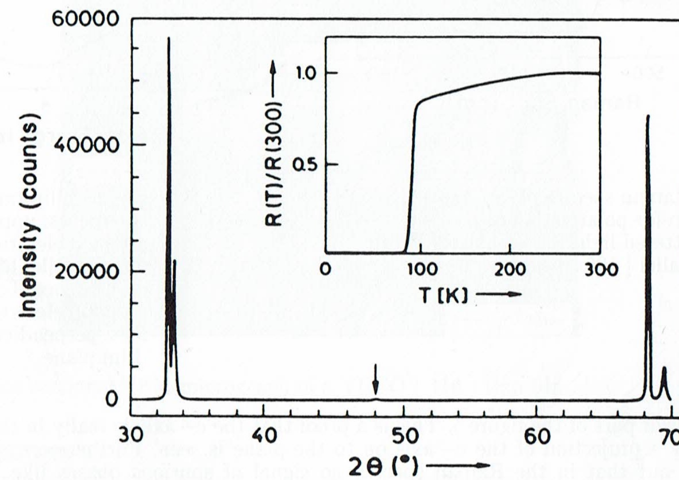

Fig. 7: X – ray diffraction pattern of an (110) oriented YBCO thin film [the insert shows the electrical transition to superconductivity].

"The growth of (110) YBaCuO thin films and their characterization by optical methods", Habermeier, H.-U.; Lourenço, A.A.C.S.; Friedl, B.; Kircher, J.; Köhler, J., *Solid State Communications* 77 9 (1991): 683-687.

Growth of (110) $YBa_2Cu_3O_{7-\delta}$ thin films

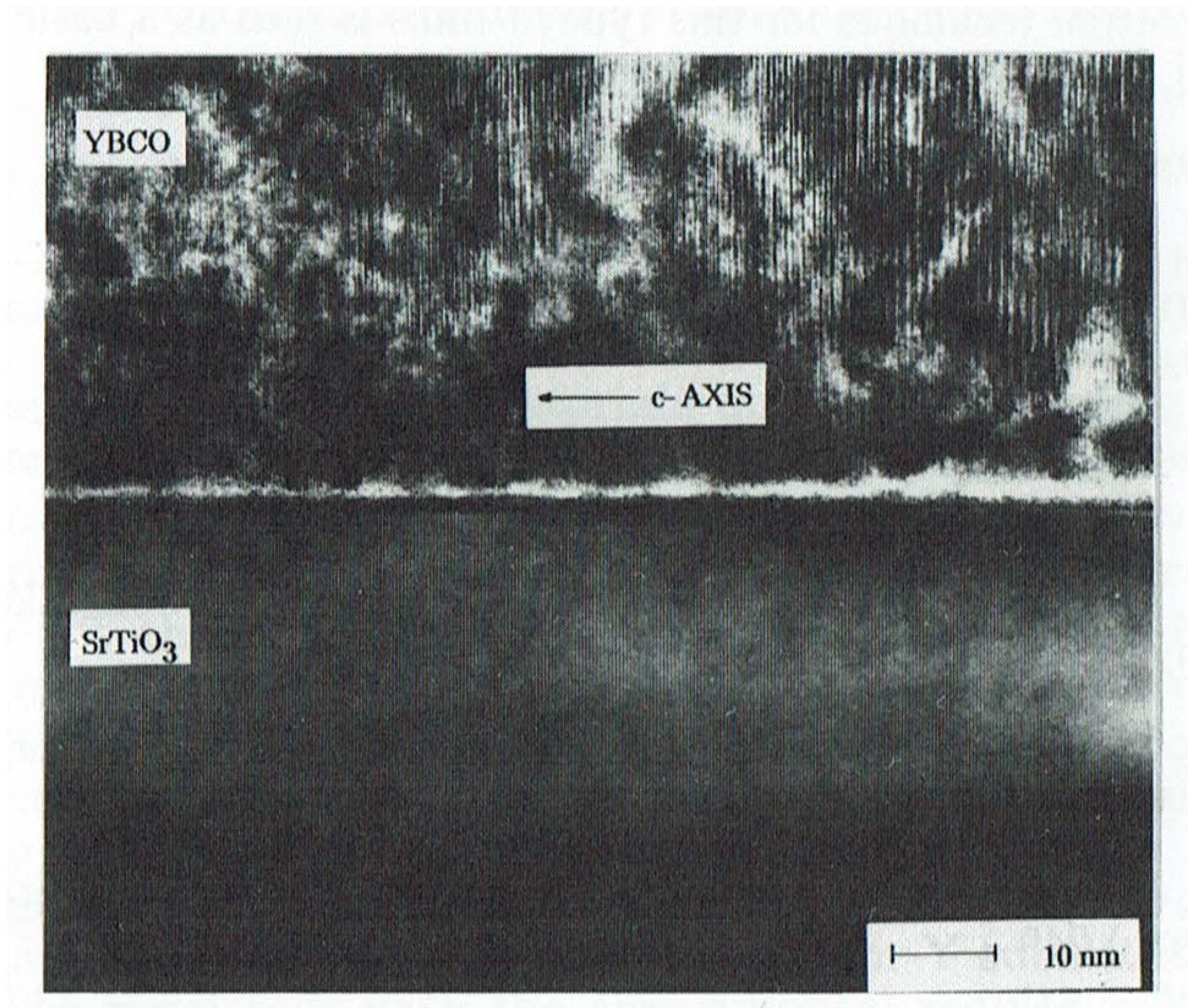

Growth of (110) $YBa_2Cu_3O_{7-\delta}$ thin films

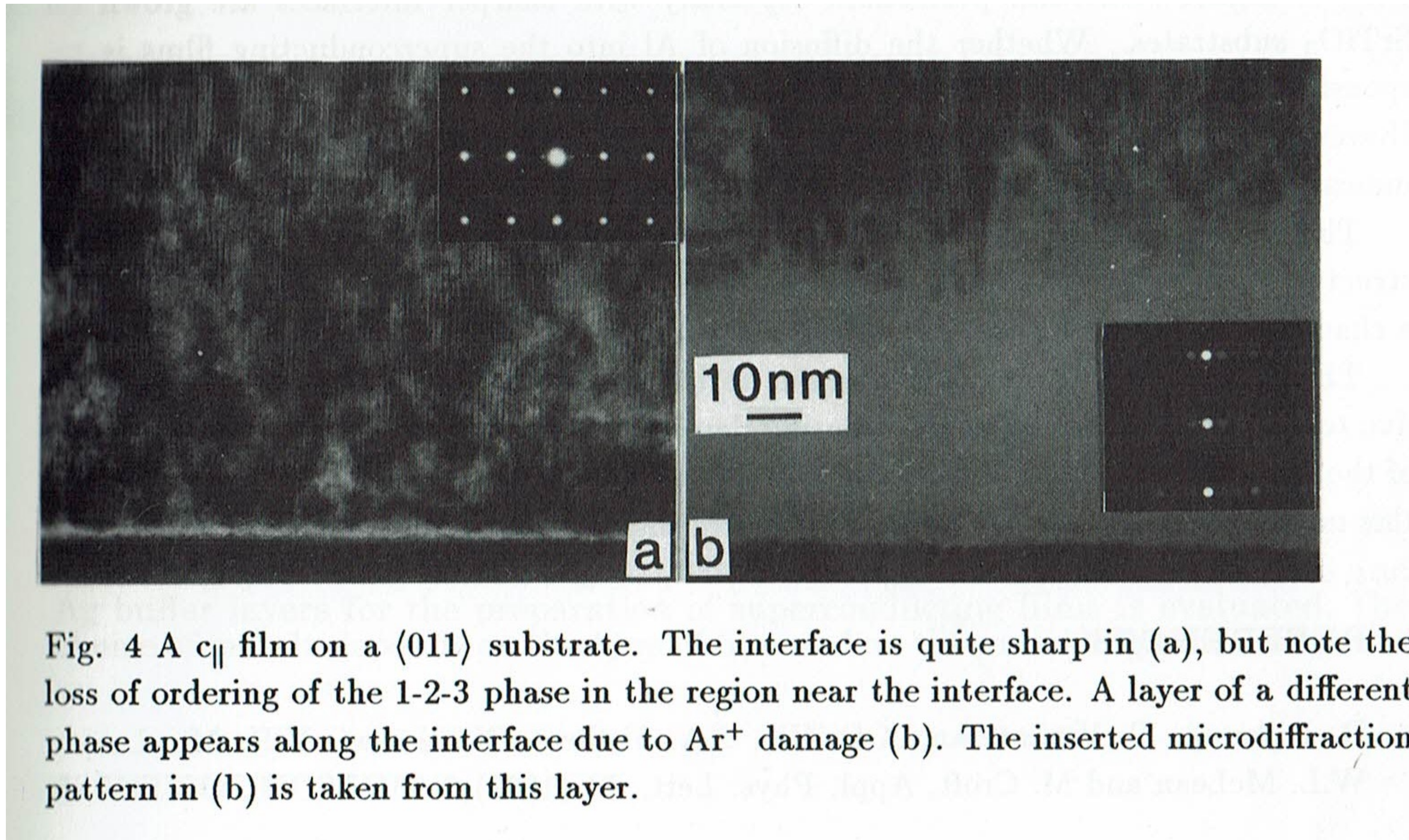

Fig. 4 A $c_{\parallel}$ film on a ⟨011⟩ substrate. The interface is quite sharp in (a), but note the loss of ordering of the 1-2-3 phase in the region near the interface. A layer of a different phase appears along the interface due to Ar^+ damage (b). The inserted microdiffraction pattern in (b) is taken from this layer.

Surface crystallisation of thin (5.6 nm) amorphous $BaTiO_3$ films

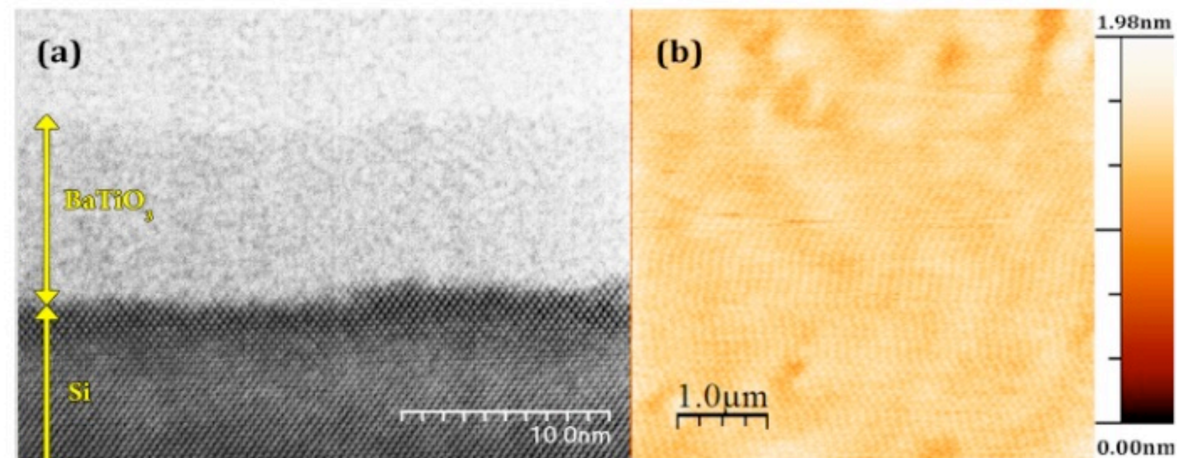

Figure 1. (**a**) Bright field STEM image of a 5.6 nm-thick $BaTiO_3$ film on Si substrate and (**b**) topography of the film before poling (RMS roughness 0.18 nm).

Surface crystallisation of thin (5.6 nm) amorphous $BaTiO_3$ films

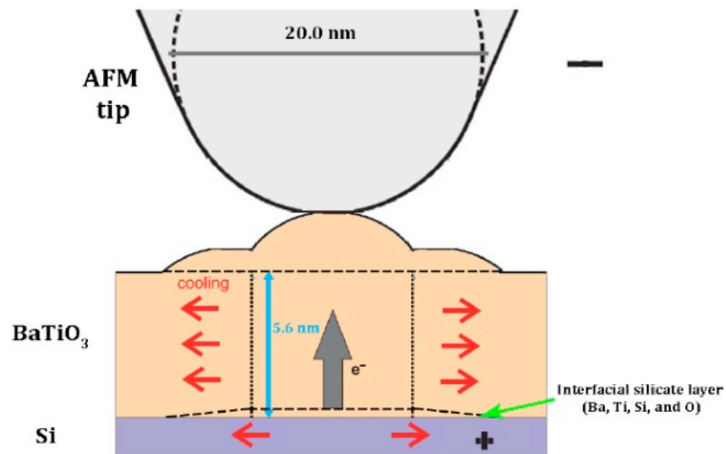

- Amorphous BatiO3 thin film with 5.6 nm thickness
- Surface was locally elevated 9 nm (-20V) and doesn't retract even when under +20V electric field
- 160% strain in the poled region
- Voltage threshold for modifying surface is -12V
- Modified topography showed a 0.02 nm/min decay
- The poled material develops high polarization that cannot be switched back, even under a high electric field
- Strong vertical piezoresponse was observed, witch increased with time after poling, 20% after 100 min
- The top layer of amorphous BaTiO3 film becomes ferroelectric because of local crystallization (by Joule heating?)

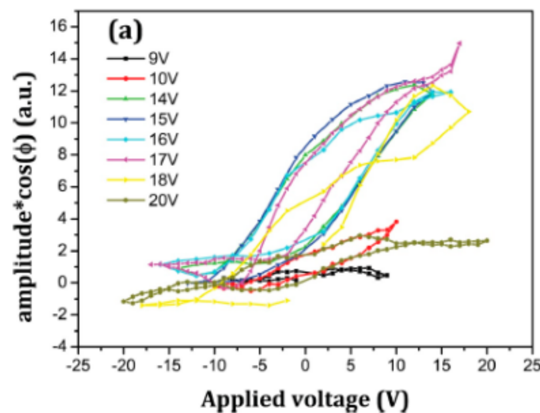

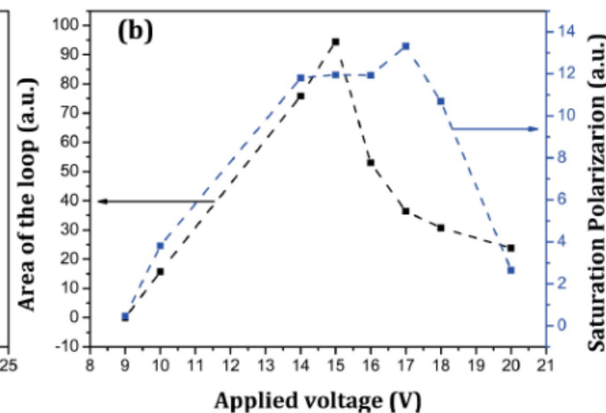

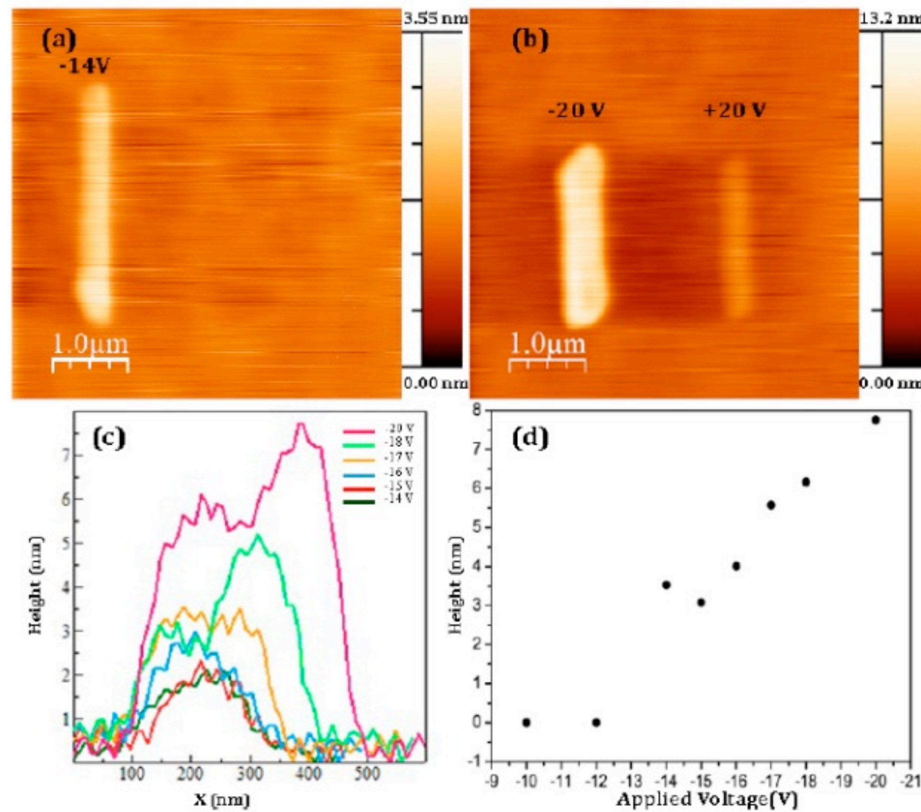

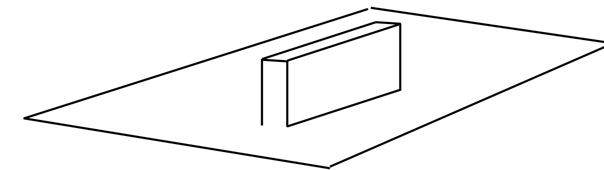

hight: ≈ 9 nm
width: ≈ 200 – 400 nm

Figure 2. Topography of $BaTiO_3$ thin film after application of ±14 V (**a**) and ±20 V; (**b**) during scanning of the area 0.2 × 2 μm^2; (**c**) Comparison of the topography cross-sections of the areas poled with different voltages; (**d**) Average height of the poled areas vs. applied negative voltage.

"Giant Strain and Induced Ferroelectricity in Amorphous BaTiO3 Films under Poling", Pegah Mirzadeh Vaghefi, Ali Baghizadeh, Armando A.C.S. Lourenço, Vitor S. Amaral and Andre L. Kholkin, Materials 2017, 10, 1107; doi:10.3390/ma10091107

LaBaMnO/BaTiO3/LaBaMnO heterostructures

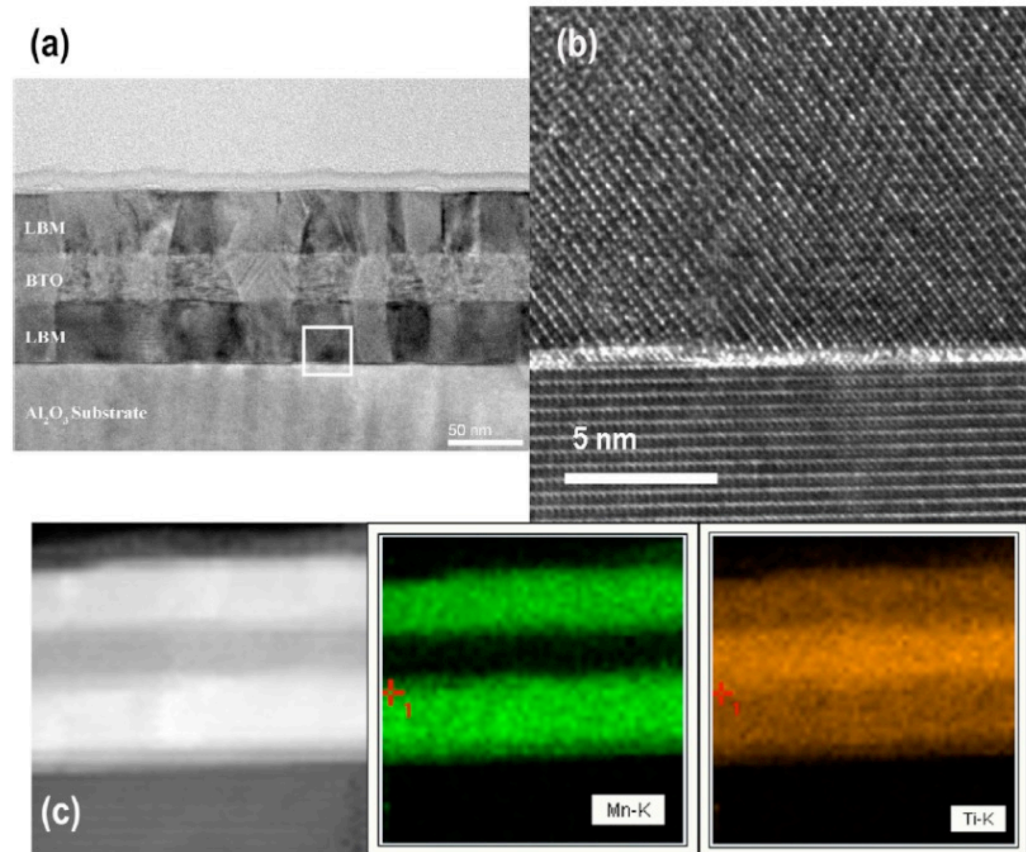

Fig. 6. (a) TEM micrograph of $LBMBT_a$ heterostructure, the thickness of the layers is 40/30/40 nm, respectively, (b) the interface between bottom LBM layer and substrate, the epitaxial growth of the film is obvious, and (c) the STEM-HAADF micrograph and EELS-mapping of the $LBMBT_a$ heterostructure.

"Effect of lattice mismatch on the magnetic properties of nanometer-thick La0.9Ba0.1MnO3 (LBM) films and LBM/BaTiO3/LBMheterostructures", P. Mirzadeh Vaghefia, A. Baghizadehb, M. Willingerc, A.A.C.S. Lourenco, V.S. Amaral, *Applied Surface Science* **425** (2017) 988–995, http://dx.doi.org/10.1016/j.apsusc.2017.06.252 0169-4332

XRR – X-Ray Reflectometry

Heinz Kiessig fringes 1931 (Ni on glass)

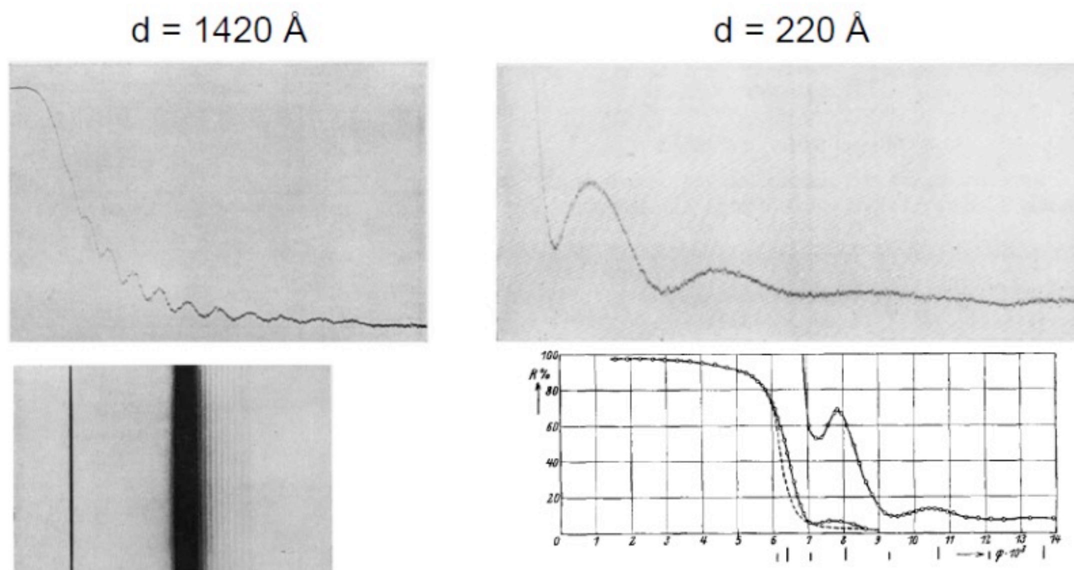

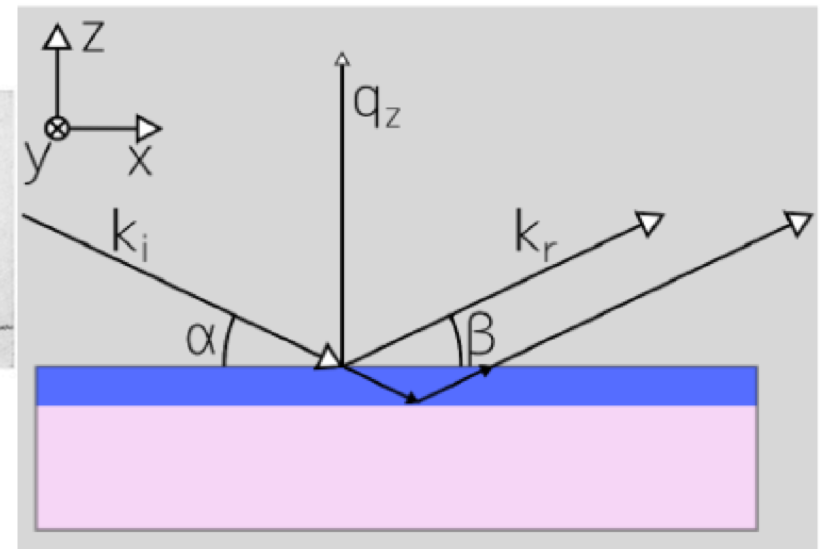

Kiessig, Heinz (1931). "Untersuchungen zur Totalreflexion von Röntgenstrahlen". Annalen der Physik, 402 (6): 715–768

HfO_2 thin films

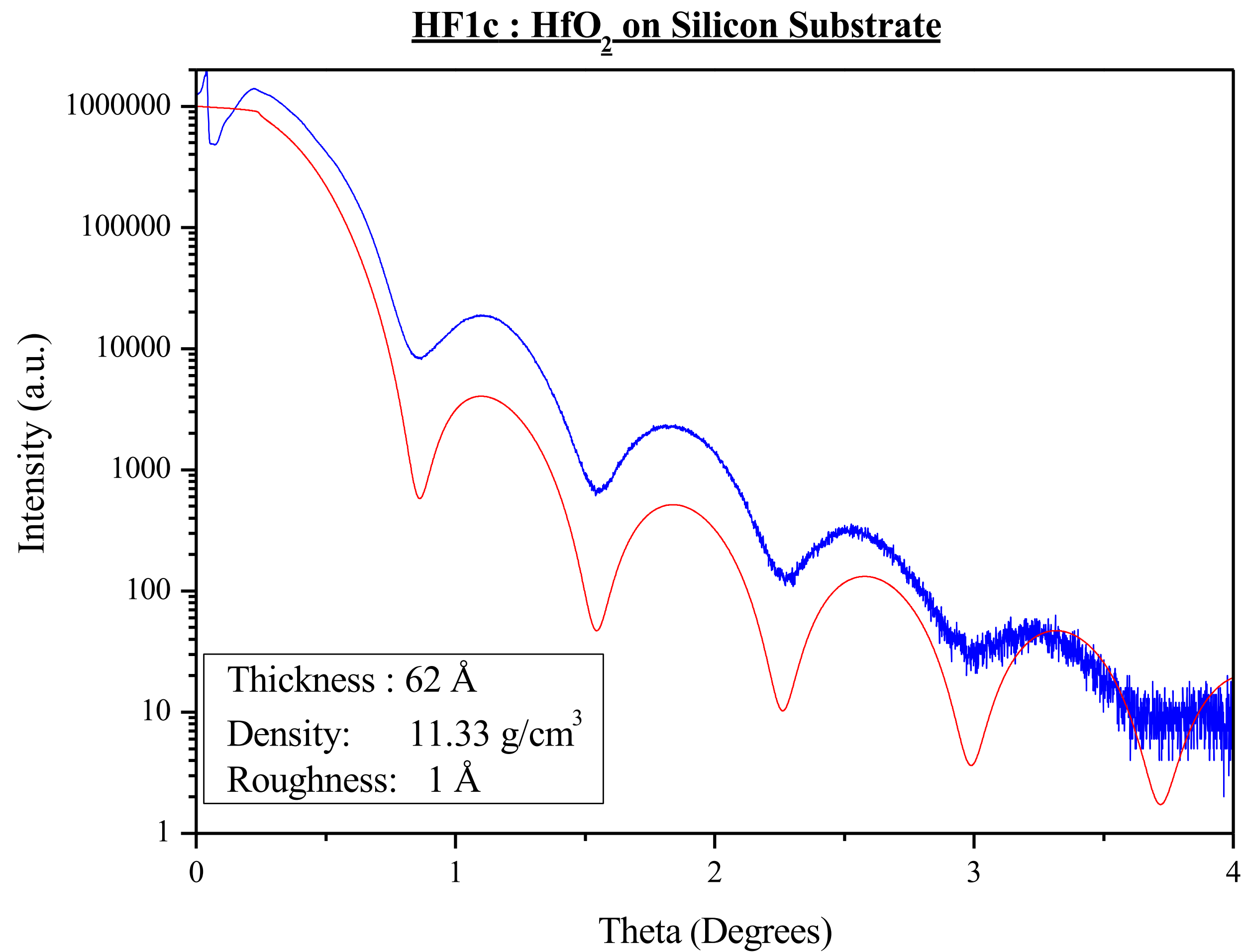

HfO_2 thin films

HfO_2 on Si (100) (sample Hf1c)

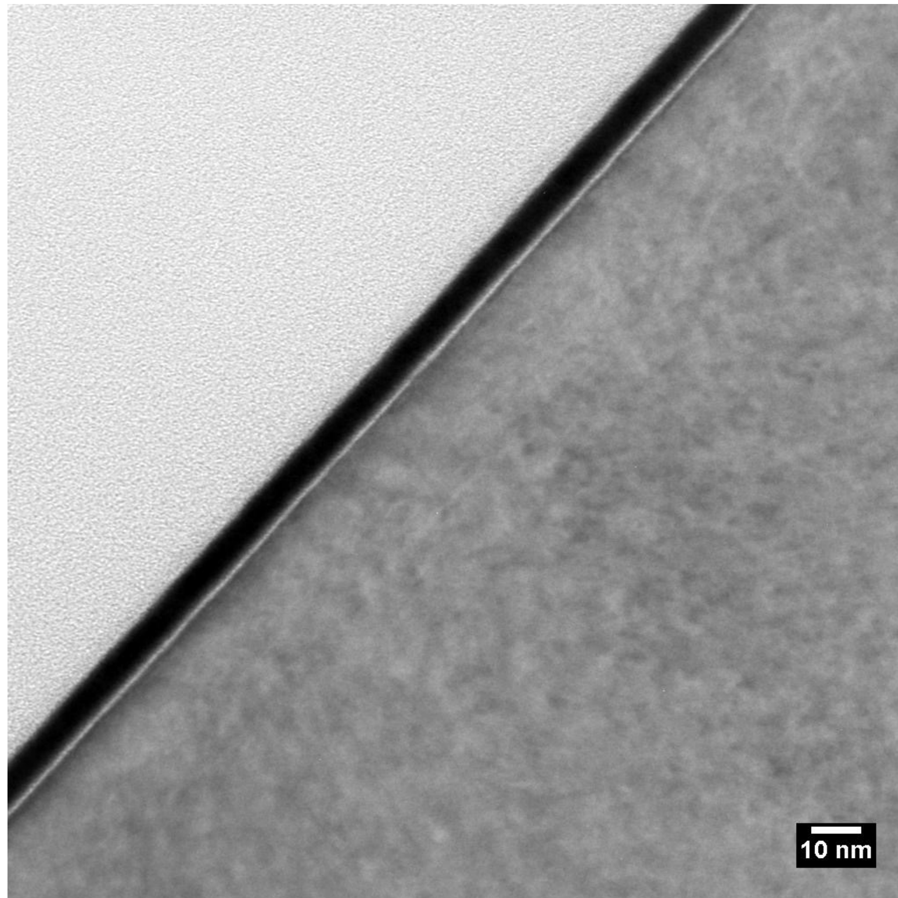

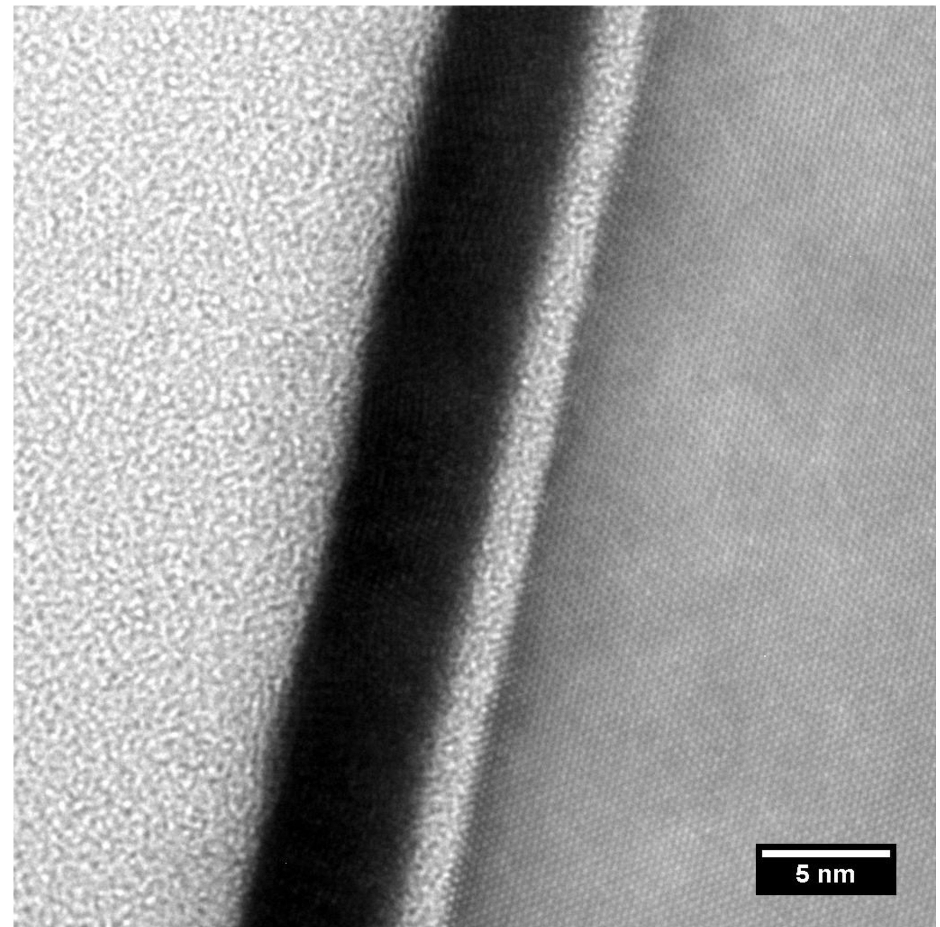

HfO_2 thin films

The Si (100) substrate was etched (HF-last) for removal of the SiO_2 native layer, but a SiO2 layer was formed during HfO_2 deposition.

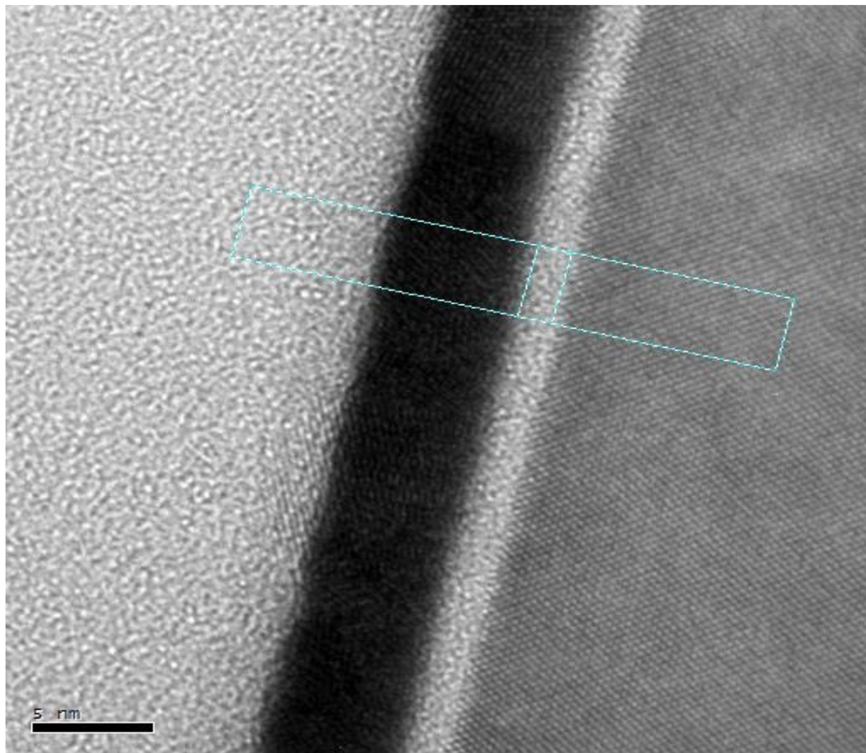

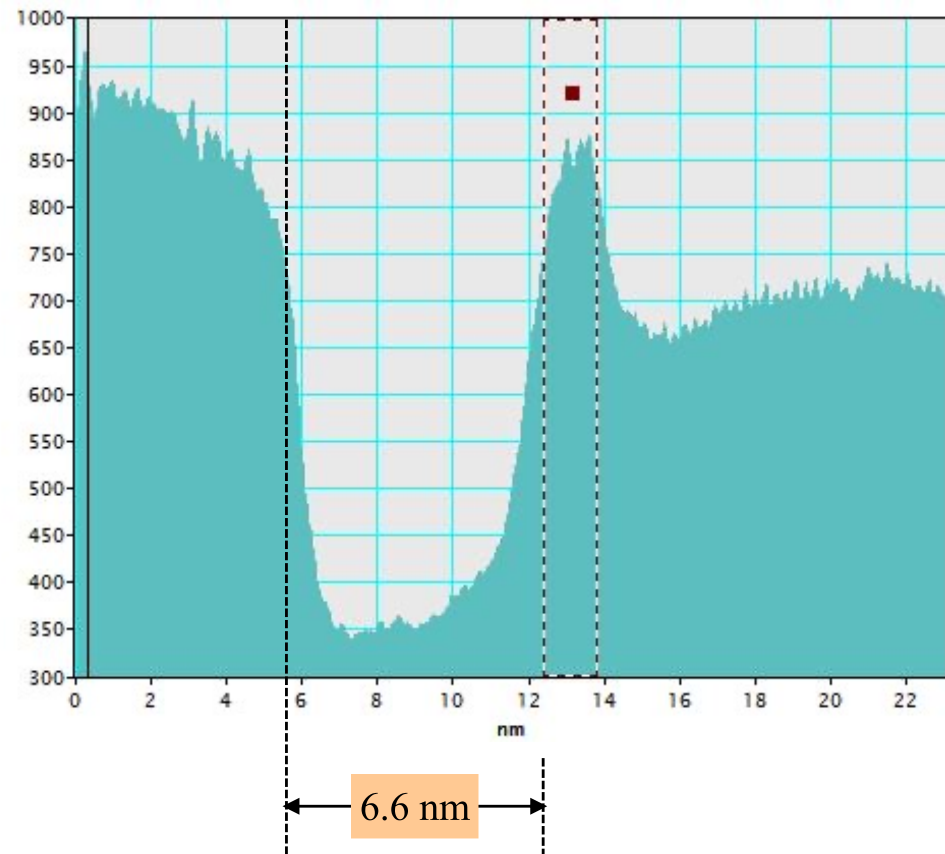

The SiO2 interlayer is 1.43 nm thick

Thickness of the film: 6.6 nm

HfO_2 thin films

To prevent the SiO_2 layer formation during HfO_2 deposition, we deposited a ultra-thin layer (patent pending) on the Si (100) clean surface.

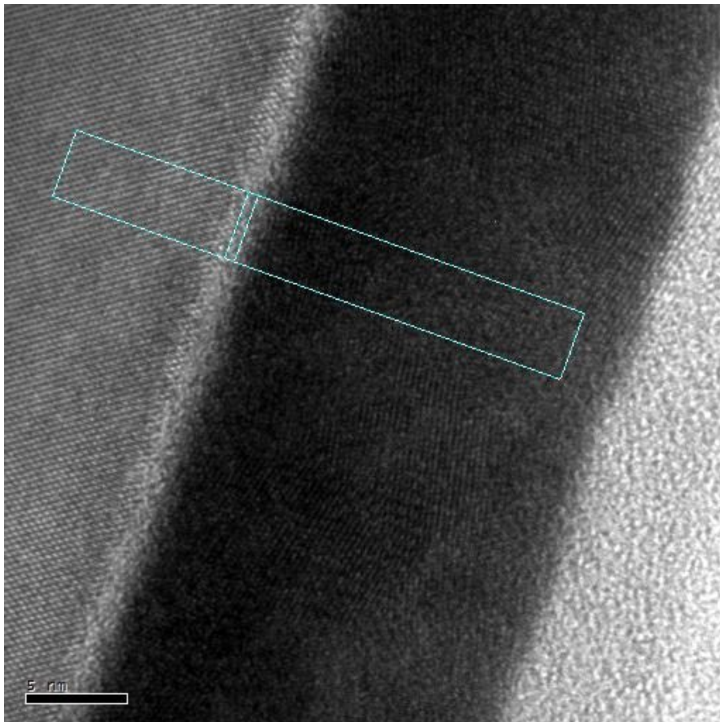

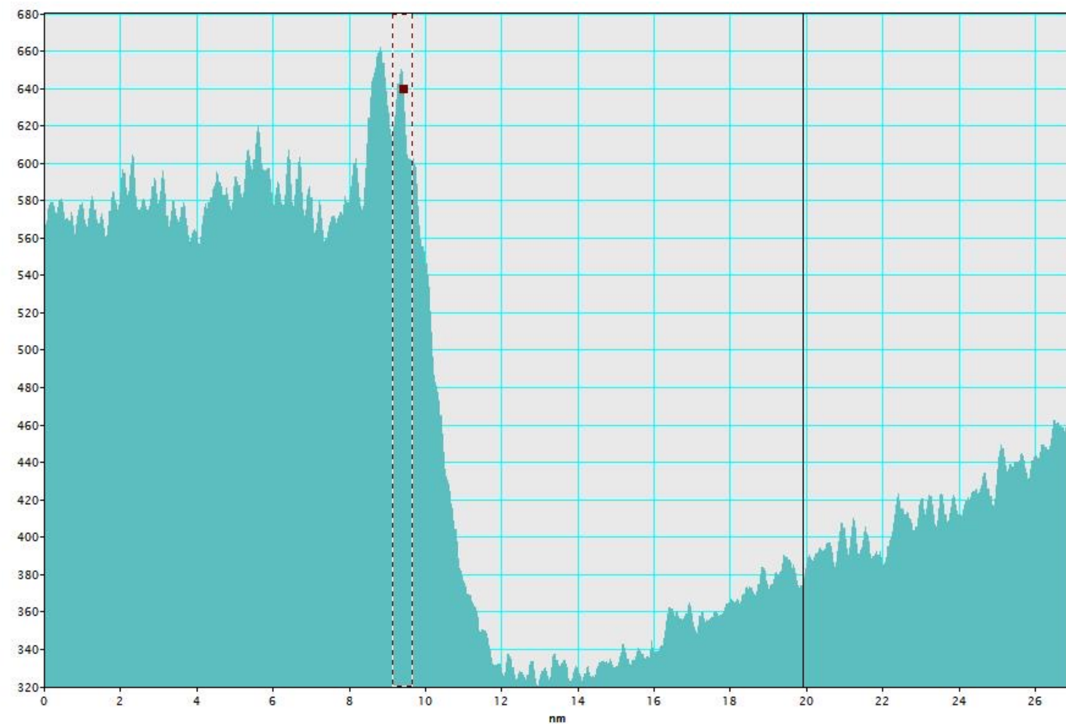

The interlayer is about: 0.5 – 0.6 nm
Thickness of the film: 20 – 20.5nm
Thickness and nature are really different

HfO_2 thin films

HfO_2/Mg/Si(100)

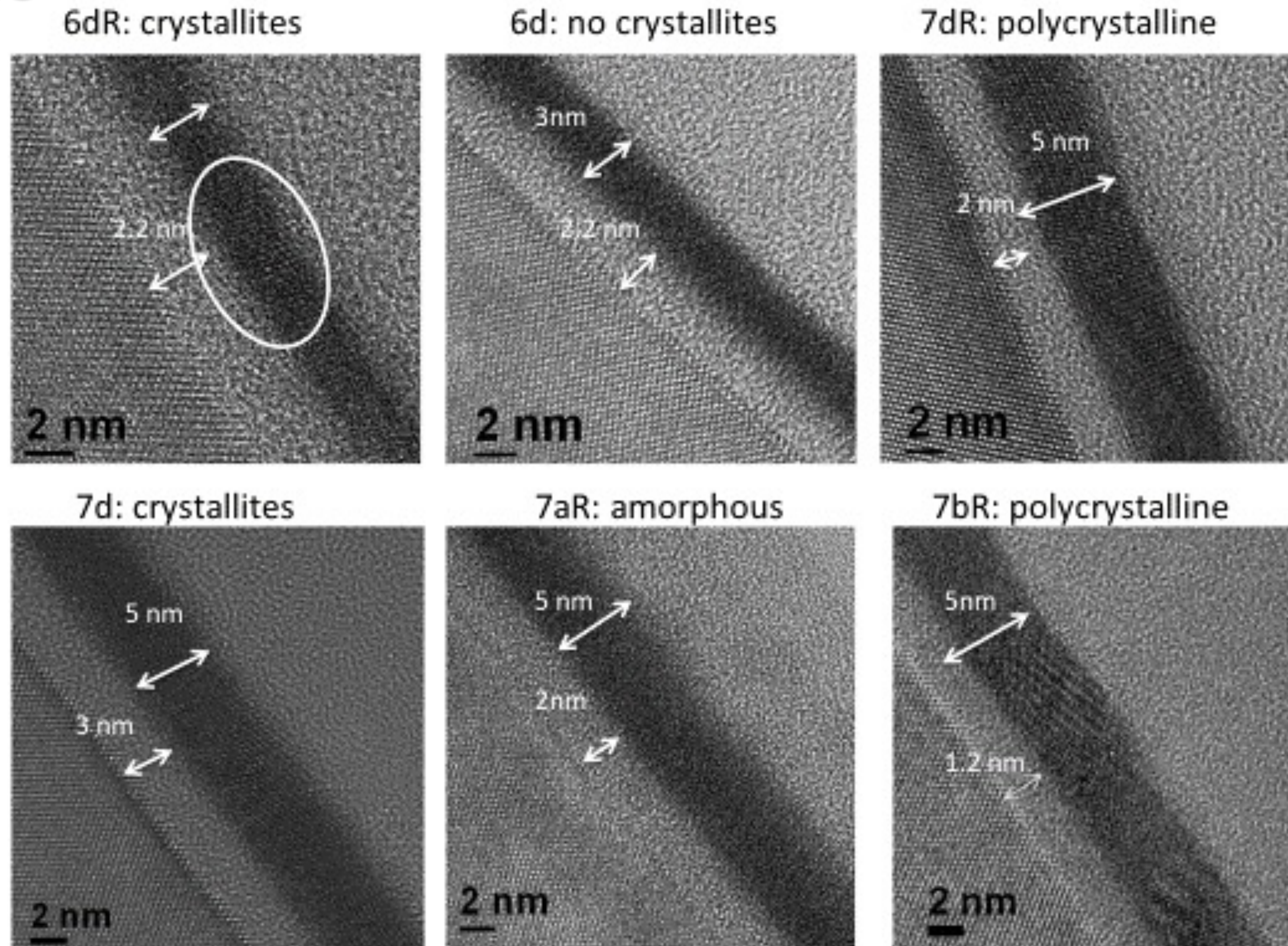

"Metallic Mg oxygen diffusion barrier difusion applied for electronic devices", Armando Santos Lourenço and Erwan Yann Rauwel, WO/2011/070398, PCT/IB2009/055667.

HfO_2 thin films

HfO_2 thin films on Si(100) deposited using ALD and rf-Magnetron Sputtering

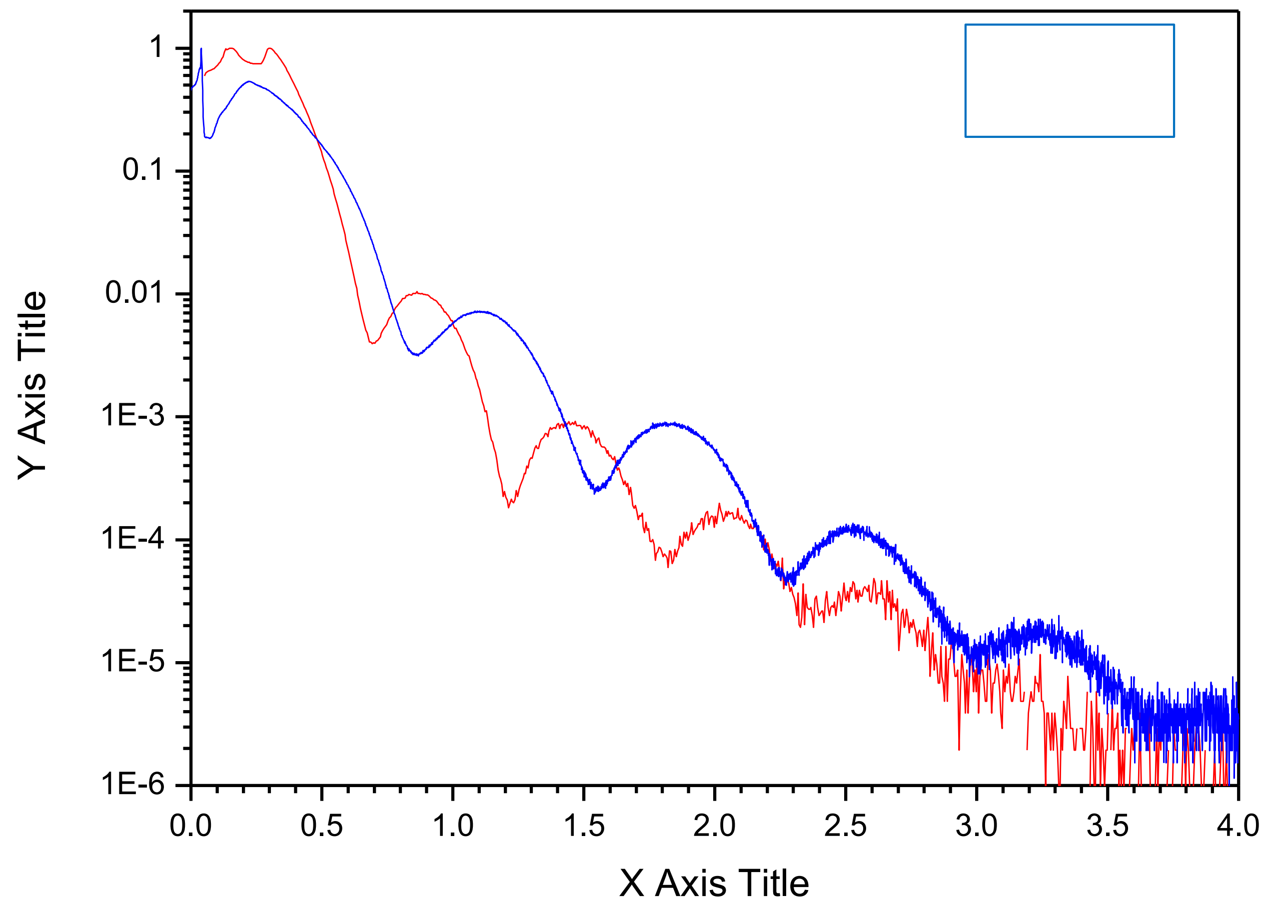

RBS – Rutherford Backscattering Spectrometry

What is Rutherford Backscattering Spectrometry?

It exploits the phenomenon of collision between a mono-energetic ion beam with the atoms of the target

For the energies (some MeV) and the ions (light ions such H+, He++) employed, the process can be fairly considered an elastic unscreend interaction between the nucleuses as in the Rutherford experiment

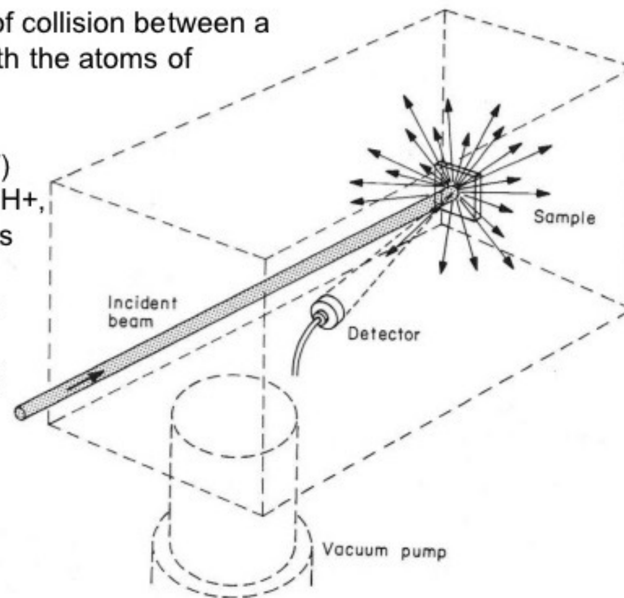

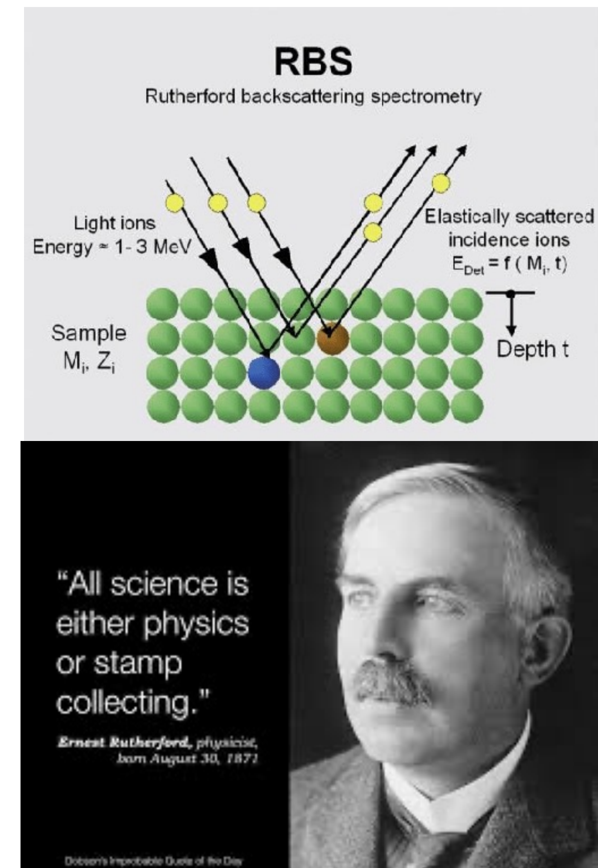

RBS – Rutherford Backscattering Spectrometry

ZnO thin films

What is Rutherford Backscattering Spectrometry?

It exploits the phenomenon of collision between a mono-energetic ion beam with the atoms of the target

For the energies (some MeV) and the ions (light ions such H+, He++) employed, the process can be fairly considered an elastic unscreend interaction between the nucleuses as in the Rutherford experiment

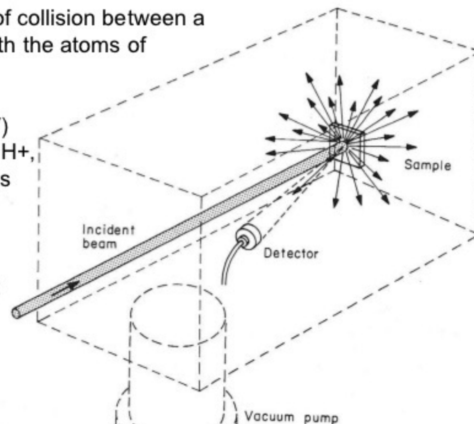

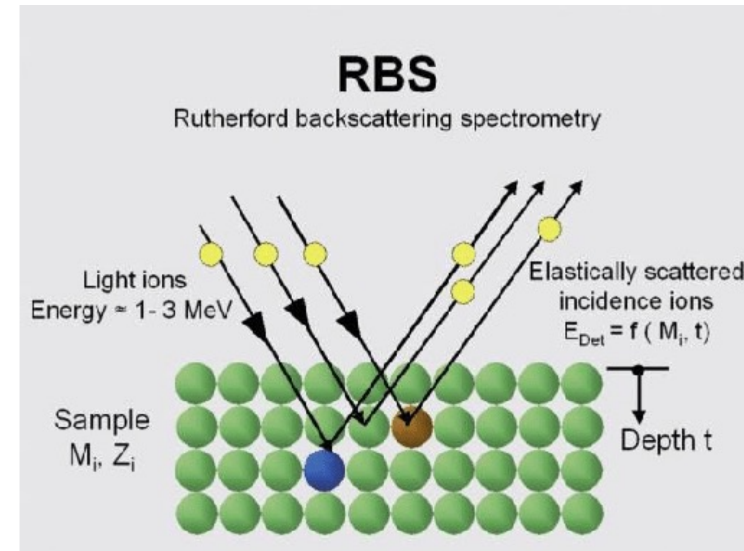

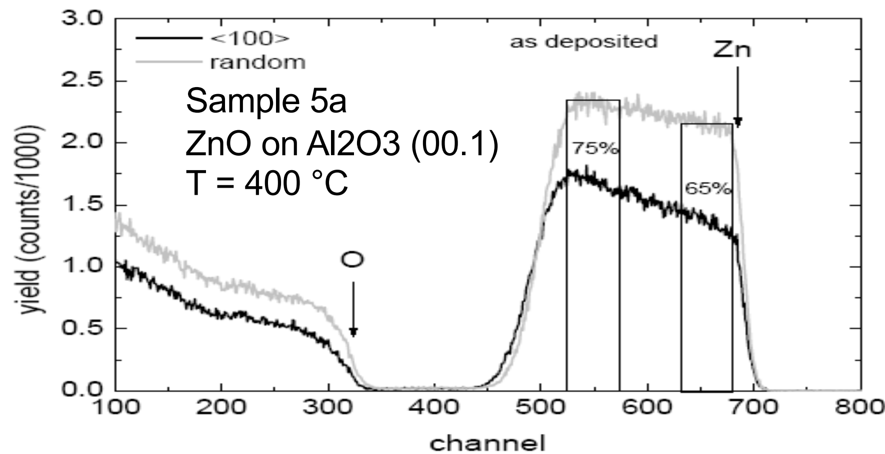

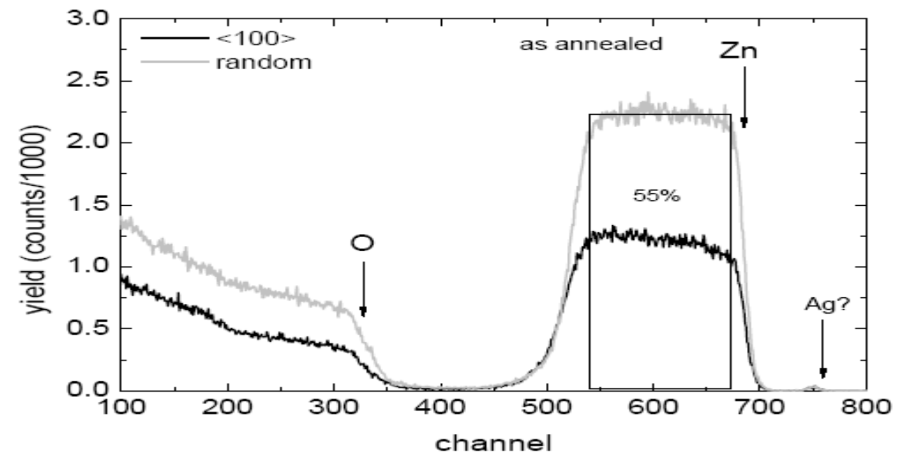

RBS – Rutherford Backscattering Spectrometry

ZnO thin films

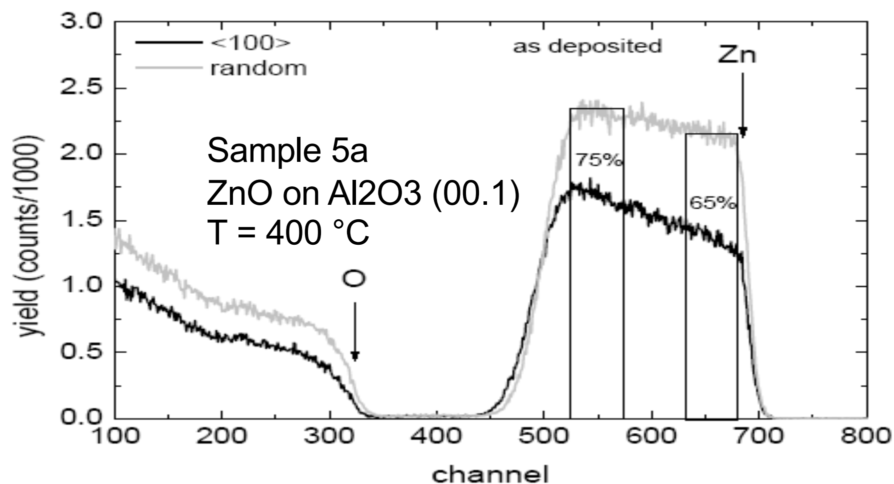

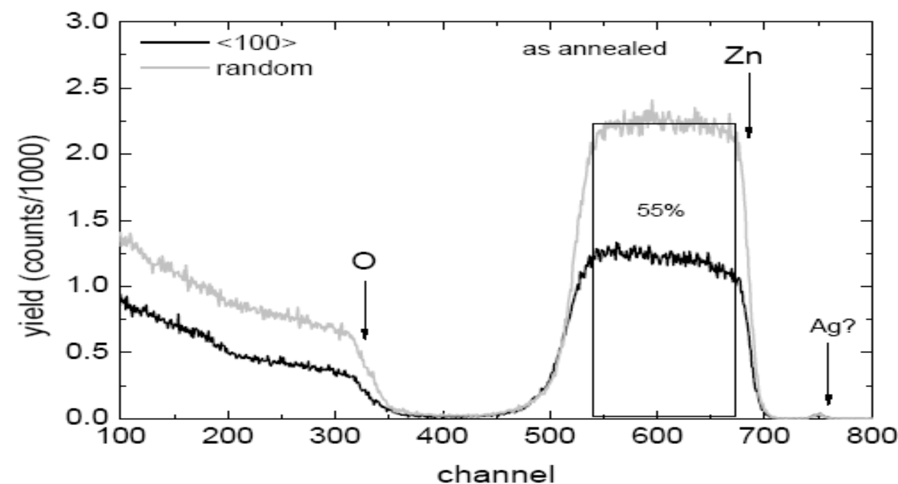

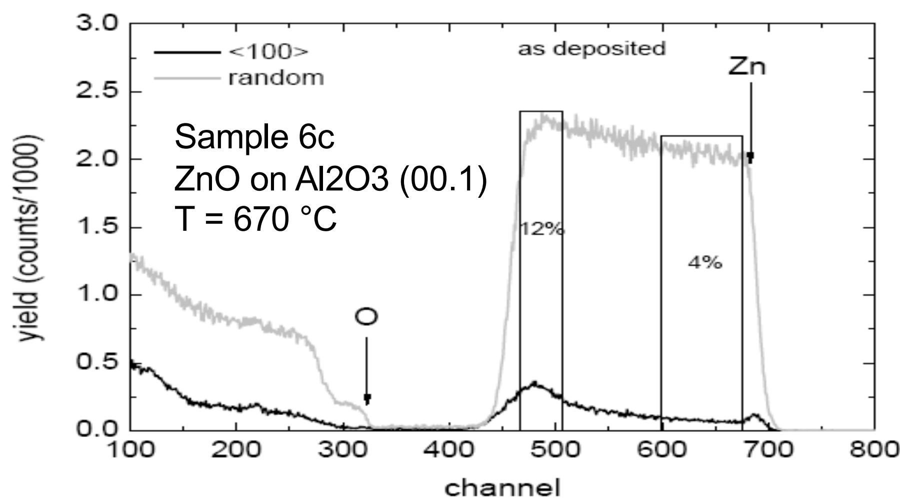

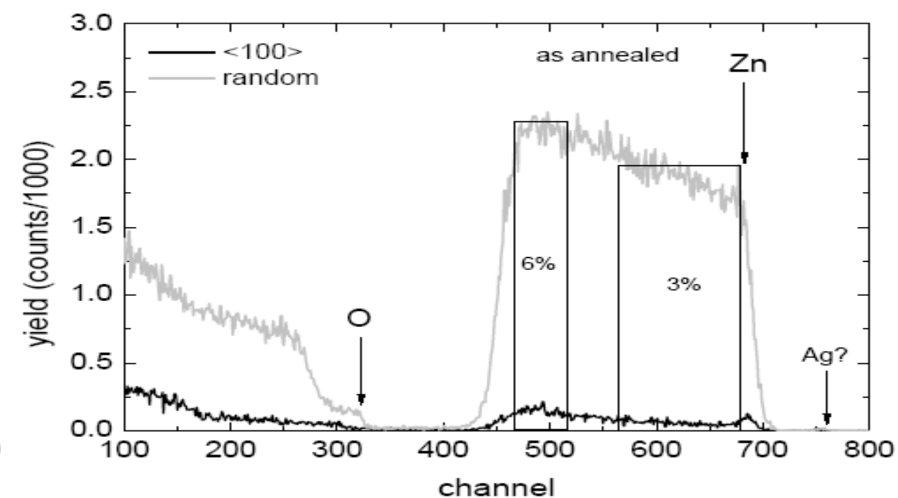

ZnO thin films

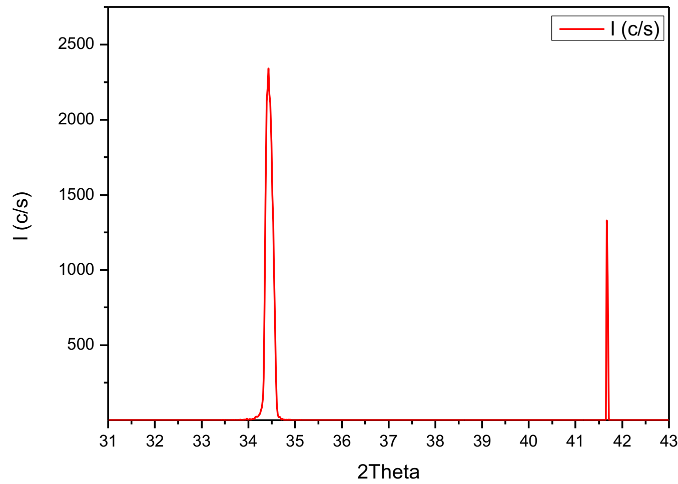

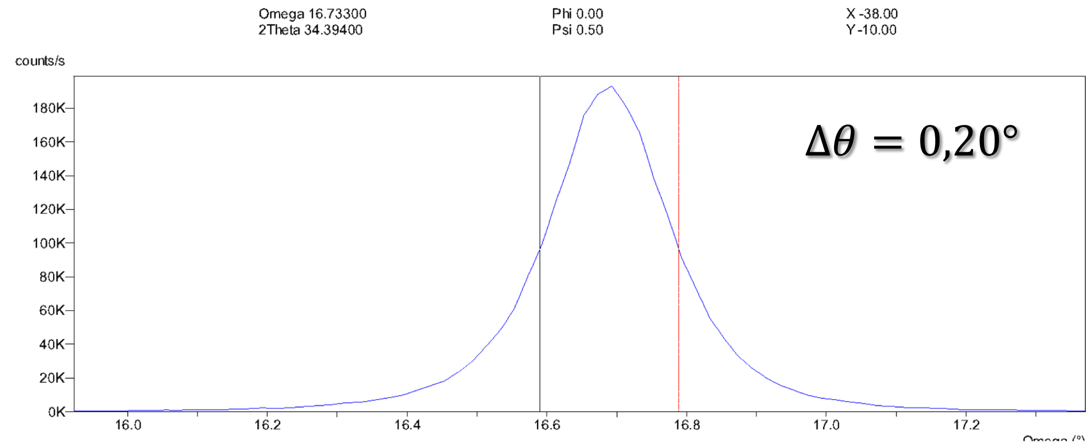

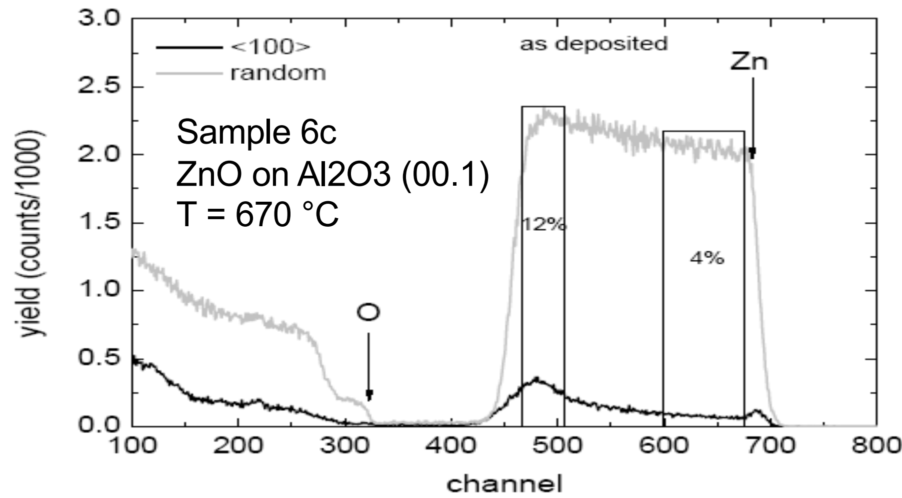

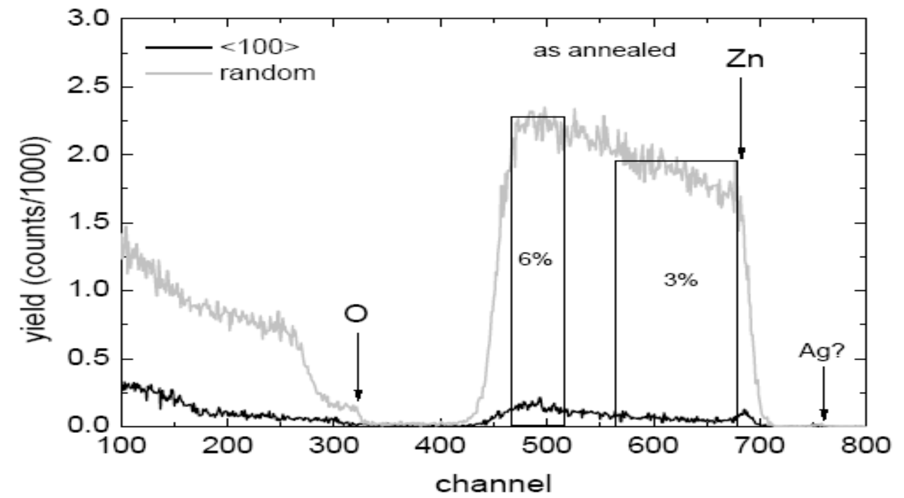

Current work

Co_{60}Fe40 very thin films for spinvalve and magnetic imaging applications

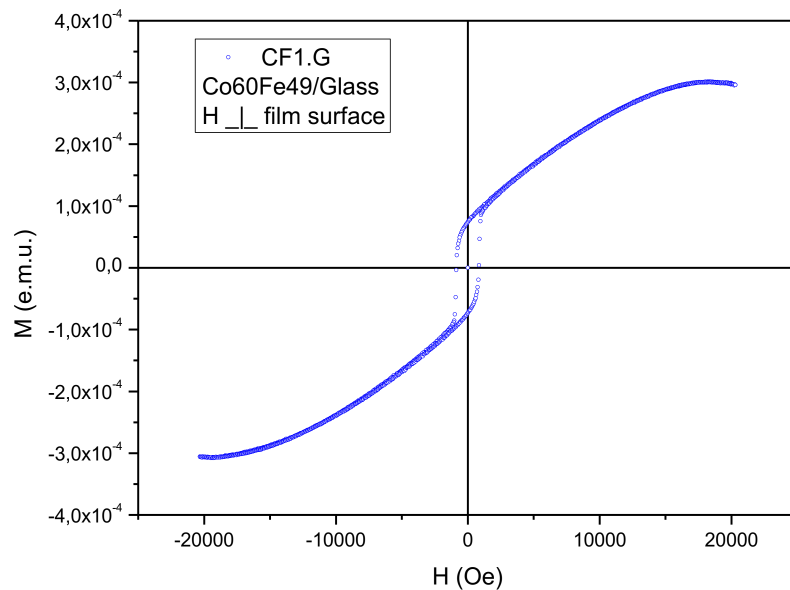

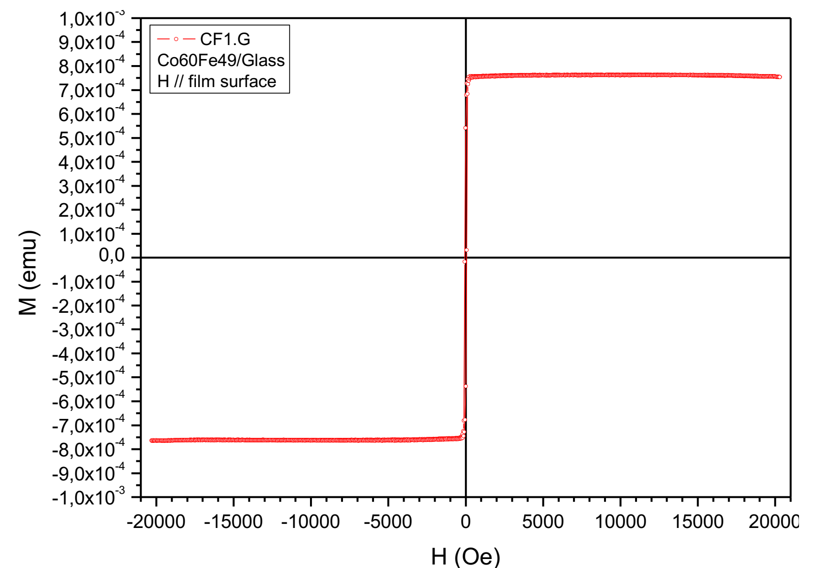

Current work

$Co_{60}Fe40$ very thin films for spinvalves and magnetic imaging applications

Parratt32 data output sheet
14/06/2023 16:08:53

sample parameters are:

	d / Å	rho / Å^-2	Im(rho) / Å^-2	sigma / Å
air	N/A	0E+0	0E+00	N/A
1	129,44	6,128E-5	8,5E-06	2,232
SiO2	29	1,891E-5	2,445E-07	7,274
bulk	N/A	2,015E-5	4,588E-07	4

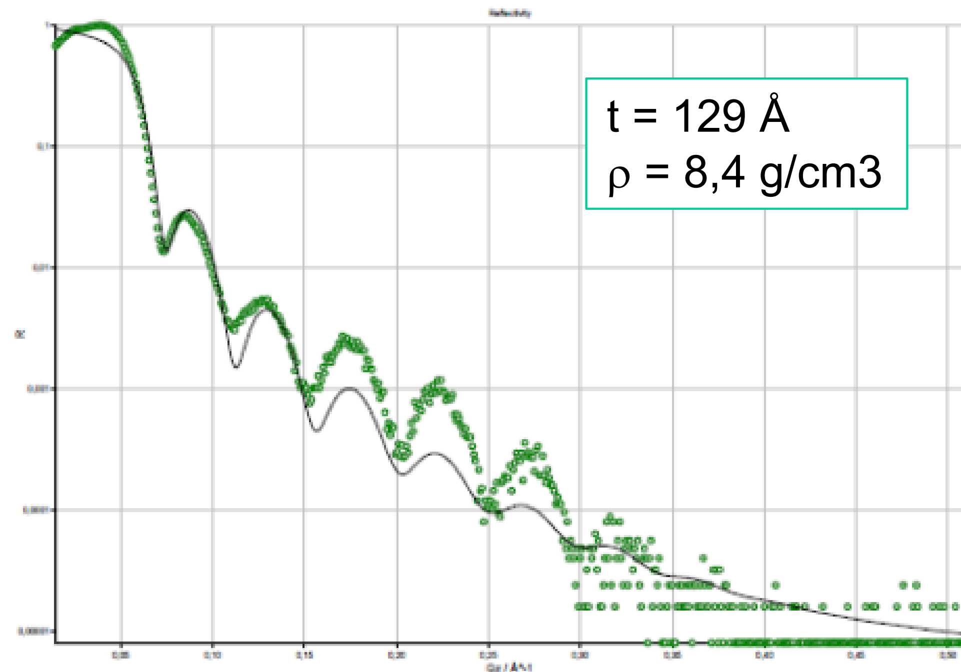

Parratt32 version 1.6 1997-2002by Christian Braun, HMI Berlin. Versions: 1.6 and 1.5. File name: Parratt.exe.

L.G. Parratt, *Phys Rev* **95**, 359 (1954)

XRD – X-ray sources

Table 1. The peak wavelengths on an absolute scale, λ, energies, E, full widths at half maximum, W, and asymmetry indices, σ_W, of the measured diagram lines. Measurement uncertainties are given in brackets. Wavelength to energy conversion is done using 806 554.477(32) $(\mathrm{eV\,m})^{-1}$ [75]. Note the 10^{-6} level of uncertainty of the present wavelength results.

Line	λ (nm)	E (eV)	W (eV)	σ_W
$CuK\alpha_1$	0.154 059 29 (5)	8047.83 (1)	2.29 (2)	1.07
$CuK\alpha_2$	0.154 442 74 (5)	8027.85 (1)	3.34 (6)	1.36
$CuK\beta_{1,3}$	0.139 223 4 (6)	8905.42 (4)	5.92	

Cu

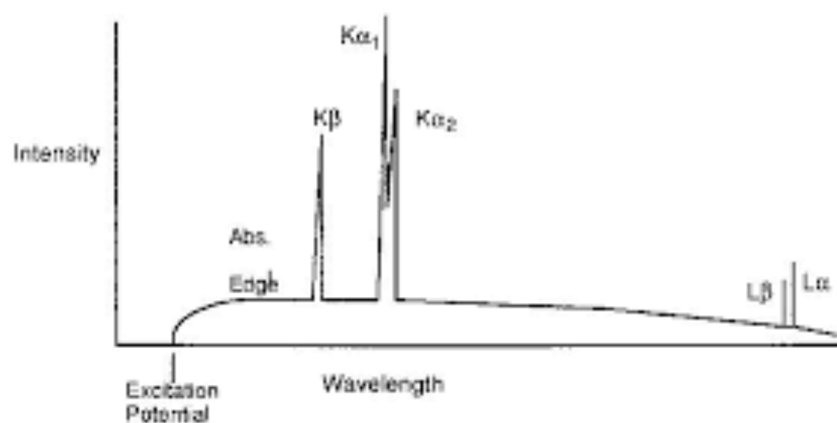

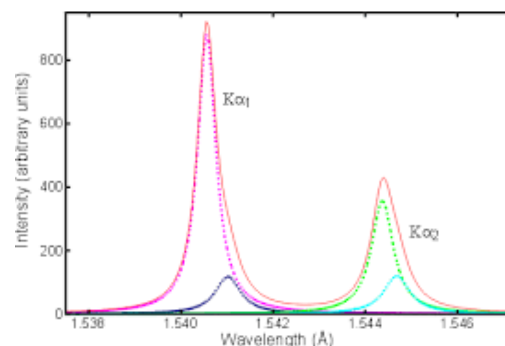

Mo

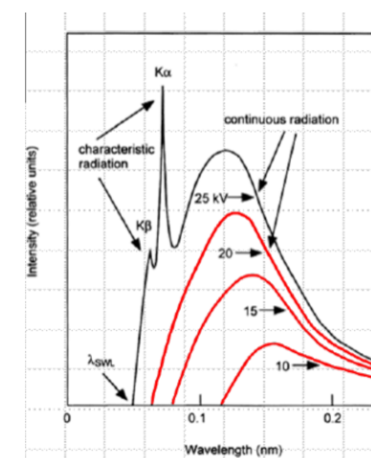

XRD – Bragg-Brentano

- Na geometria de Bragg-Brentano o vector difracção, $\boldsymbol{Q}$ é sempre perpendicular à superfície da amostra, $\Longrightarrow w = \theta$

- O vector difracção $\boldsymbol{Q}$ é o vector que bissecta o ângulo entre o raio incidente e o raio difractado

- Durante as medidas, a fonte está fixa, a amostra roda θ e o detector roda 2θ (sobre o círculo de focagem)

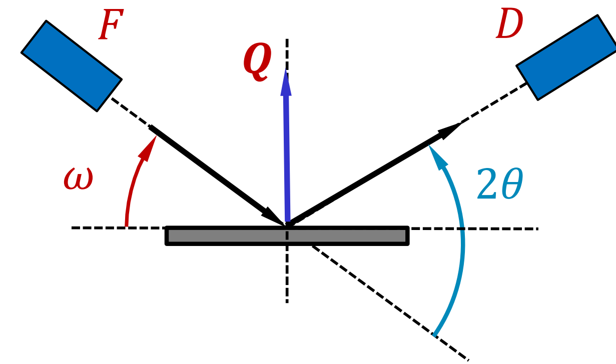

$$n\lambda = 2d\sin\theta$$

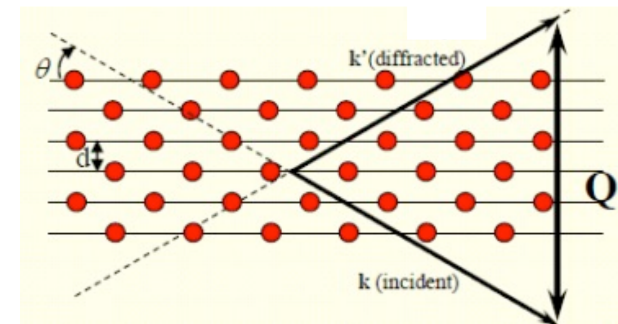

XRD – Bragg-Brentano

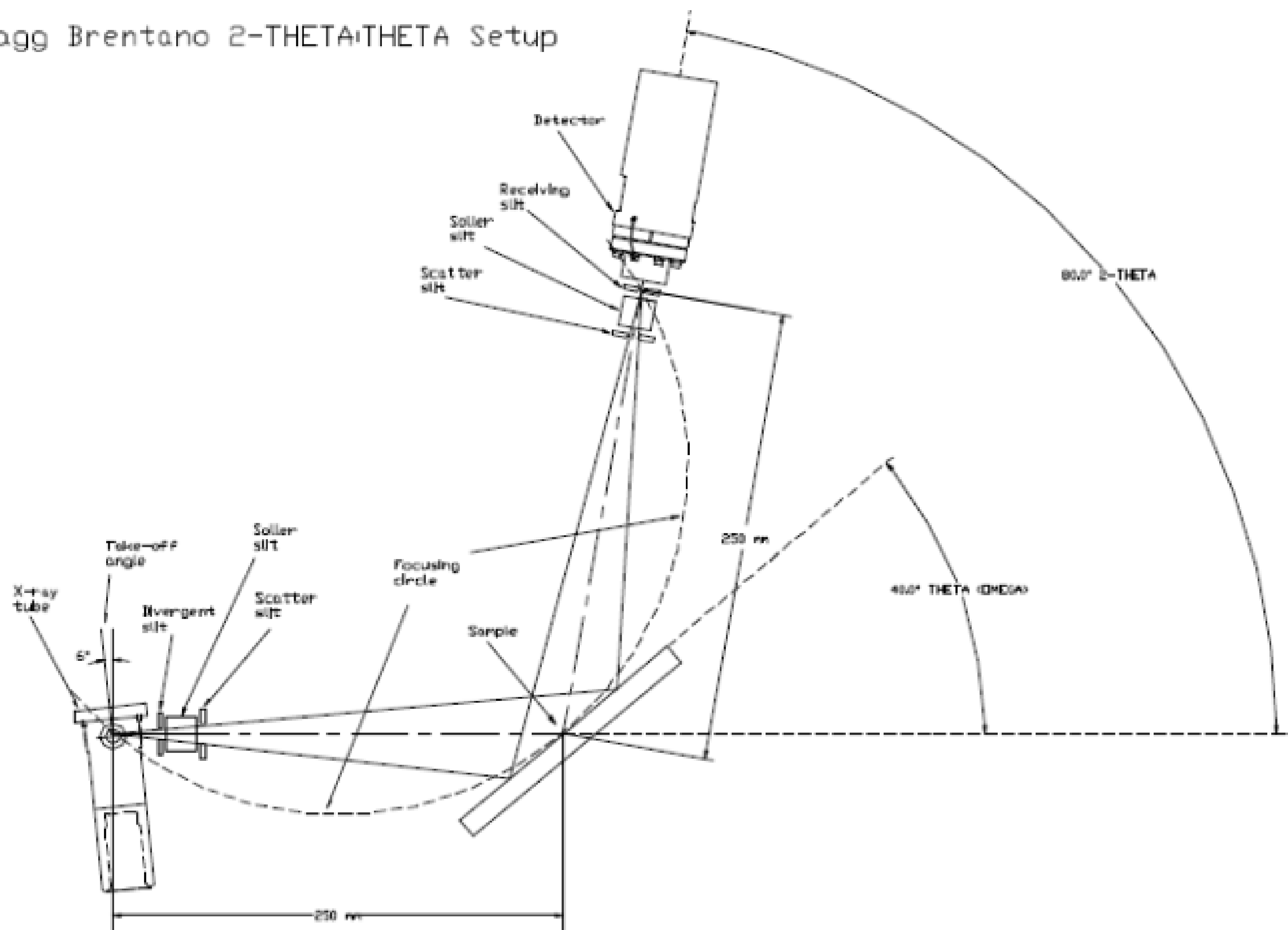

XRD – Bragg-Brentano

ZnO on saphire

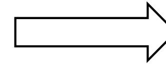

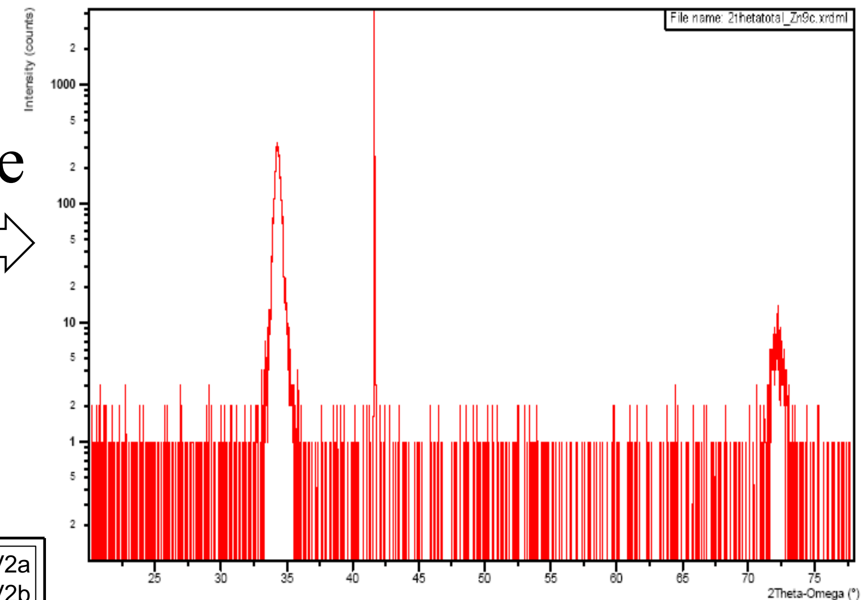

$GdVO_4:Eu^{3+}$ thin films on different substrates

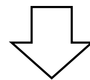

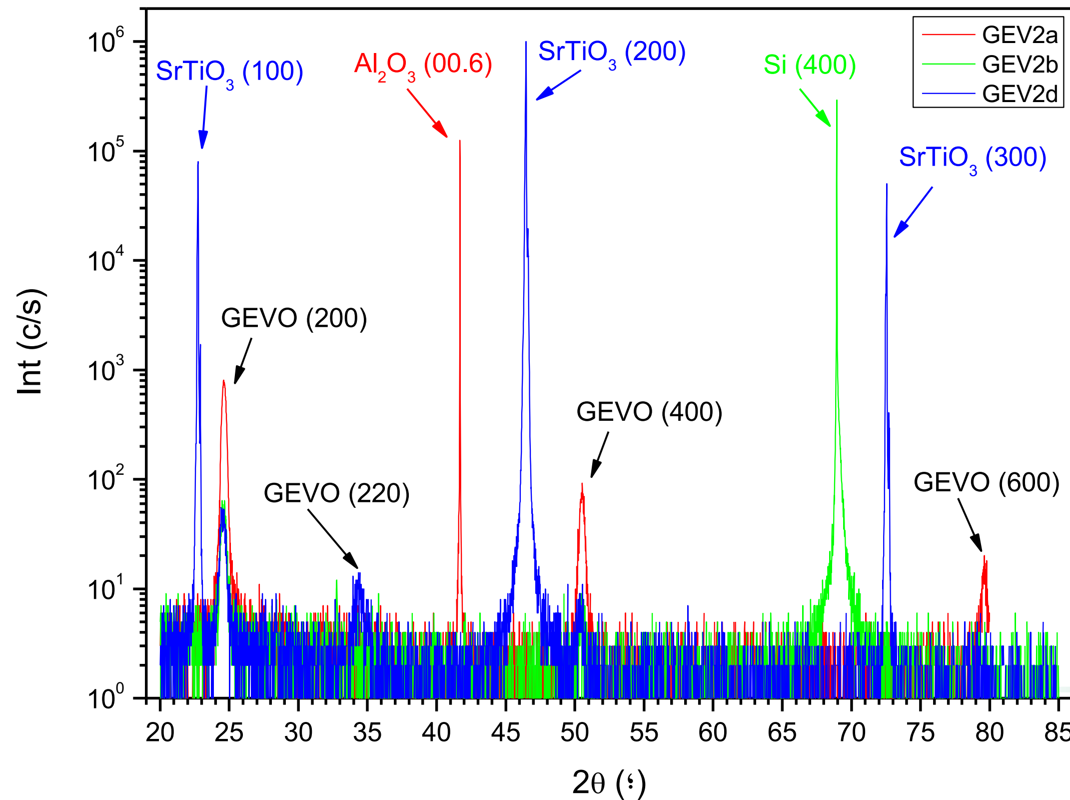

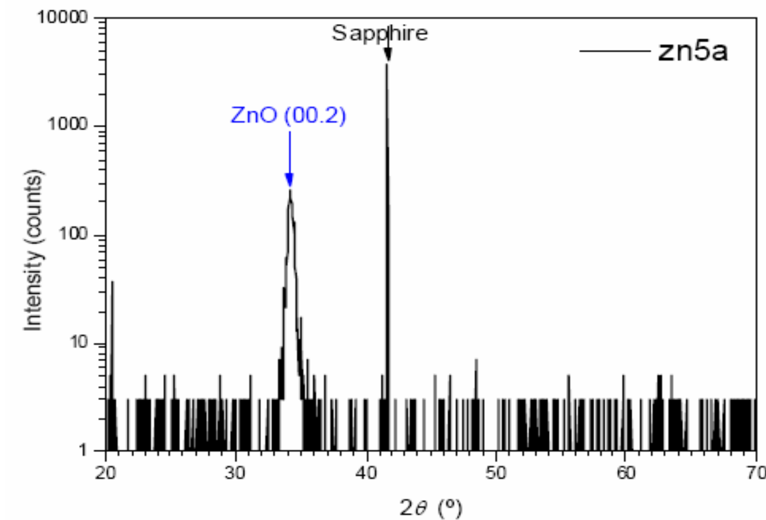

XRD – Rocking curve

- Omega scan, w, source and detector fixed (2θ fixed)
- Detecta desvios no paralelismo dos planos cristalinos (devido a deslocações, curvatura, rotação de domínios, etc)
- Um cristal perfeito produz um pico muito estreito (largura instrumental e intrínseca do material)
- O pico é observado apenas quando a direcção cristalográfica é paralela ao vector $\boldsymbol{Q}$

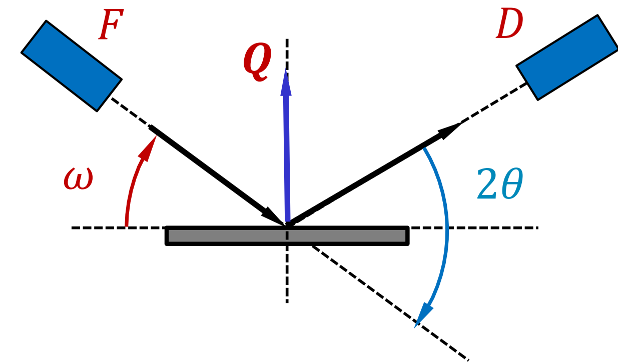

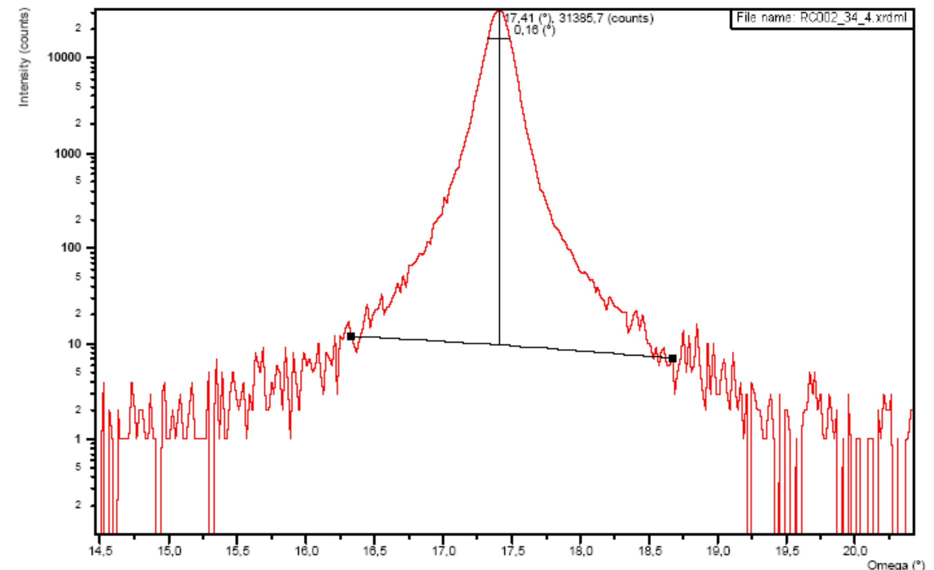

XRD – Poles ($\phi - scan$)

- Distribuição das orientações cristalográficas (in plane)
- Estudo da anisotropia estrutural no plano
- Registo da intensidade para um dado 2θ em função da rotação ϕ

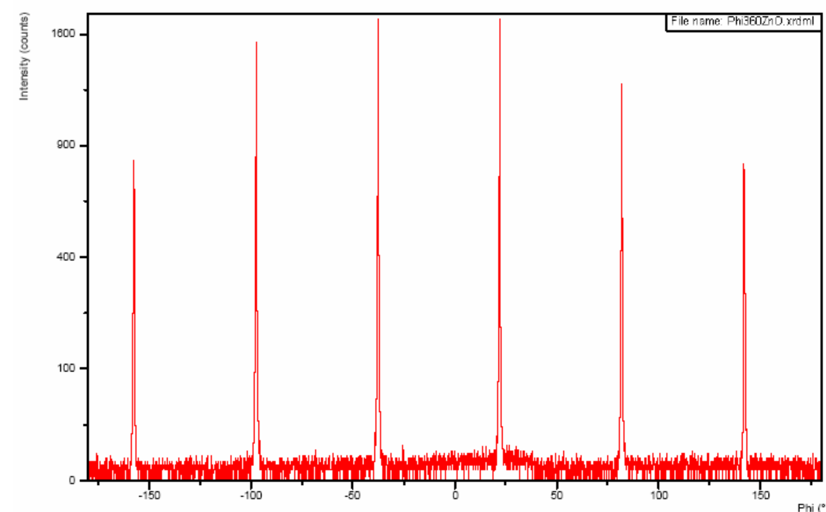

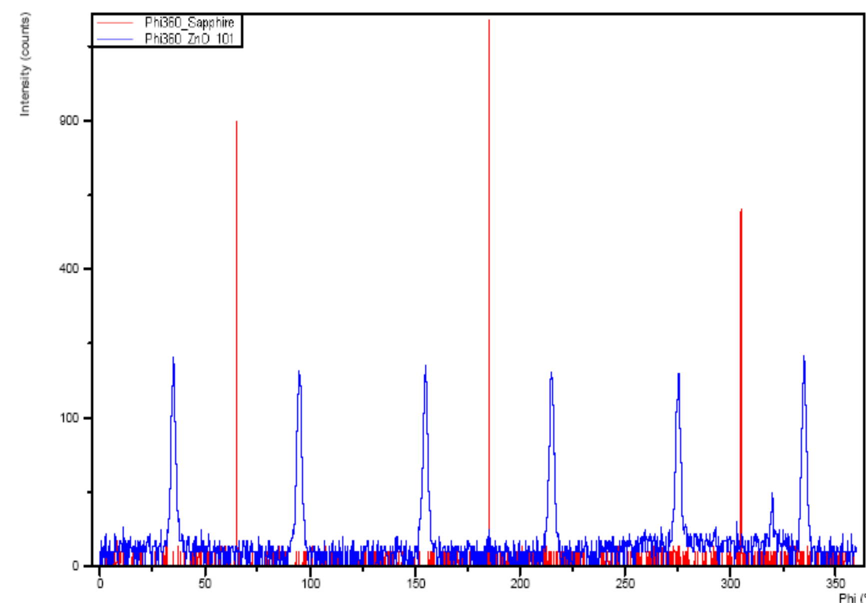

XRD – Texture ($\phi - \psi\ scan$) contour maps

- Distribuição das orientações cristalográficas (in plane)
- Estudo da anisotropia estrutural no plano
- Registo da intensidade para um dado 2θ em função da rotação ϕ e da inclinação ψ – para cada ψ uma rotação completa em ϕ

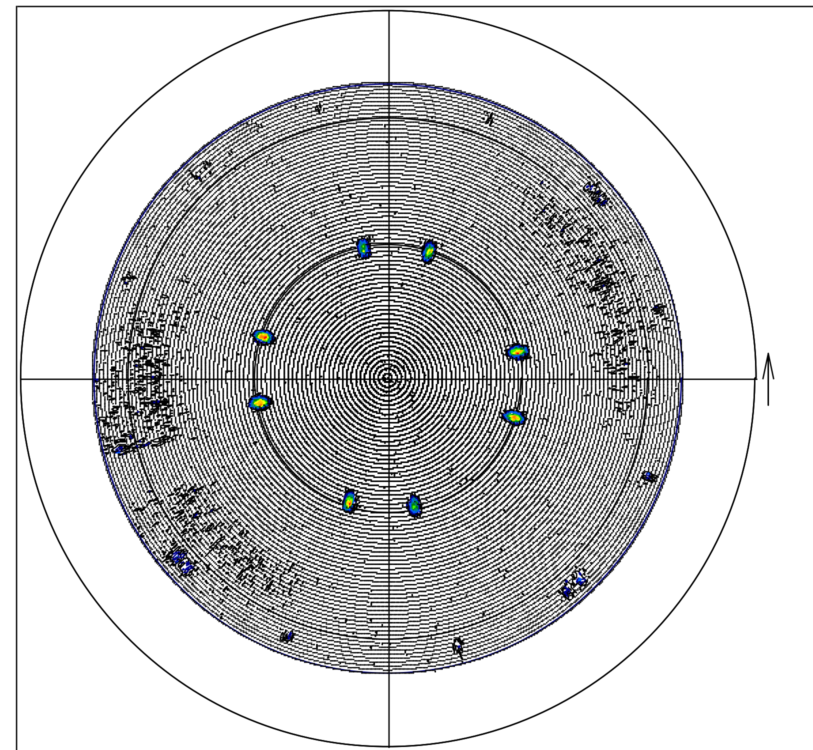

XRD – Reciprocal Space Maps (omega-2θ scans)

Do espectro de Bragg $(\theta - 2\theta)$ seleccionamos um máximo e em torno desse máximo fazemos um varrimento em $w \rightarrow$ para cada valor de 2θ fazemos uma "rocking curve", na zona de interesse

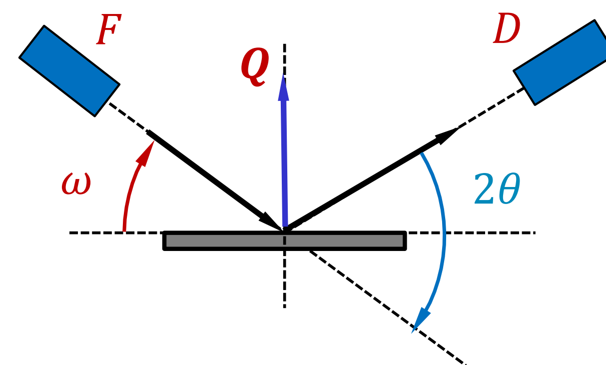

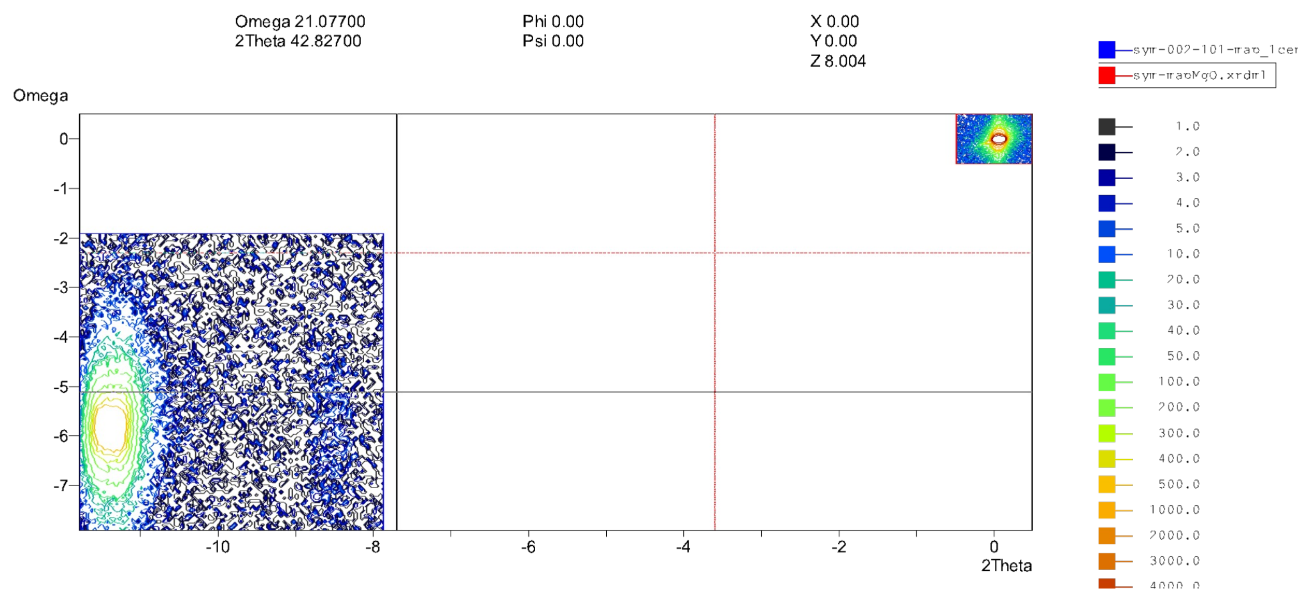

ZnO on MgO (100)

XRD – Reciprocal Space Maps (omega-2θ scans)

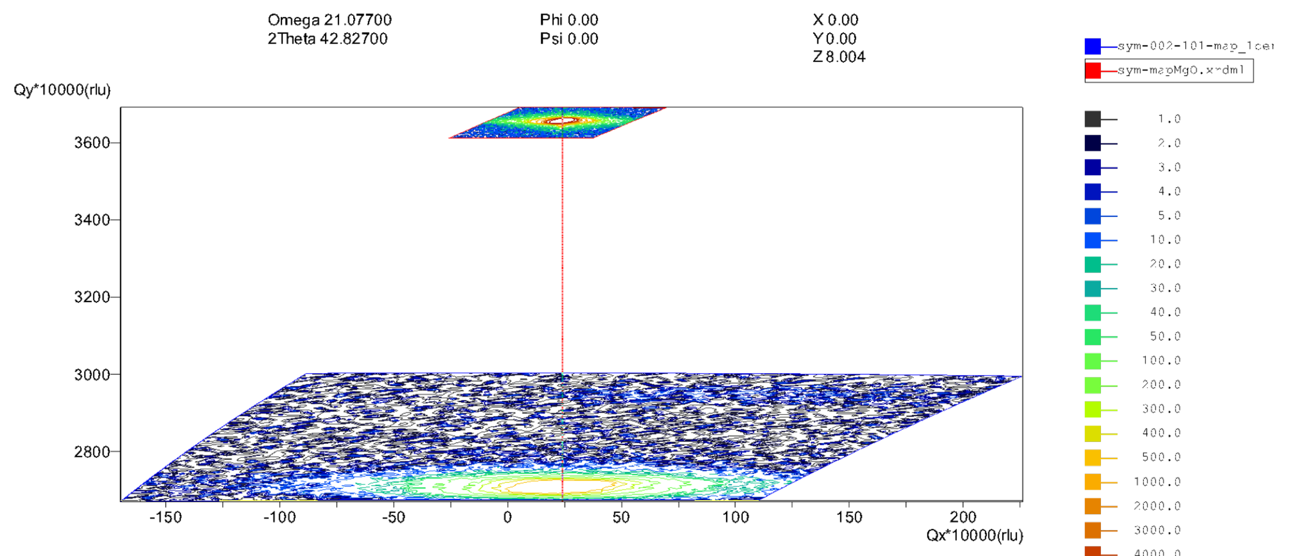

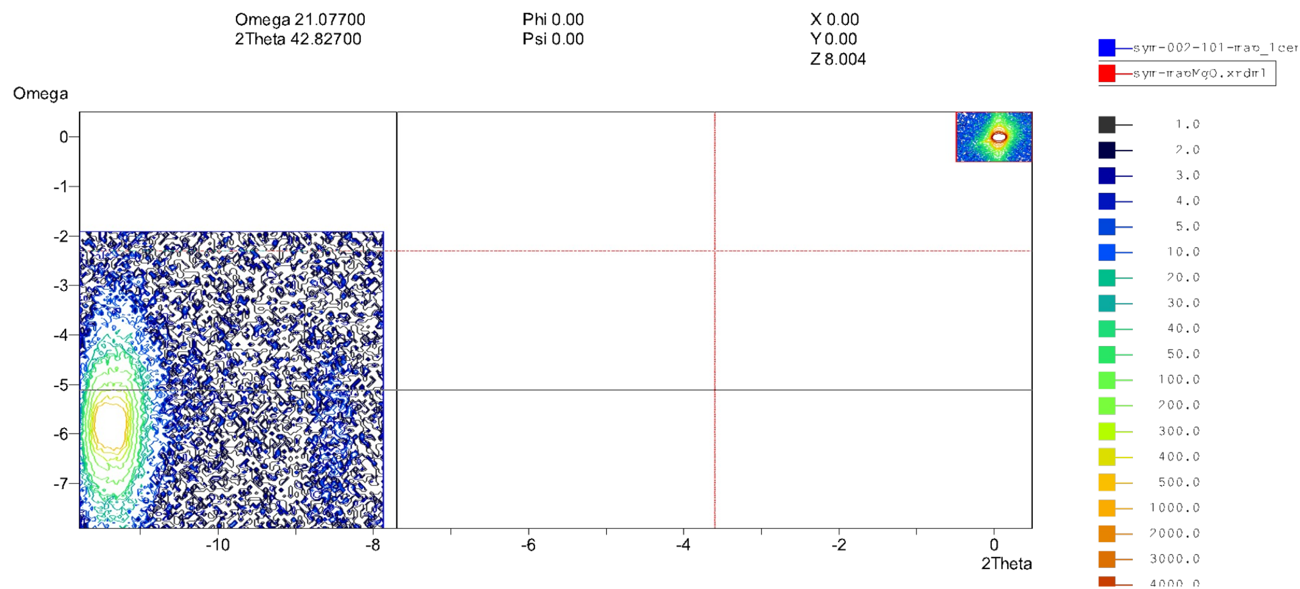

ZnO on MgO (100)

XRD – Reciprocal Space Maps (omega-2θ scans)

Substrate influence

ZnO on sapphire (Al_2O_3)

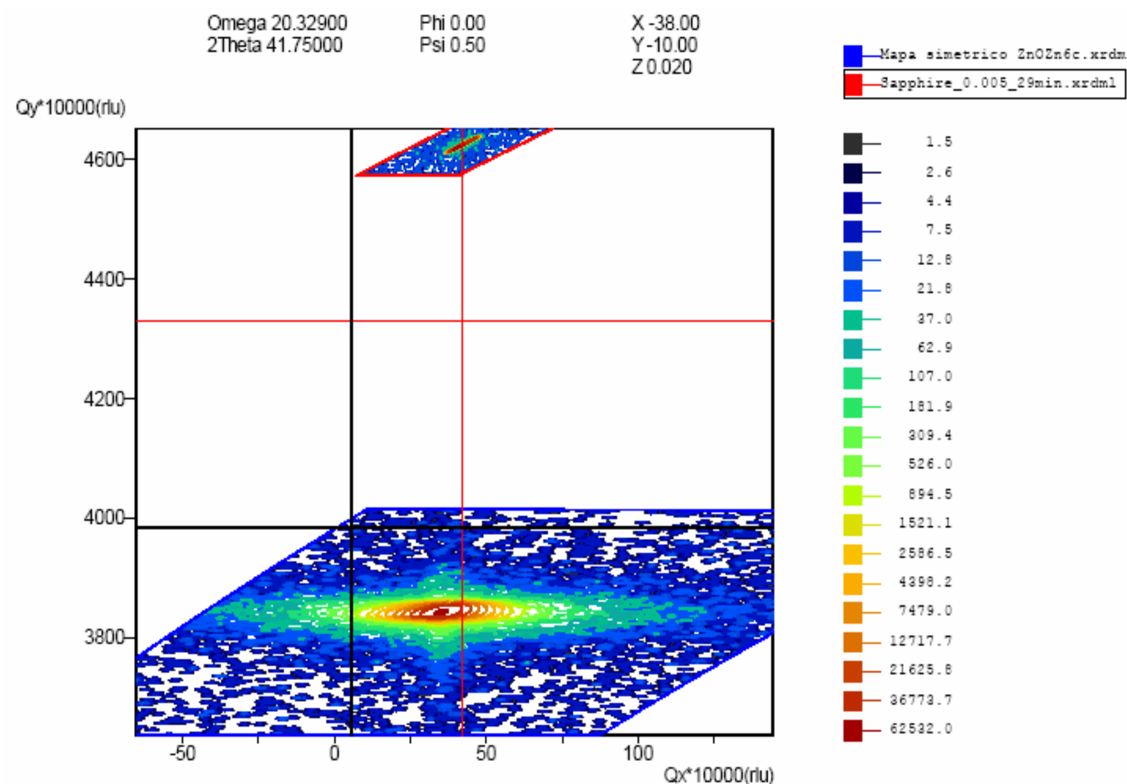

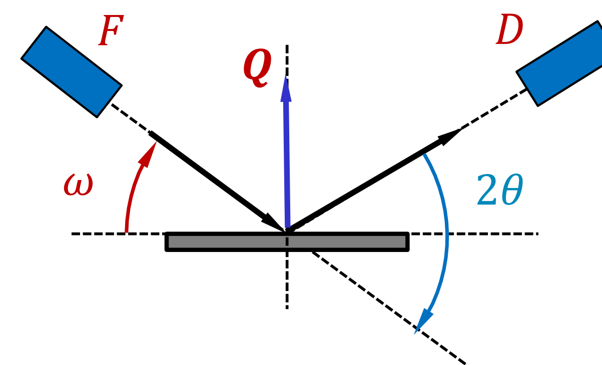

ZnO on Al_2O_3 (00.1)

XRD – Reciprocal Space Maps (omega-2θ scans)

- ZnO sobre SrTiO3 (100)

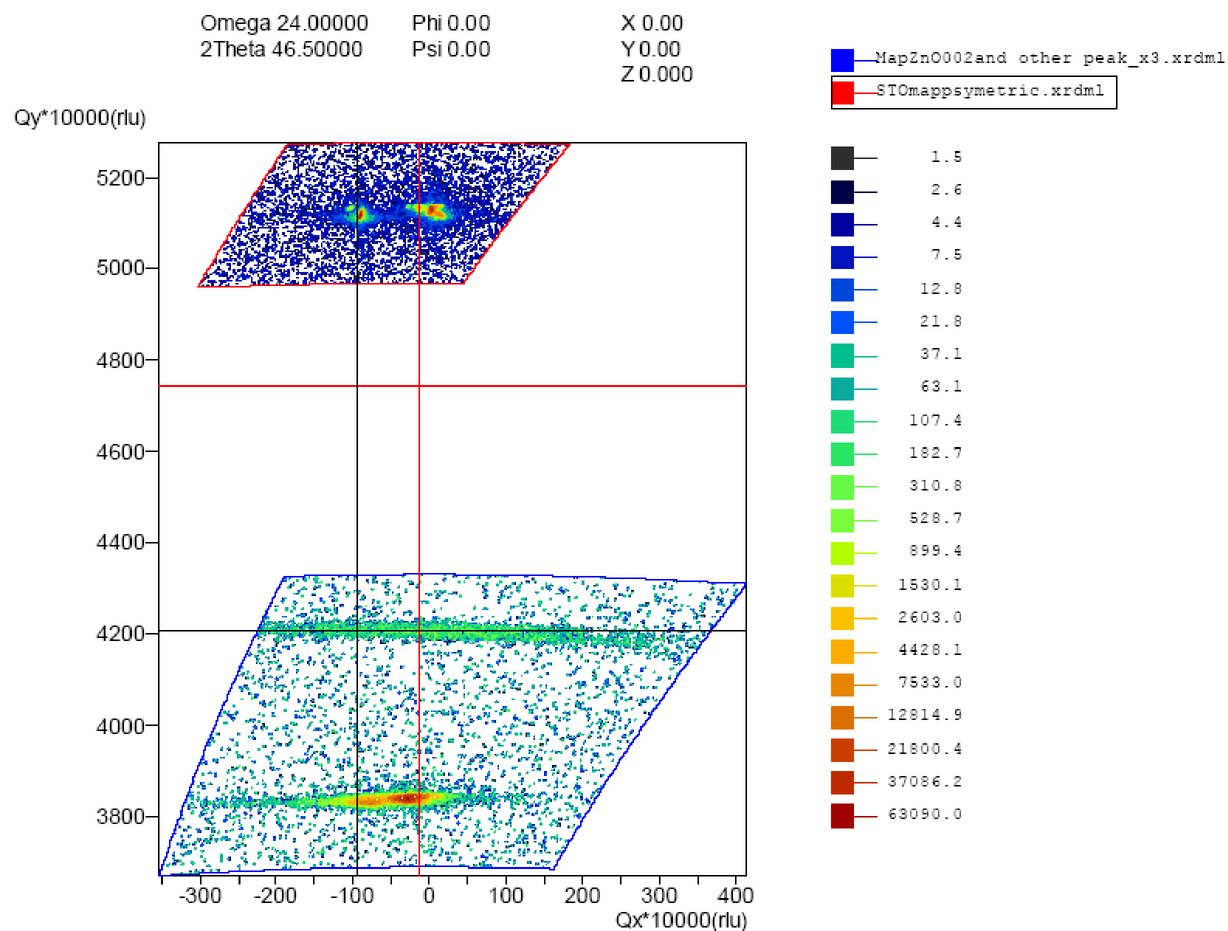

XRD – Reciprocal Space Maps (omega-2θ scans)

- ZnO on $SrTiO_3$ (100) substrate twin planes detected → ***the substrate is not a monocrystal***

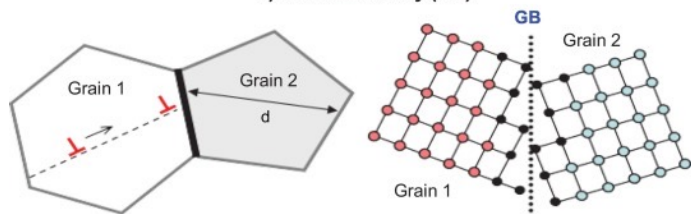

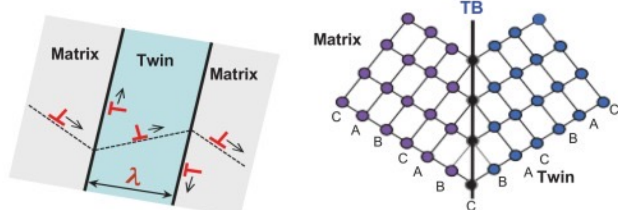

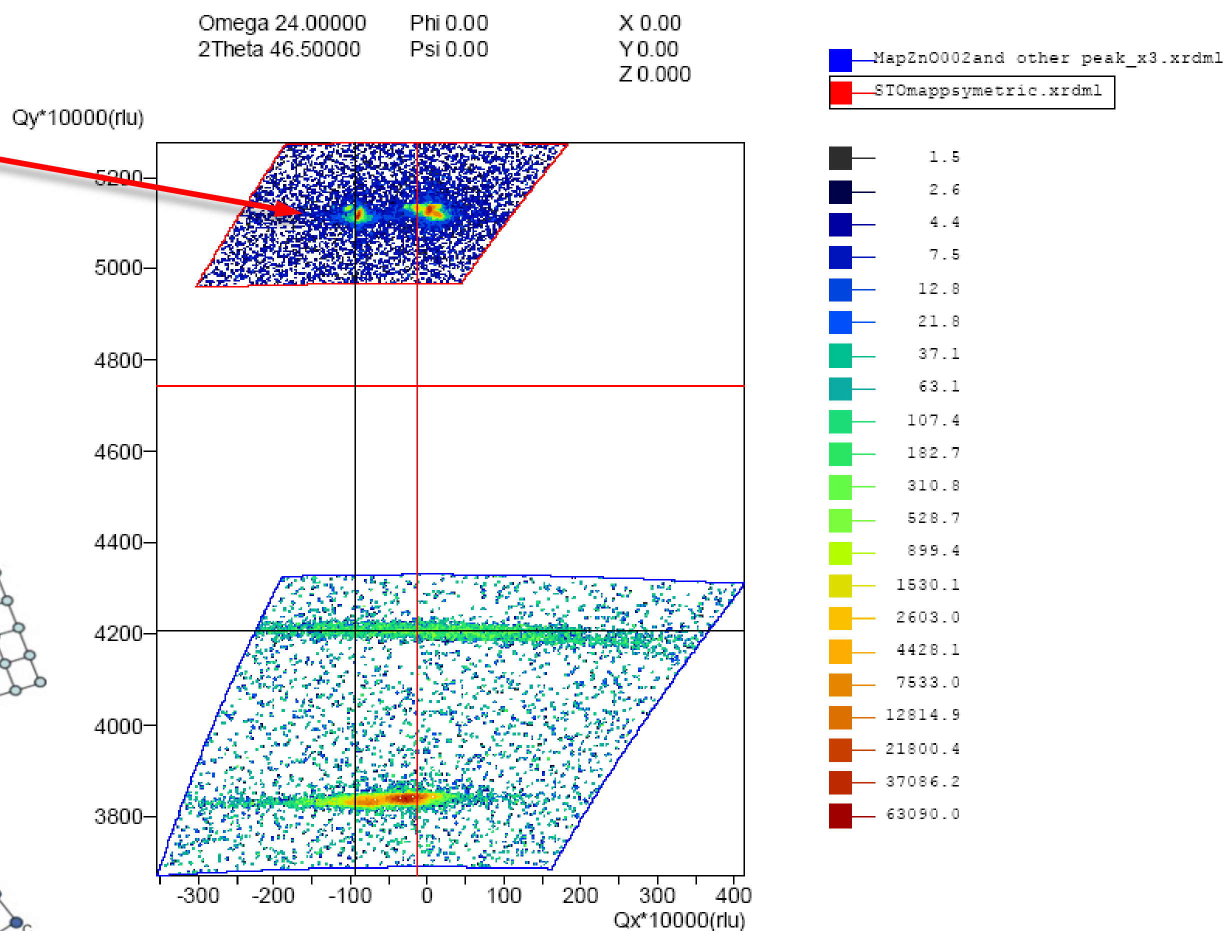

XRD – Reciprocal Space Maps (omega-2θ scans)

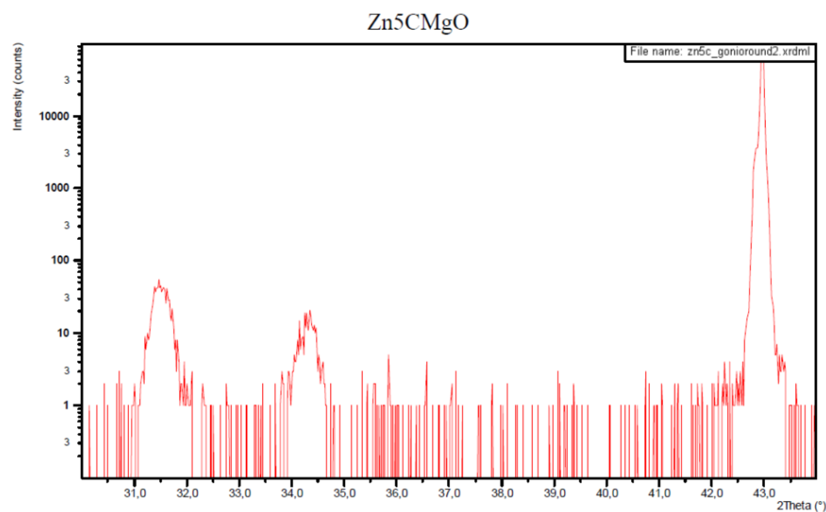

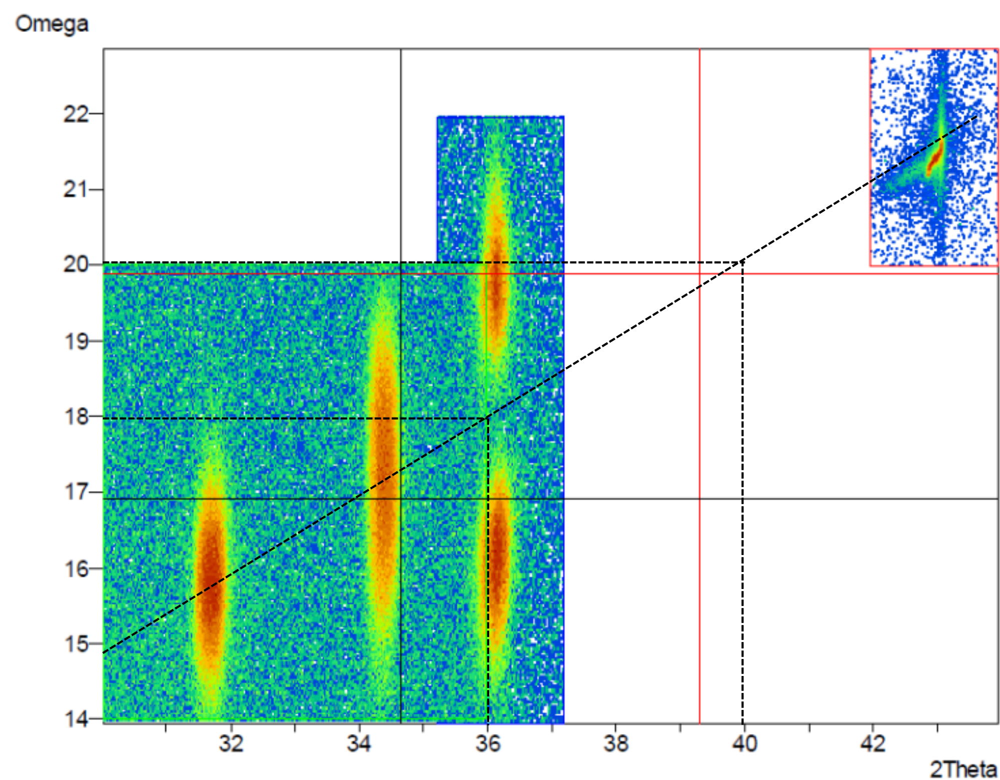

XRD – Reciprocal Space Maps (omega-2θ scans)

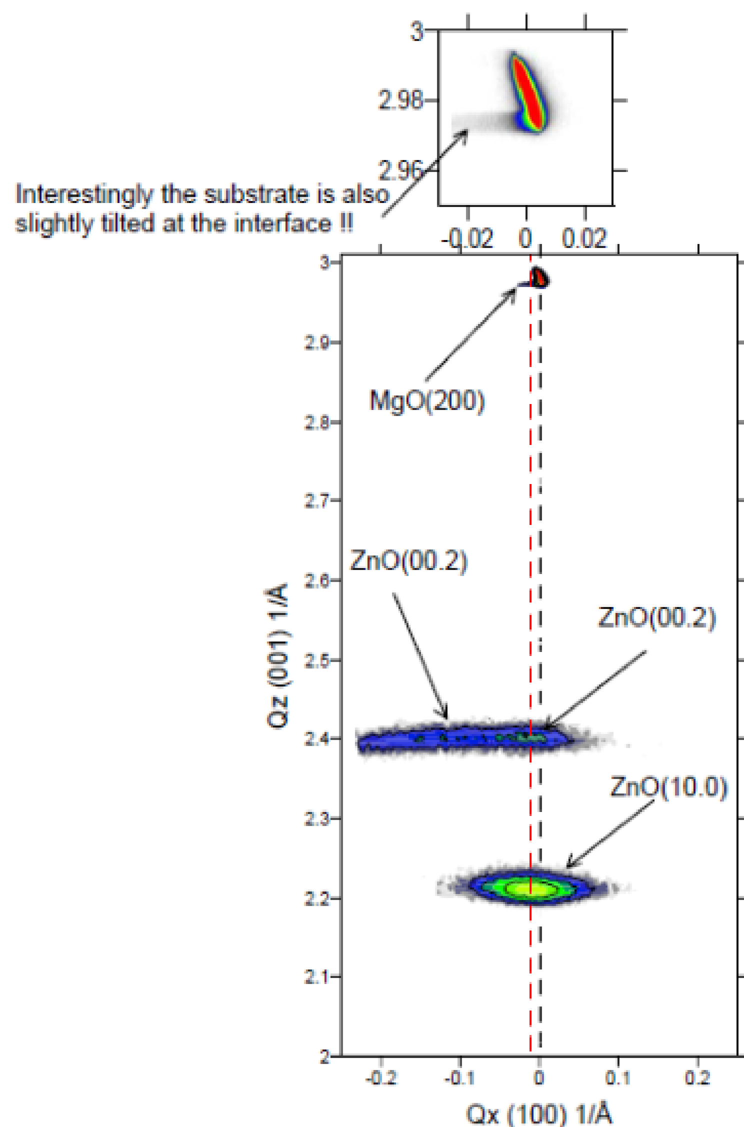

ZnO on MgO (200)

- substrate is slightly tilted at the interface
- ZnO (10.0) grows initially aligned with the substrate
- Após uma dada espessura começa a desenvolver-se uma estrutura inclinada, o crescimento mais comum do ZnO (00.2)
- As duas estruturas coexistem nesta região do filme

4. Analysis

XRD – Grazing Incidence

$w = 2°$

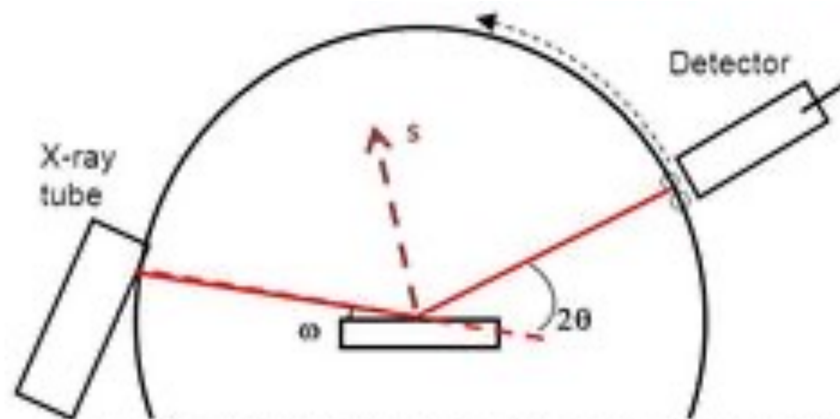

- The incident angle, ω, is set to a very shallow angle (between 0.2 and 5 deg).
  - This causes the X-rays to be focused in the surface of the sample, limiting the penetration depth of the X-rays
- Only the detector moves during data collection
  - The value τ is changing during the scan (where τ = ½*2θ – ω)
  - As a consequence, the diffraction vector (s) is changing its direction during the scan
- Remember the diffraction only comes from crystallites in which dhkl is parallel to s
  - Therefore, the direction being probed in the sample changes
  - This is perfectly ok for ideal samples with randomly oriented grains; however, for samples with preferred orientation this will cause a problem.
- Regular GIXD will constrain the X-ray beam in the top few microns of the surface
- IP-GIXD can be configued to constrain diffraction to the top 10-20 nm of the surface.

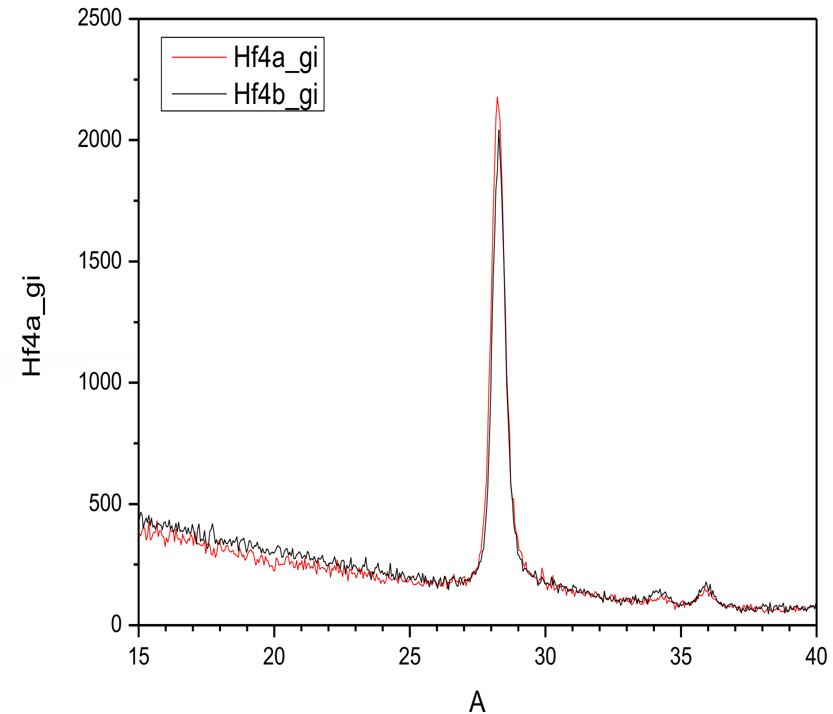

Thickness

Hf4a – 278 Å

Hf4b – 280 Å

4. Analysis

XRR – X-Ray Reflectometry

Heinz Kiessig fringes – interferência da radiação reflectida na interface e na superfície de Ni sobre vidro em 1931

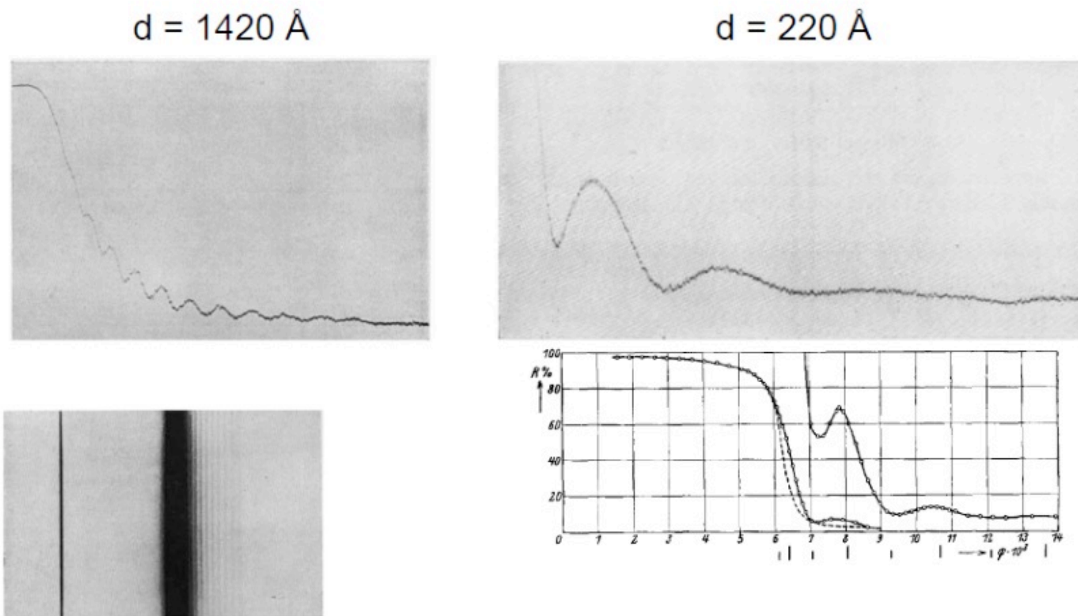

Kiessig, Heinz (1931). "Untersuchungen zur Totalreflexion von Röntgenstrahlen". *Annalen der Physik* **402** (6): 715–768

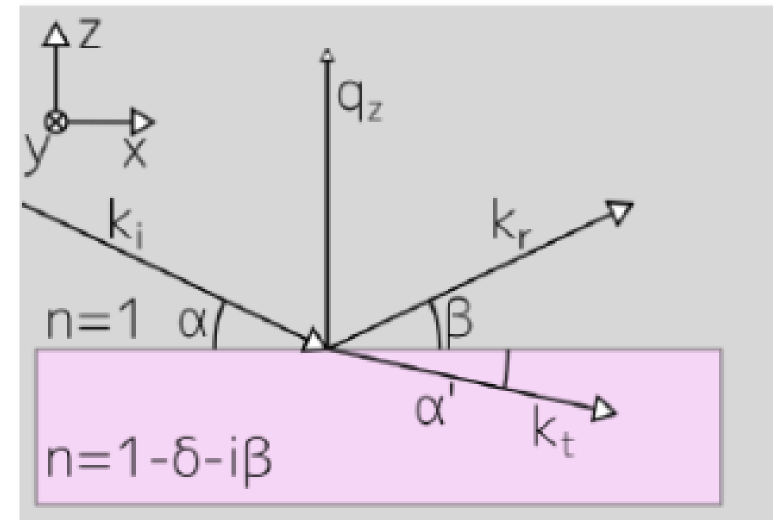

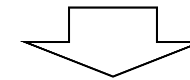

- Varrimento $\theta - 2\theta$
- $q_x = q_y = 0, q_z \neq 0$
- apenas informação na direcção normal à superfície

4. Analysis

XRR – X-Ray Reflectometry

Acess

- Film thickness
- Film density
- Interface roughness
- Surface roughness
- electronic density profile along the normal direction

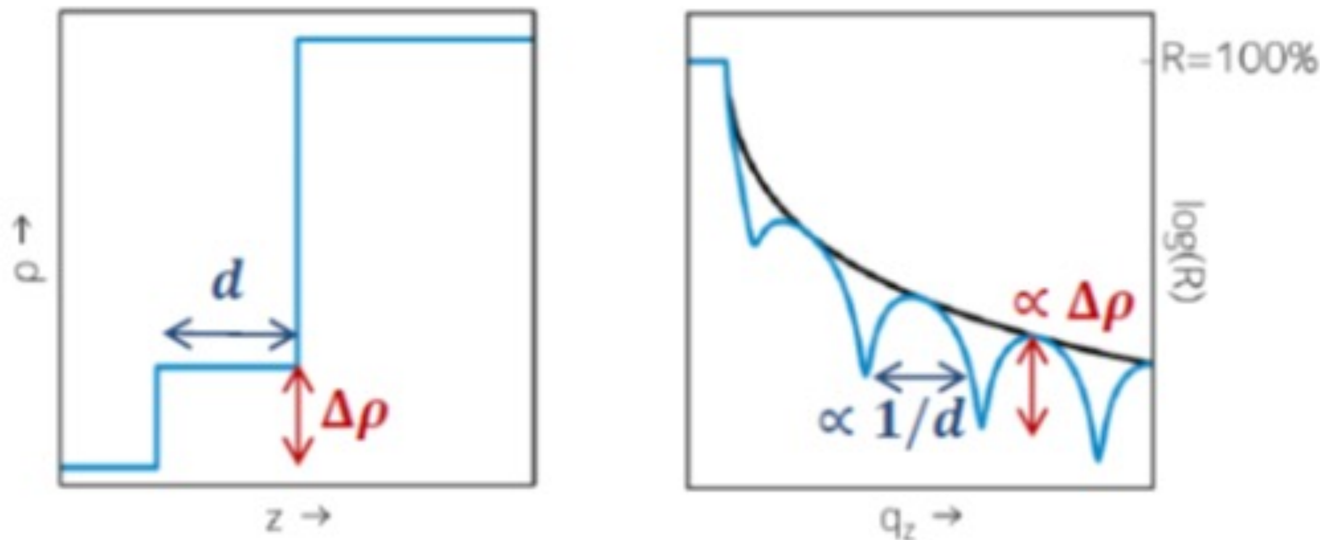

4. Analysis

Microscopy – A.F.M.

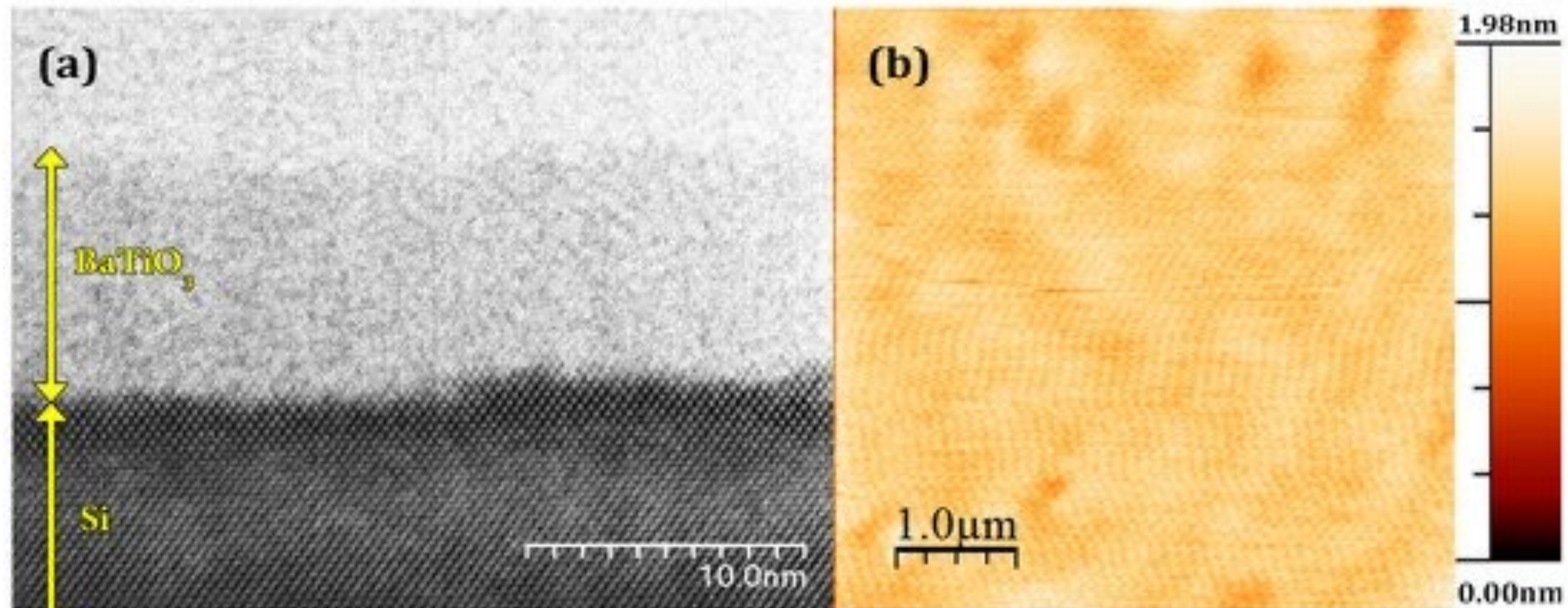

Figure 1. (a) Bright field STEM image of a 5.6 nm-thick BaTiO3 film on Si substrate and (b) topography of the film before poling (RMS roughness 0.18 nm).

"Giant Strain and Induced Ferroelectricity in Amorphous BaTiO3 Films under Poling", Pegah Mirzadeh Vaghefi, Ali Baghizadeh, Armando A.C.S. Lourenço, Vitor S. Amaral and Andre L. Kholkin, *Materials* 2017, 10, 1107; doi:10.3390/ma10091107

4. Analysis

Caracterização magnética –magnetização

Magnetização - resposta dos materiais à aplicação de campos magnéticos

Classificação dos materiais dependendo das suas propriedades e valor da permeabilidade (susceptibilidade $-1 \leq \chi < \infty$)

Três grupos principais

- Diamagnéticos ($\chi = -1, \sim 10^{-5}$)
- Paramagnéticos
- Ferromagnéticos

Ainda mais dois grupos

- Ferrimagnéticos
- Antiferromagnéticos

4. Analysis

Caracterização magnética –magnetização

Magnetização - resposta dos materiais à aplicação de campos magnéticos

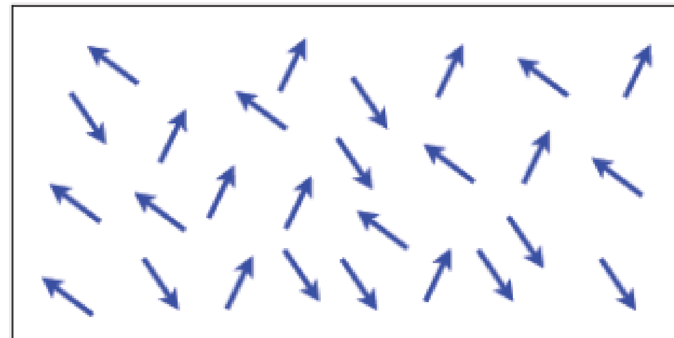
Paramagnet

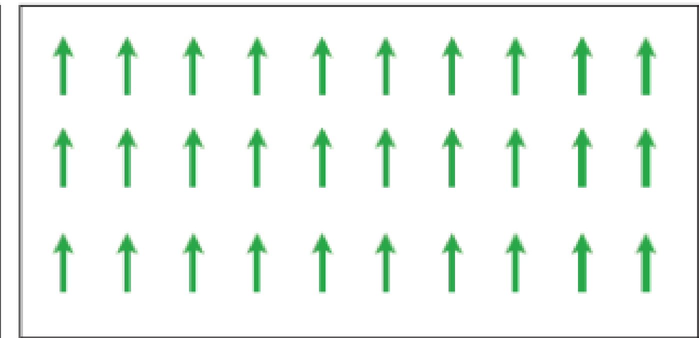
Ferromagnet

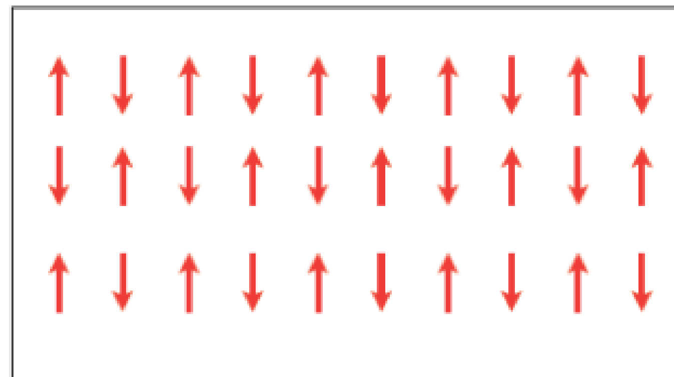
Anti-ferromagnet

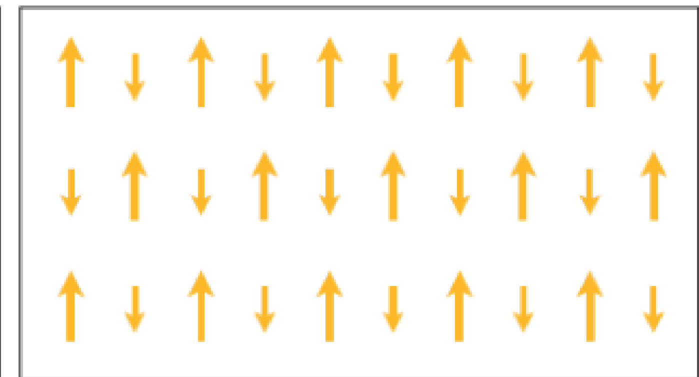
Ferrimagnet

4. Analysis

Caracterização magnética –magnetização

Magnetização - resposta dos materiais à aplicação de campos magnéticos

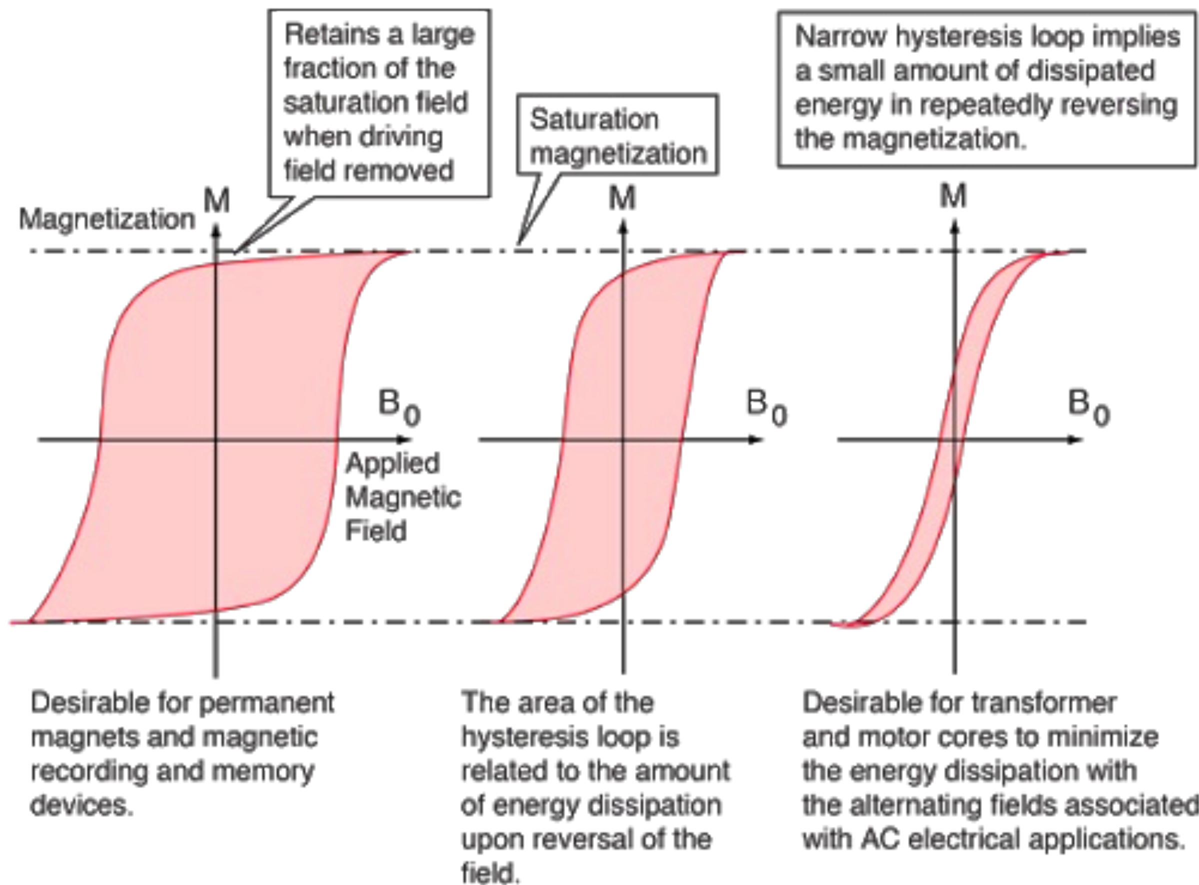

Ferromagnetismo

Ciclos histeréticos

4. Analysis

Caracterização magnética –magnetização

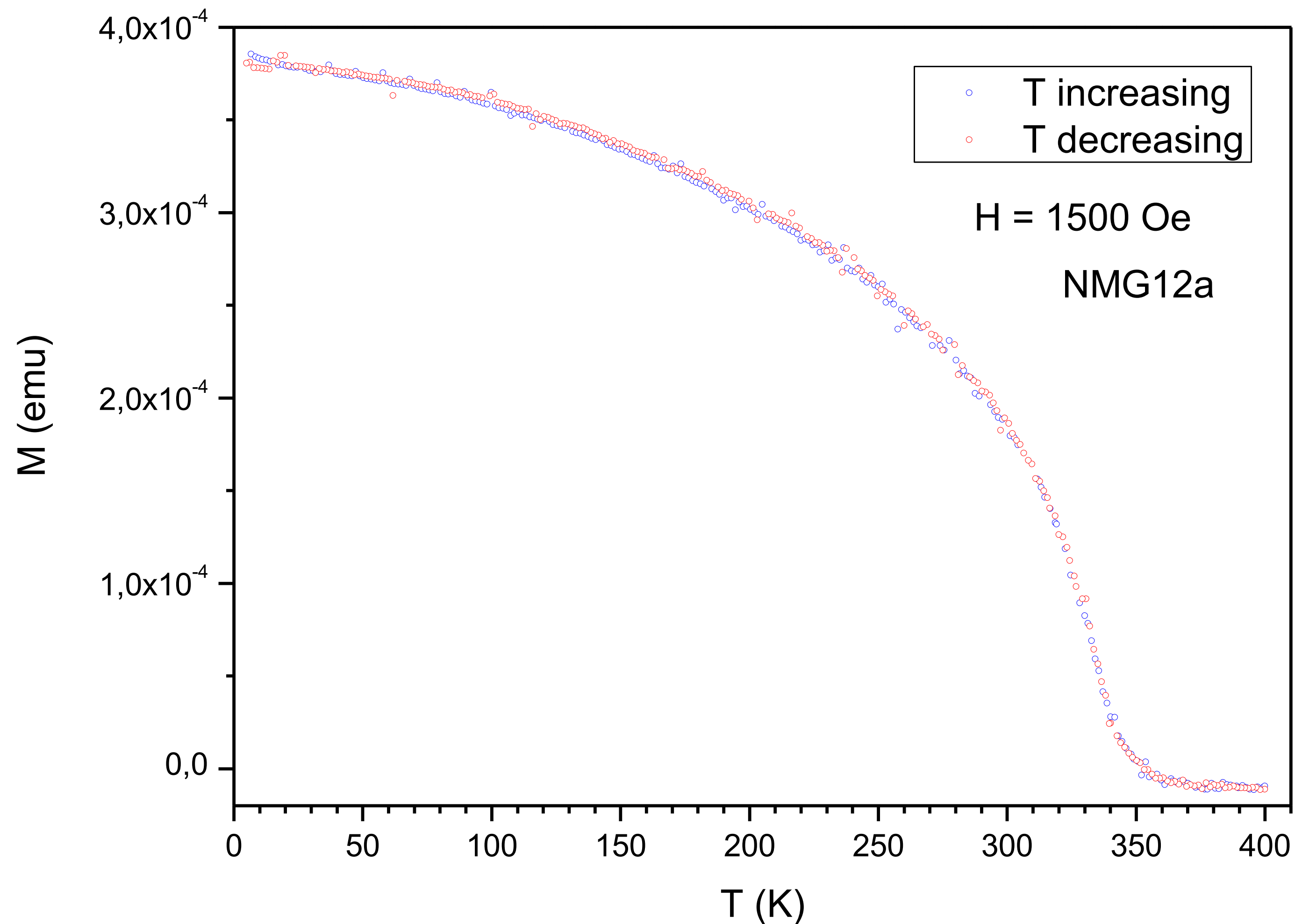

4. Analysis

Caracterização magnética –magnetização

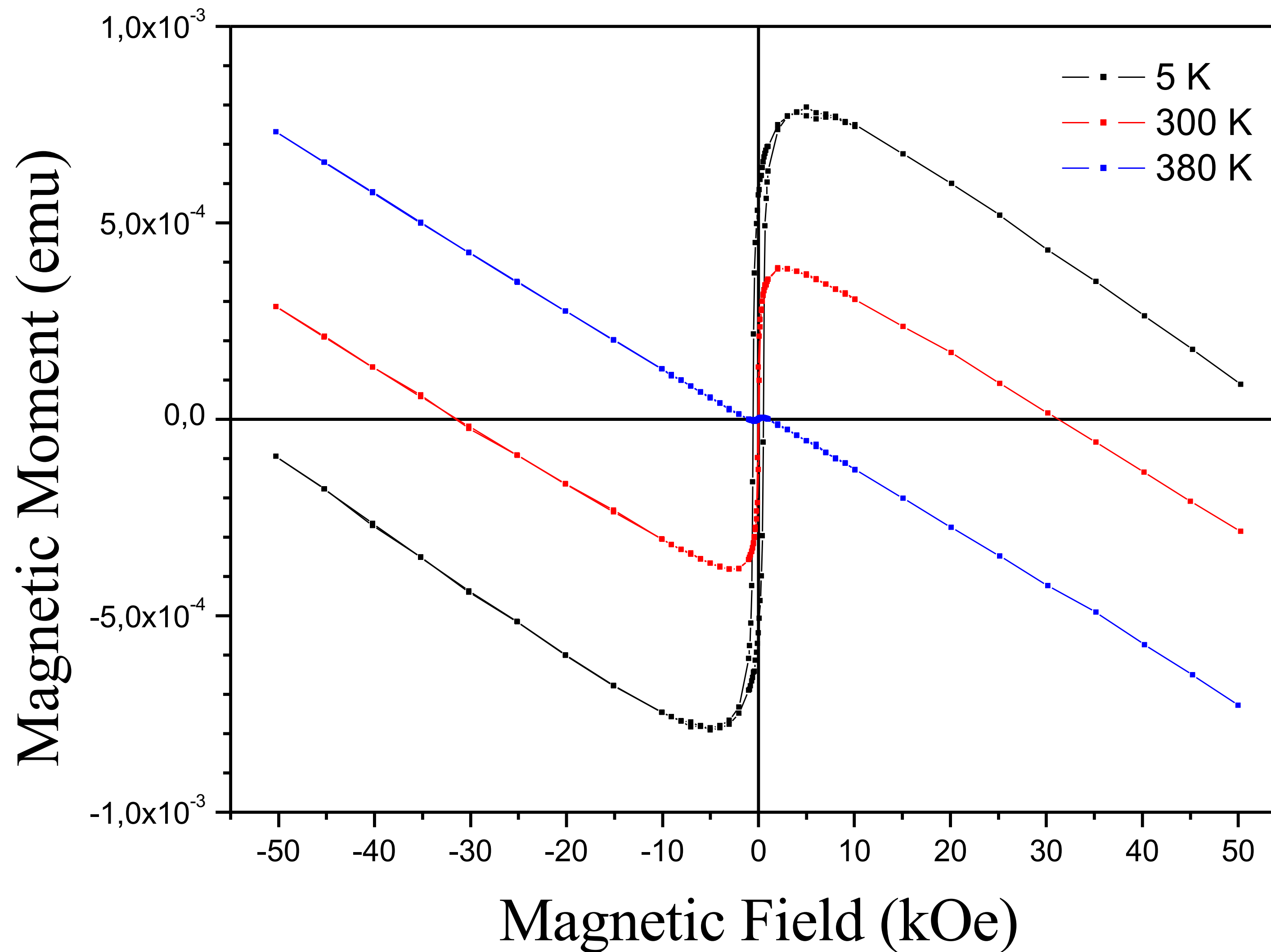

Hardware

- To build or not to build ?
- That was the question

Not to build $\Rightarrow$ to buy $\Rightarrow$ a lot of money...

To build $\Rightarrow$ not so big money...(to start)

$\Rightarrow$ know how... and a lot of patience

Financial support

- POCTI/CTM35462/2000
- CICECO

Hardware

Ponto de partida: escolha das fontes (o coração do sitema), Magnetrão plano de 2”.

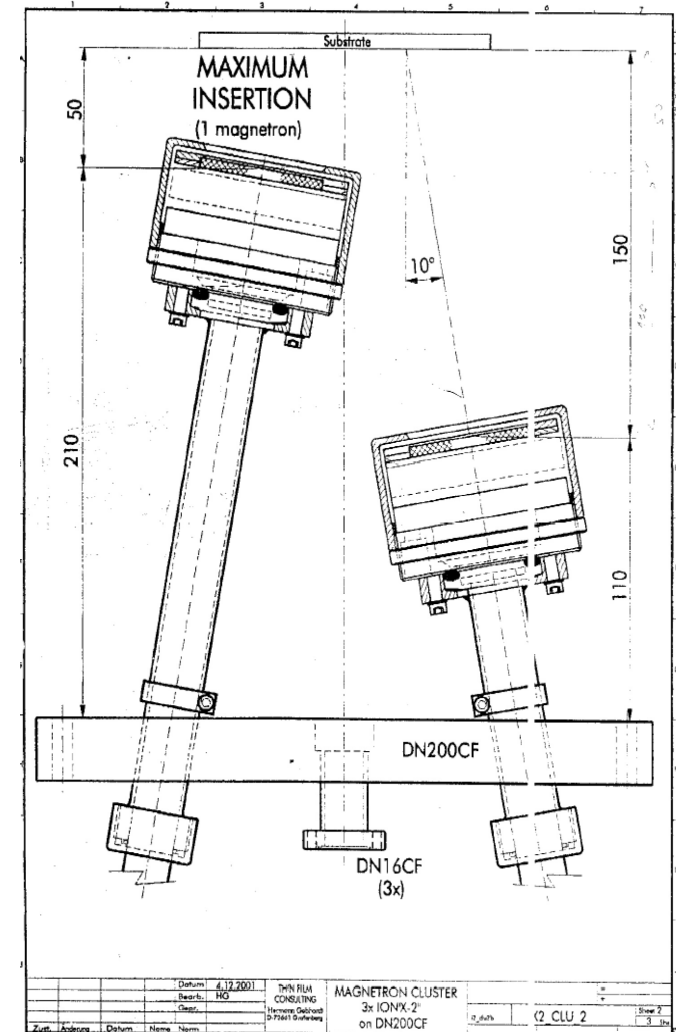

Depois...

Desenhar uma câmara de deposição para:

- 3 x 2” magnetrons planos para metais e óxidos ferromagnéticos, com uma geometria confocal para deposição sequencial e/ou co-deposição de filmes finos
- introdução de novas fontes PVD (térmica, laser, iónica)
- Desenhar todos os outros subsistemas:
  - medida da pressão
  - controlo gasoso (Ar, O_2)
  - controlo da temperatura dos substratos
  - arrefecimento dos magnetrons
  - electrónica de RF (adaptação de fase e impedância)

Hardware

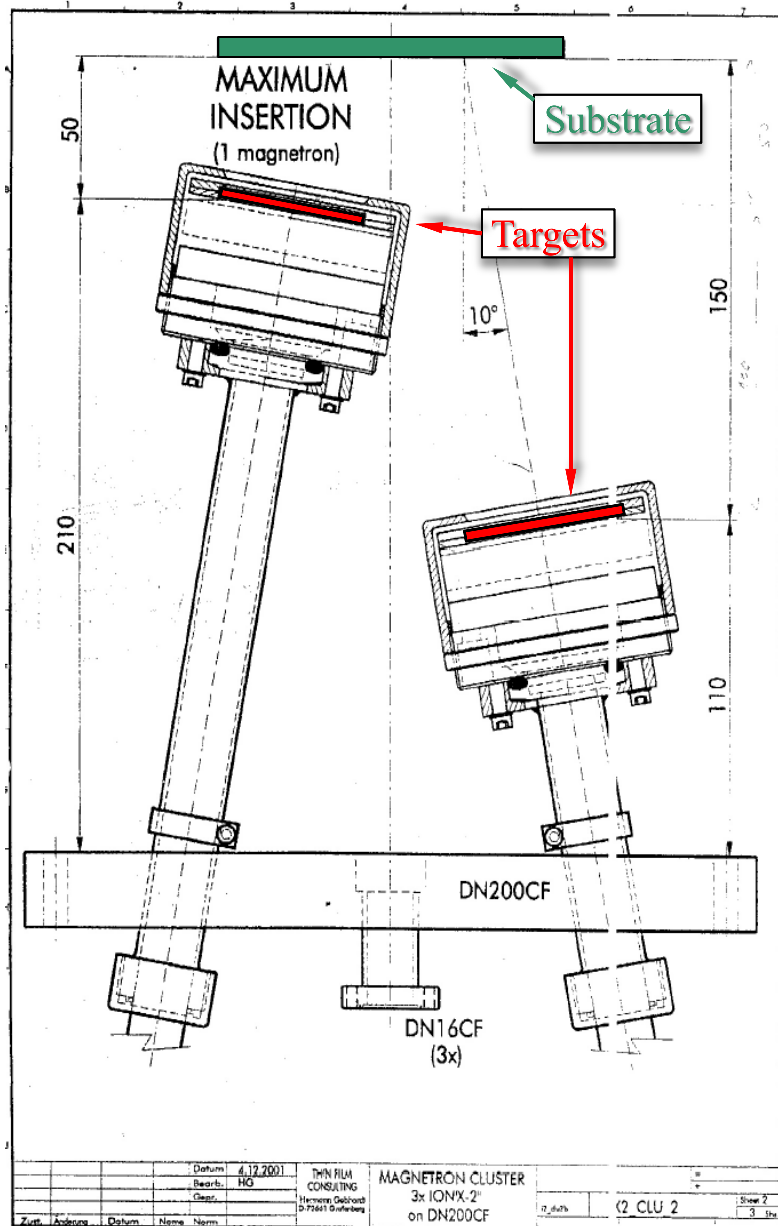

Especificações

Dimensões

- diâmetro 81 mm
- altura 56 mm

Alvo

- forma circular / plana
- diâmetro 2" = 50,8 ± 0,2 mm
- espessura 2 – 5 mm
- arrefecimento indirecto

Pressão de funcionamento

- limites $3\times10^{-3} - 10^{-1}$ mbar

Campo magnético

- NdFeB permanente

Temperatura

- Máxima 80 ºC

Taxas de deposição típicas

- Cu (300W DC): 15 $Å/s$ a 10 cm
- Al (300W DC): 8 $Å/s$ a 10 cm

Arrefecimento

- caudal mínimo 2,0 l/min
  3,0 l/min (P = 600W)

Hardware

Câmara de deposição

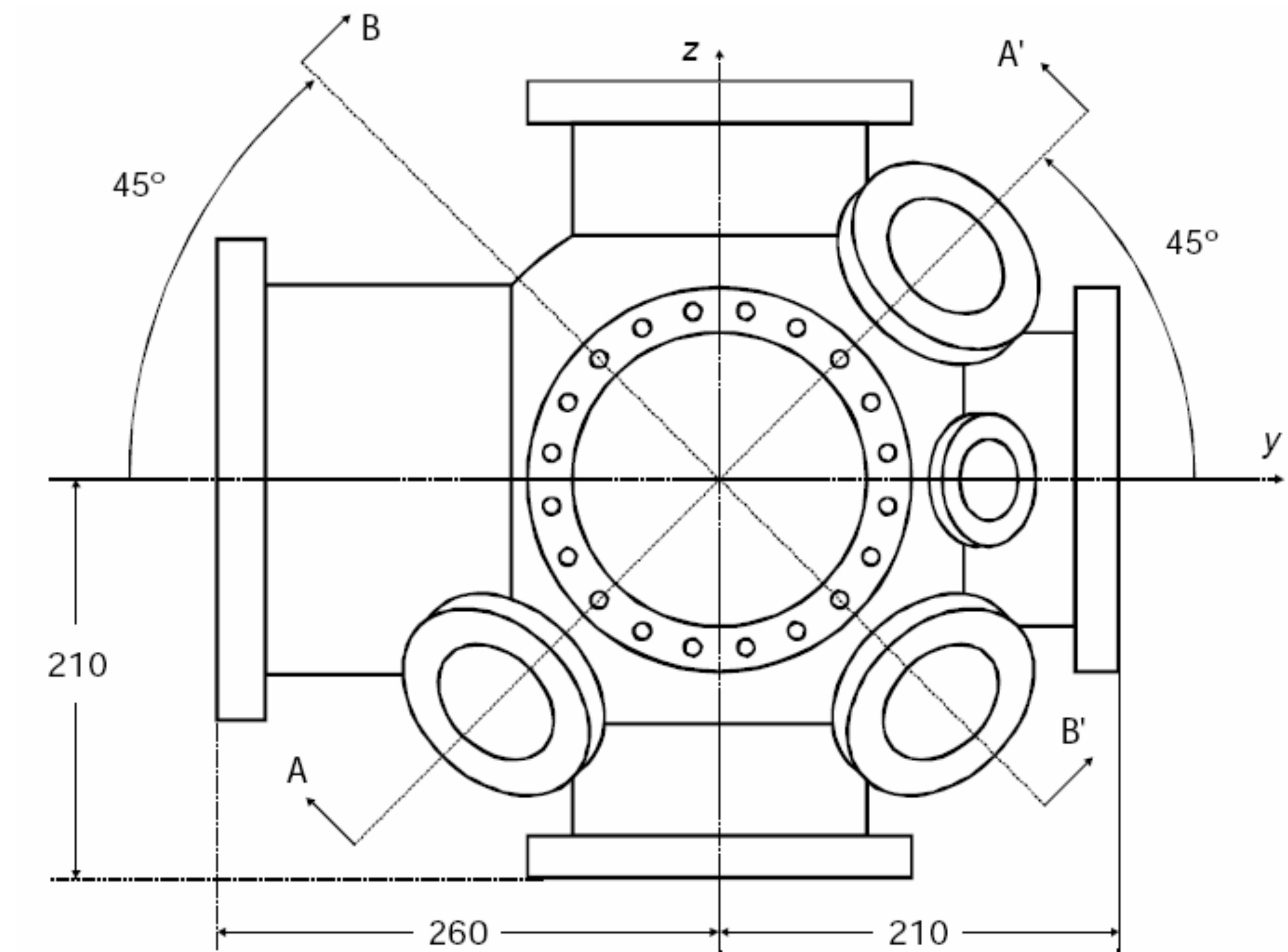

Hardware

Magnetrons

Três magnetrons em geometria confocal para a deposição sequential ou simultânea

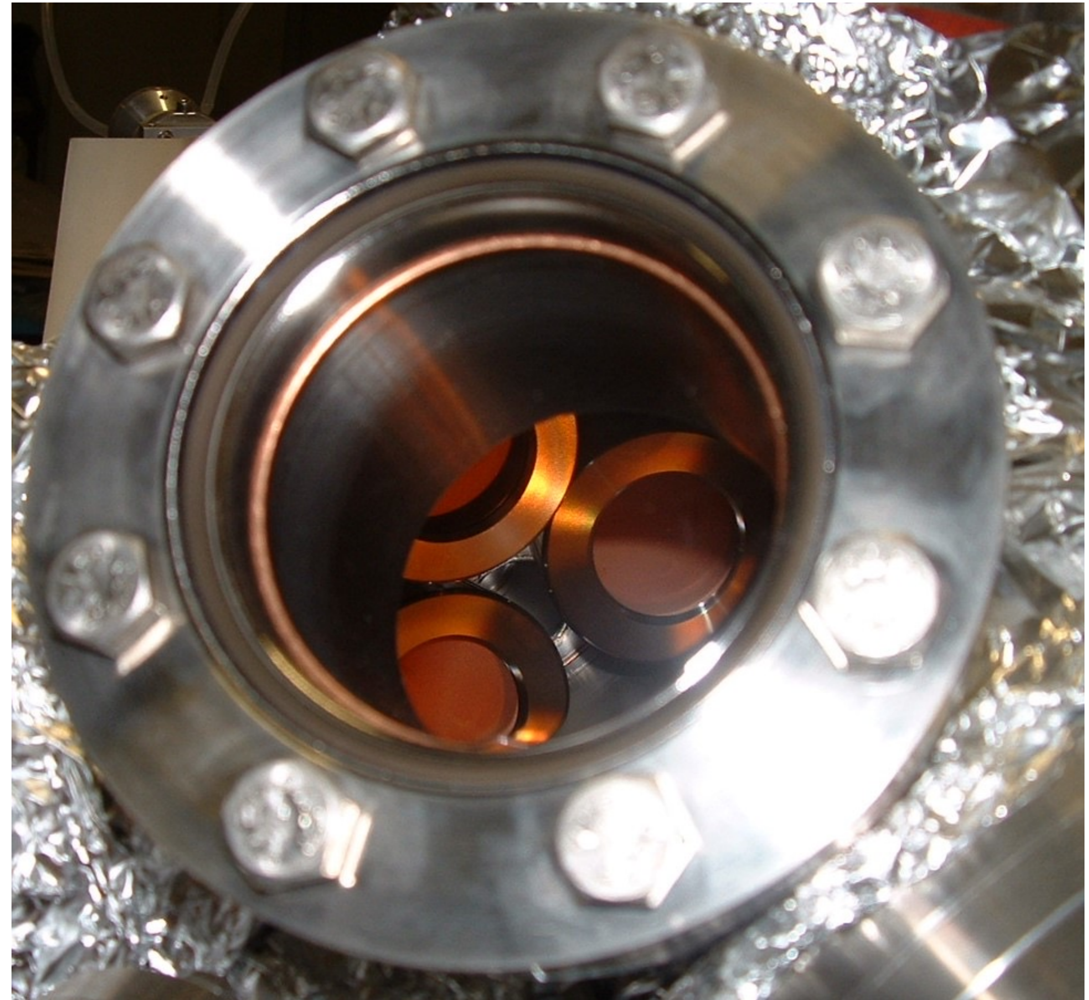

rf - Ionic sputtering

RF Sputtering – Codeposition

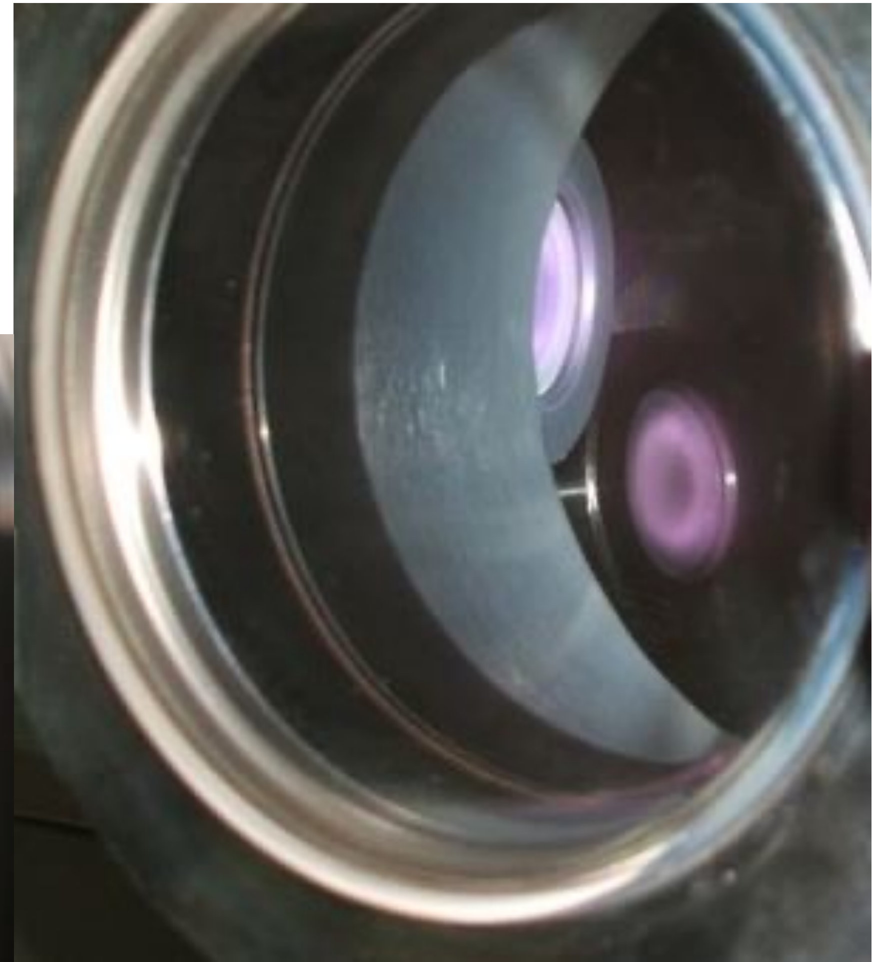

Hardware

Deposition chamber

Suporte para o aquecedor
Tubo em aco 304
diam: 5/8"=15,9 mm

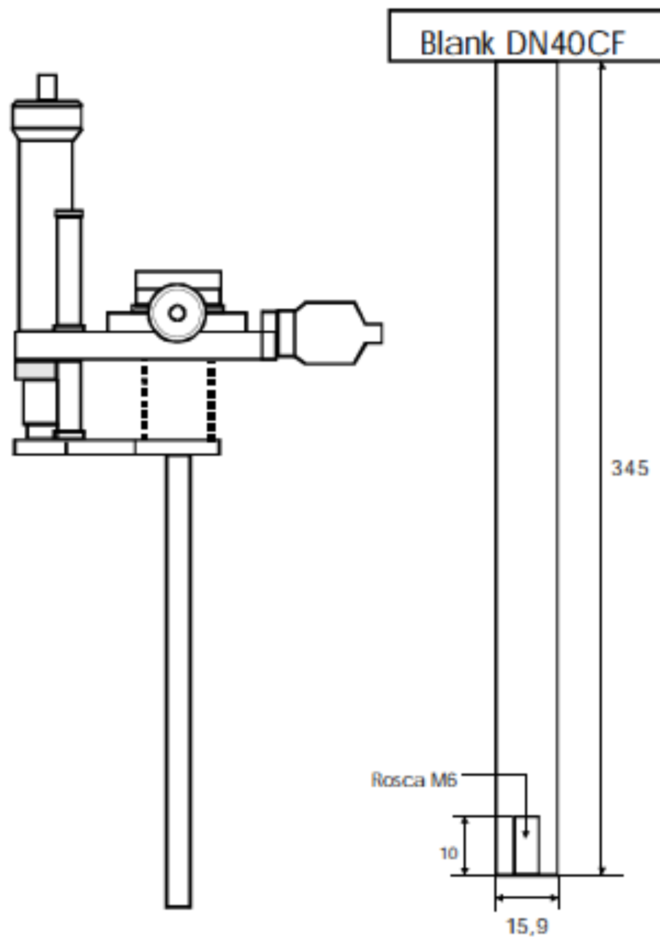

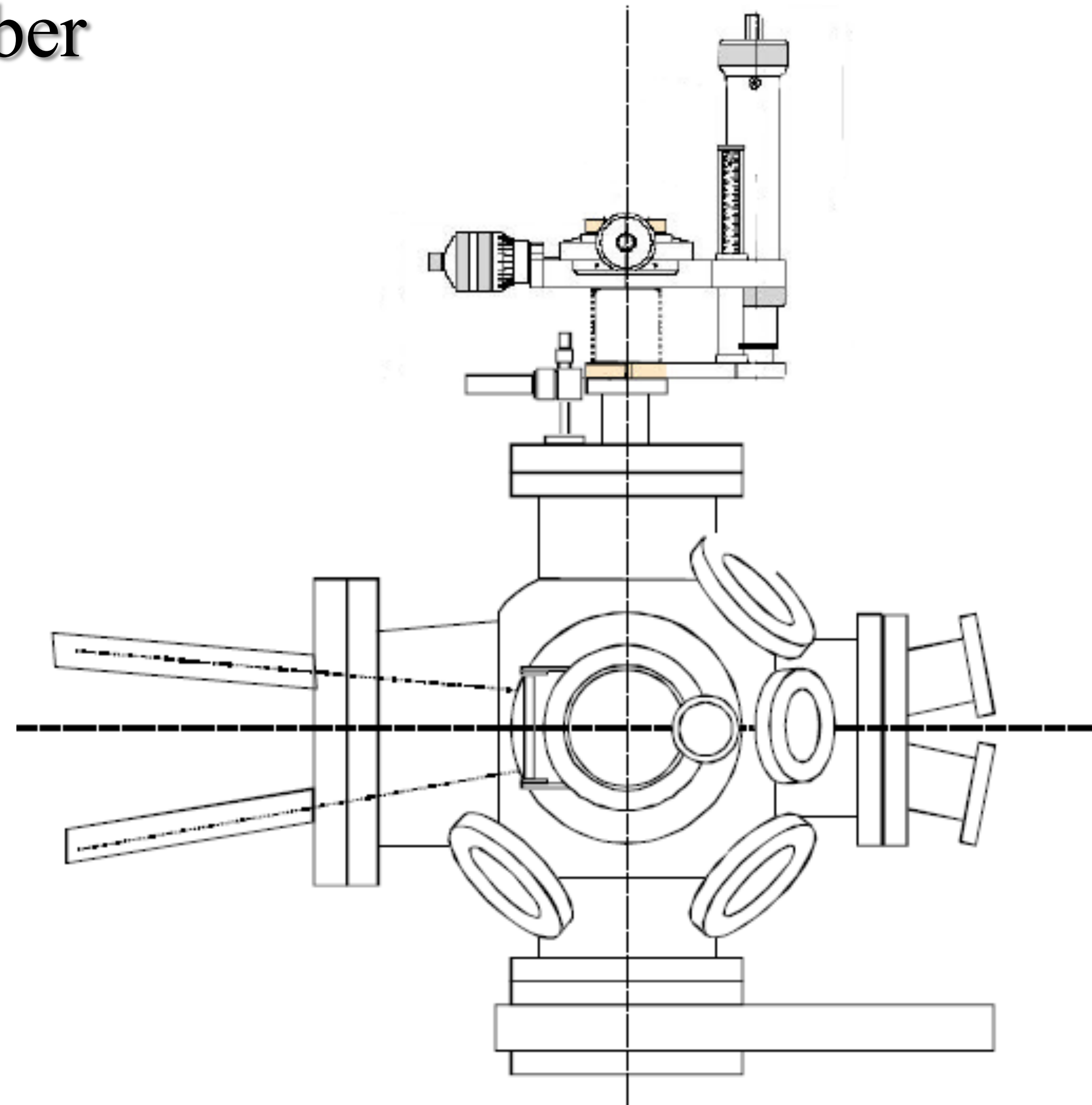

Hardware

Heater assembly

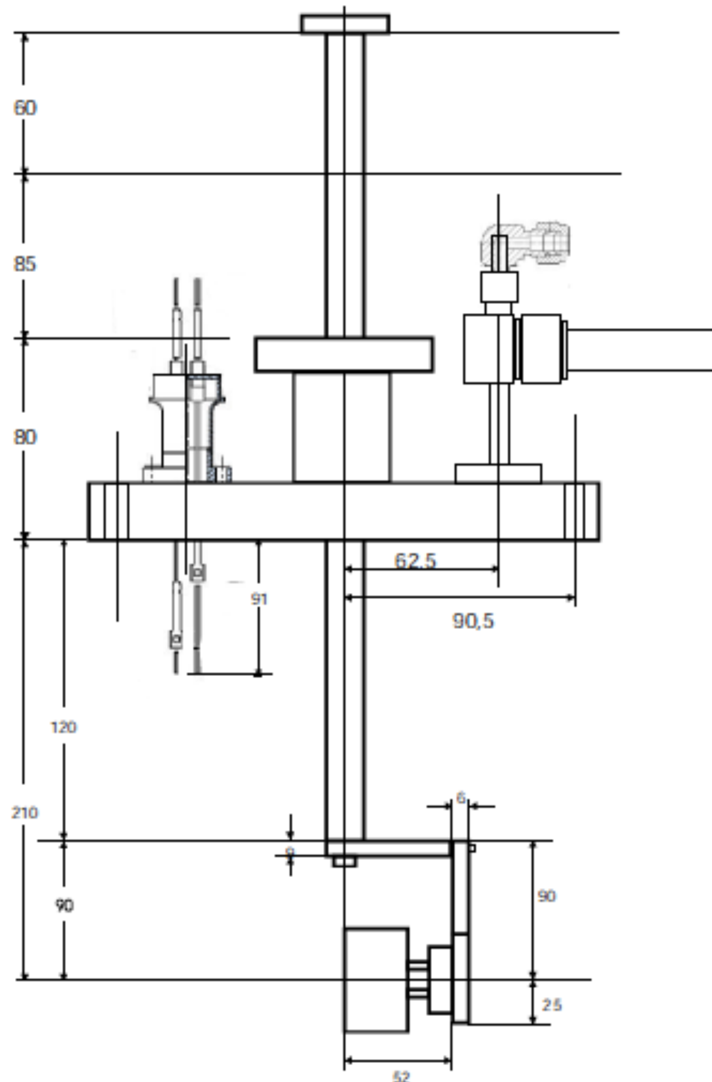

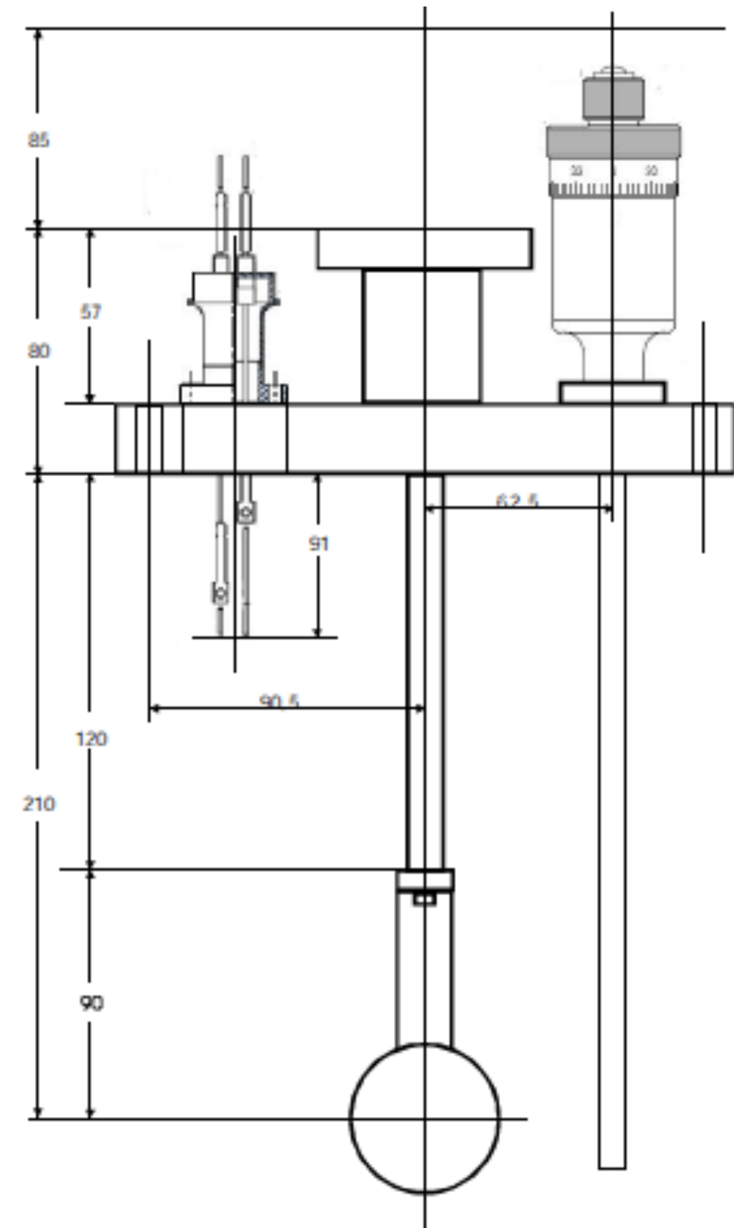

Hardware

Selagem de vácuo permanente – precisão ~ 1μm

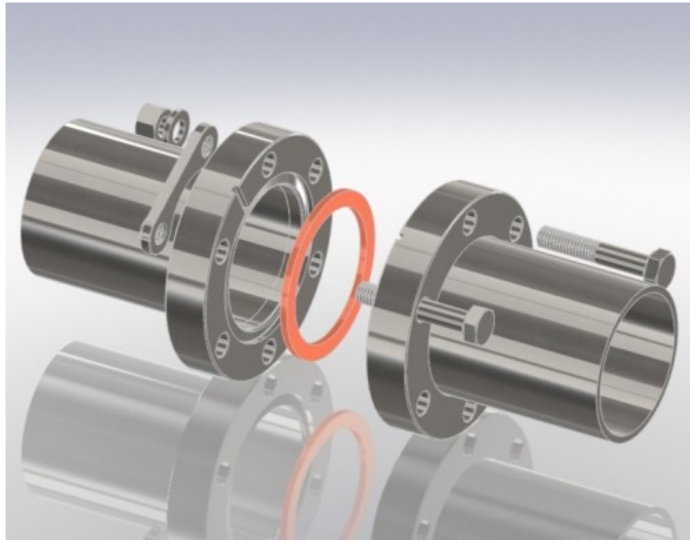

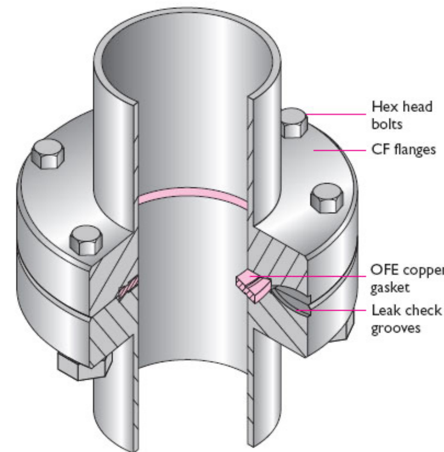

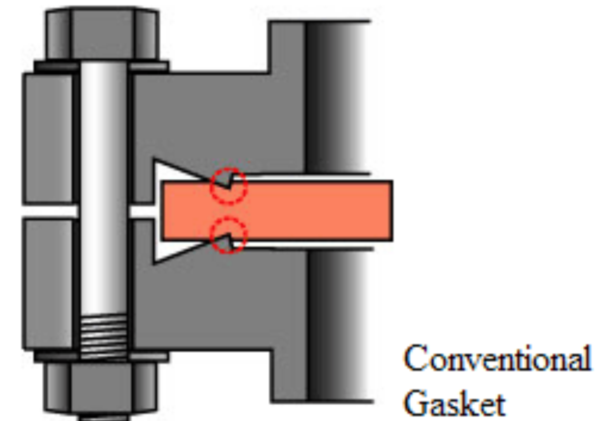

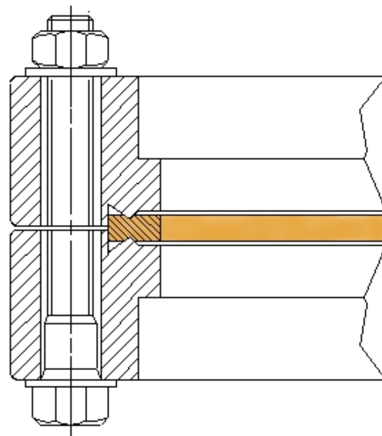

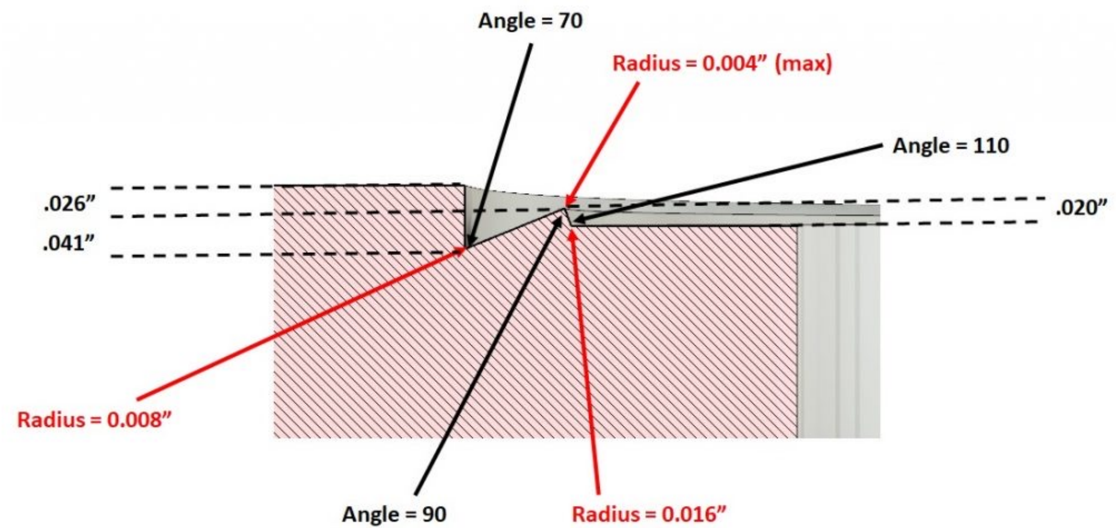

Hardware

Sistema de bombagem

convencional turbo-molecular + rotativa

$P_{atm} = 10^3 \rightarrow \ 10^{-8}$ mbar (10^{-2} Pa)

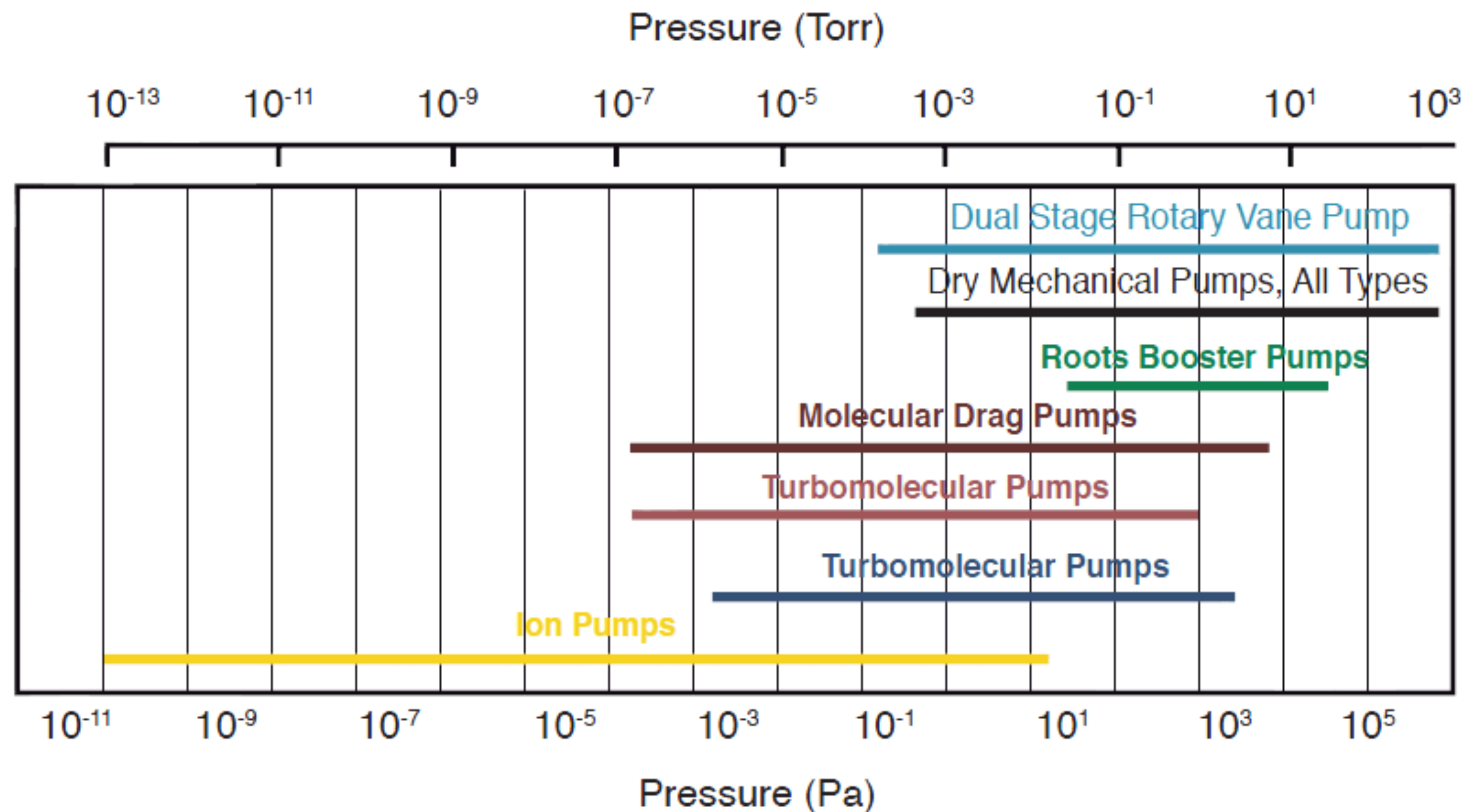

Hardware

Sensores de Pressão

Combinação de sensores para cobrir todo o intervalo de pressão pretendido $P_{atm} = 10^3 \rightarrow\ 10^{-10}$ mbar (1mbar = 1,33 Torr)

P_{atm}

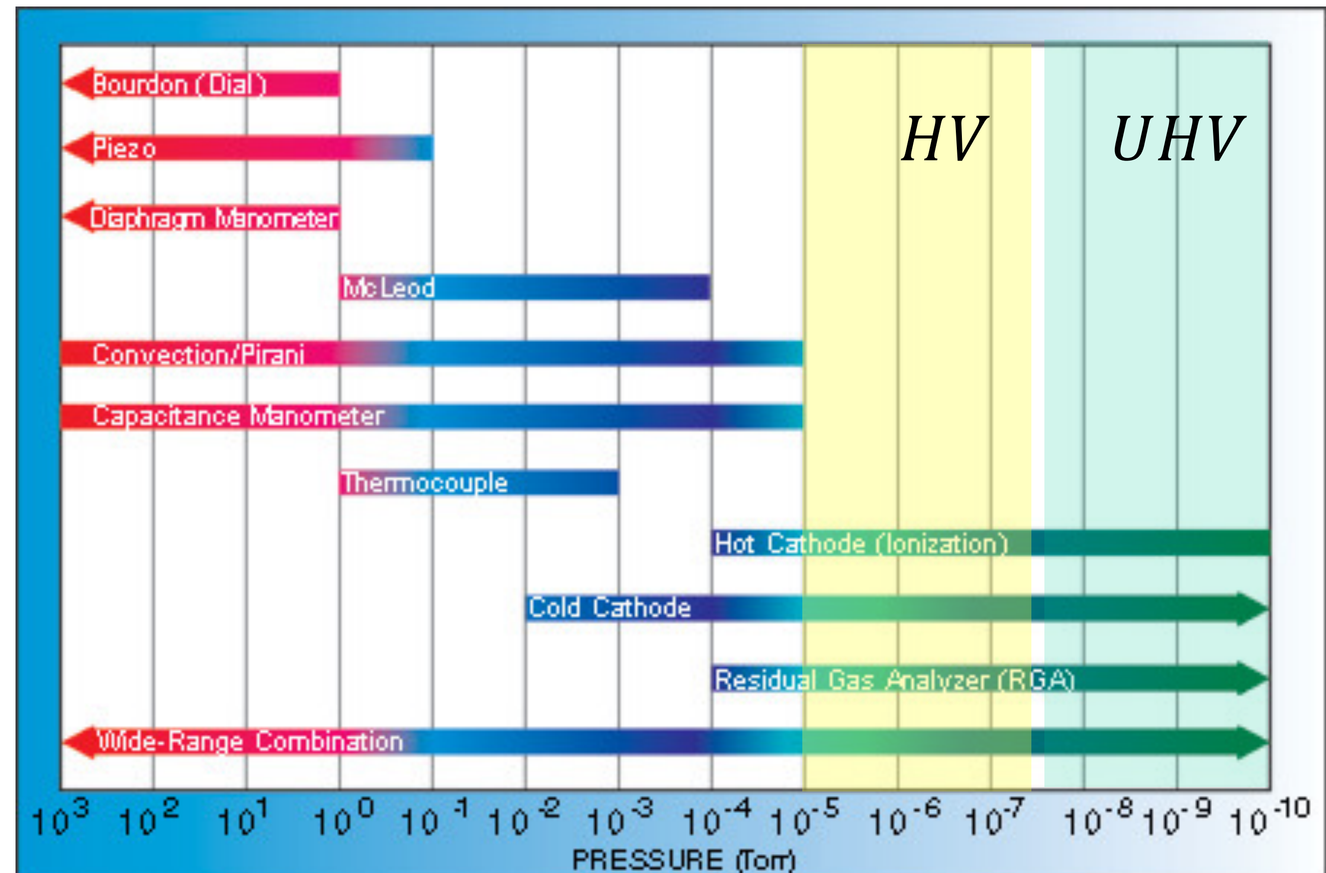

Hardware

Sensores de Pressão

Pirani

Hot cathode

Pirani
$10^3 - 1{,}3\times10^{-3}$ mbar

Hot cathode
$1{,}3\times10^{-2} - 1{,}3\times10^{-11}$ mbar

Hardware

RGA – Residual Gas Analizer

Analisador de Gases Residuais (RGA)

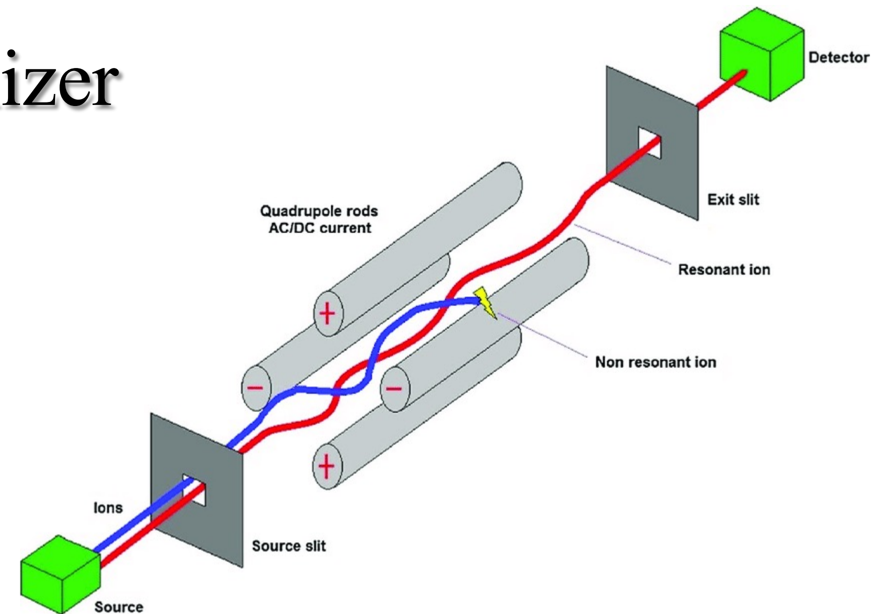

Um pequeno espectrómetro de massa quadrupolar (0-80 amu) monitoriza a composição da atmosfera residual, isto é, do vácuo, para detecção de fugas e/ou contaminações provenientes:

- da desgasificação dos componentes da câmara
- óleo da bomba rotativa
- juntas de selagem (flanges)

Intervalo de pressão de funcionamento

- $1\times10^{-3} - 1\times10^{-11}$ mbar

Hardware

Sensores de Pressão

Combinação de sensores para cobrir todo o intervalo de pressão pretendido $P_{atm} = 10^3 \rightarrow 10^{-10}$ mbar (1mbar = 1,33 Torr)

UHV (Ultra High Vaccum)
Neste regime o livre percurso médio λ das moléculas gasosas é maior que as dimensões da câmara L

$$\lambda = \frac{k_B T}{\sqrt{2}\pi d^2 p} \gg L$$

isto significa que o número de Knudssen é $K_n = \frac{\lambda}{L} \gg 1$

No nosso caso temos $L \approx 80$ cm e , portanto, será

$$p \ll 10^{-5} \text{ mbar}$$

Hardware

Sensores de Pressão

Escolha dos sensores

- Pressão de funcionamento

  intervalo de pressões que é necessário monitorar/controlar durante todo o processo (preparação, deposição e pós deposição)

- Presença de Ar e O2

  exceptuando os medidores de pressão total, é necessário calibrar os sensores para os gases (e misturas gasosas) utilizados durante todo o processo

- Gases reactivos

  podem ocorrer reacções químicas que afetam a medida da pressão e degradam o desempenho dos sensores ao longo do tempo

- Altas temperaturas

  interferência térmica nas medidas de pressão durante todo o processo

- Interferência electromagnética (13,56 MHz)

- Custo

Hardware

Desempenho

Tempo de bombagem e pressão mínima:
1,1 E-8 mbar (8,3 E-9 Torr) após 20 horas (sem "backing")

As linhas a vermelho representam simulações para os vários regimes de comportamento dos gases (neste caso ar)

- viscoso → $10^3 < P < 10^{-2}$
- intermédio → $10^{-2} < P < 10^{-7}$
- molecular → $P < 10^{-7}$

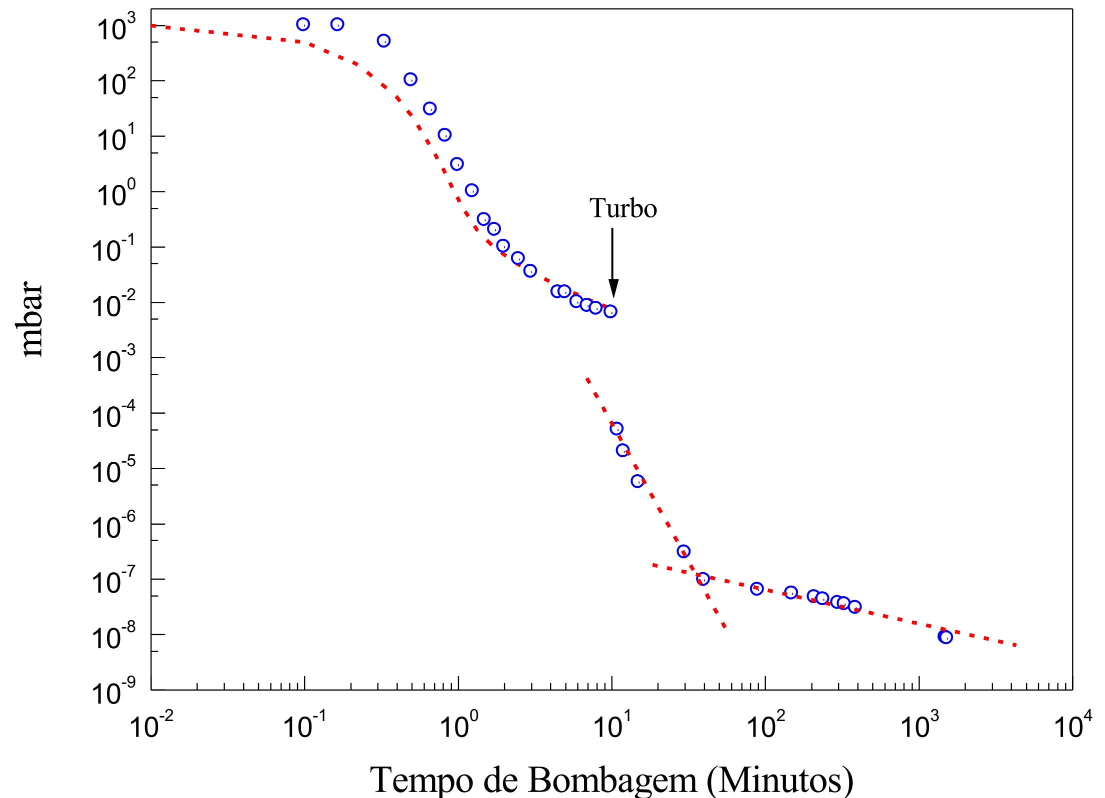

Hardware

Desempenho

Controlo da Pressão parcial de Ar e O_2

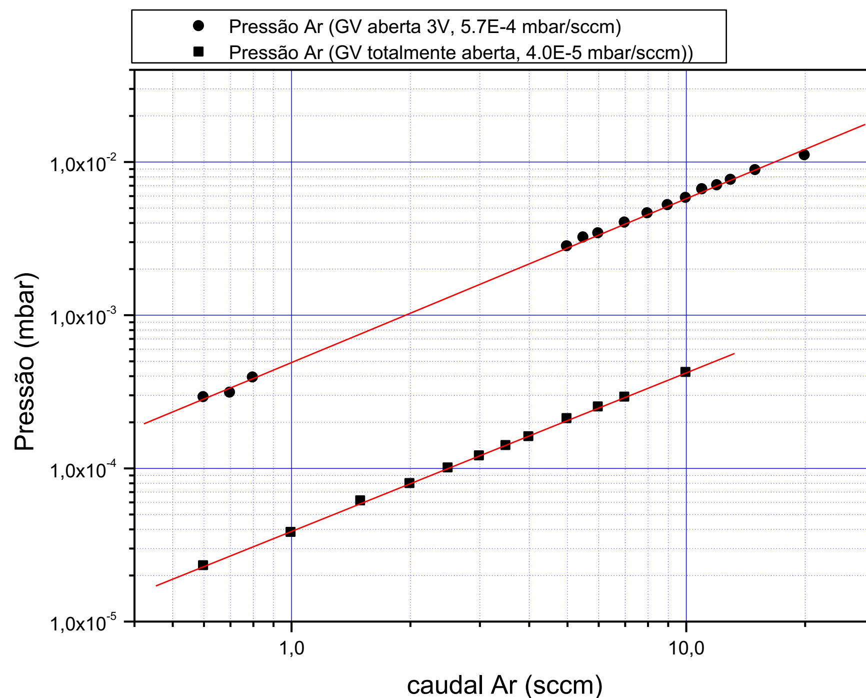

Hardware

Resistive heater

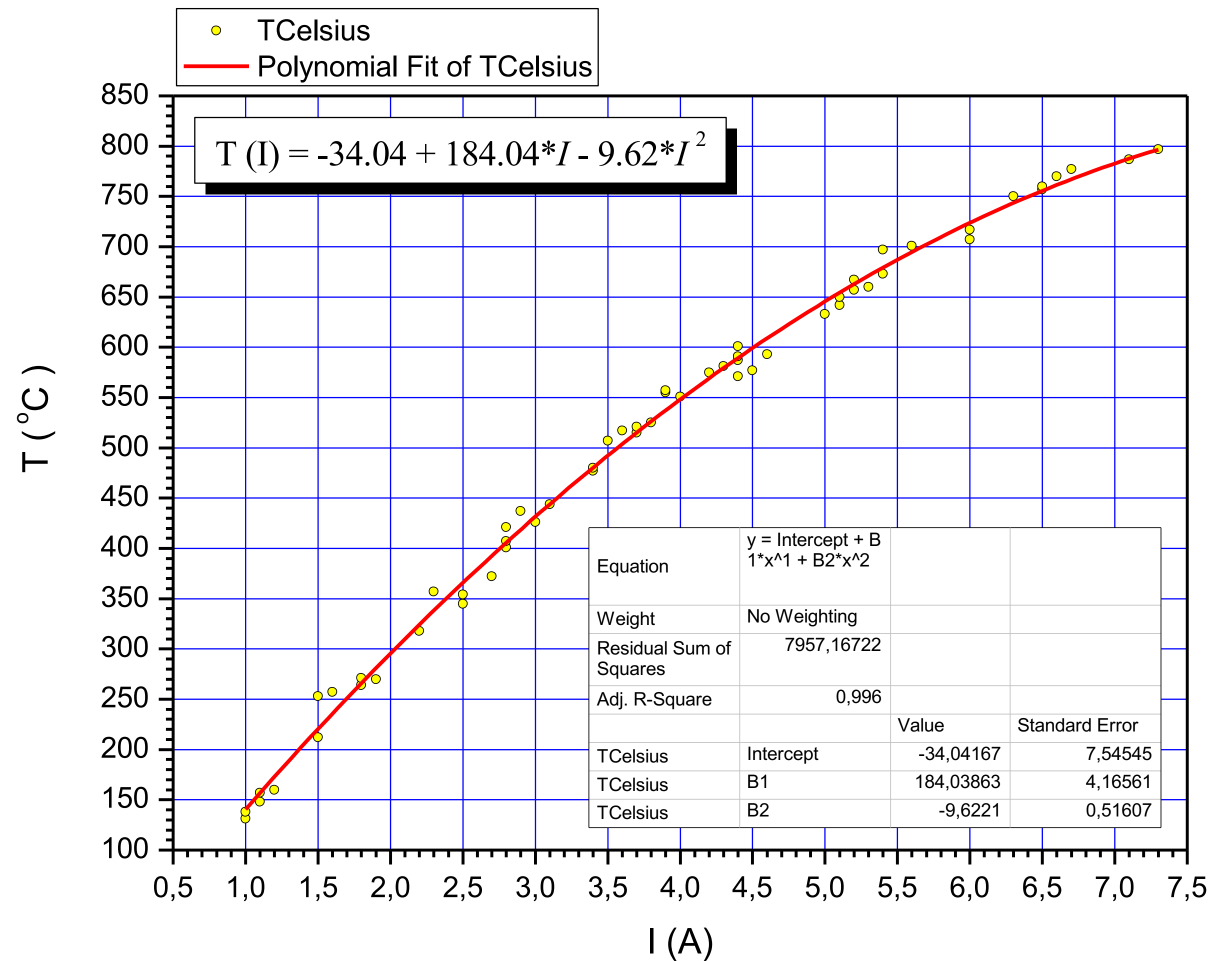

Temperature (in vacuum P < E-3 mbar)

Em estado estacionário o balanço de energia dá

$$\Delta T = T_h - T_s = T_h \left[1 - \left(\frac{\epsilon_h}{\epsilon_s + \epsilon_h}\right)^{\frac{1}{4}}\right]$$

$T_{\mathrm{h}} = 600$ ºC, $\Delta T = 140$ ºC !!!
(aquecedor metálico resistivo)

Muito importante:

- $\epsilon = \epsilon\,(\lambda)$ é a emissividade das superfícies
- O fluxo de calor é dado pela lei da radiação do corpo negro de Stefan-Boltzman

$$\Phi = n^2 \sigma T^4 \text{ (W/m}^2\text{)}.$$

- O índice de refracção do meio acima da superfície ≈ 1 para vapores < 1 atm.

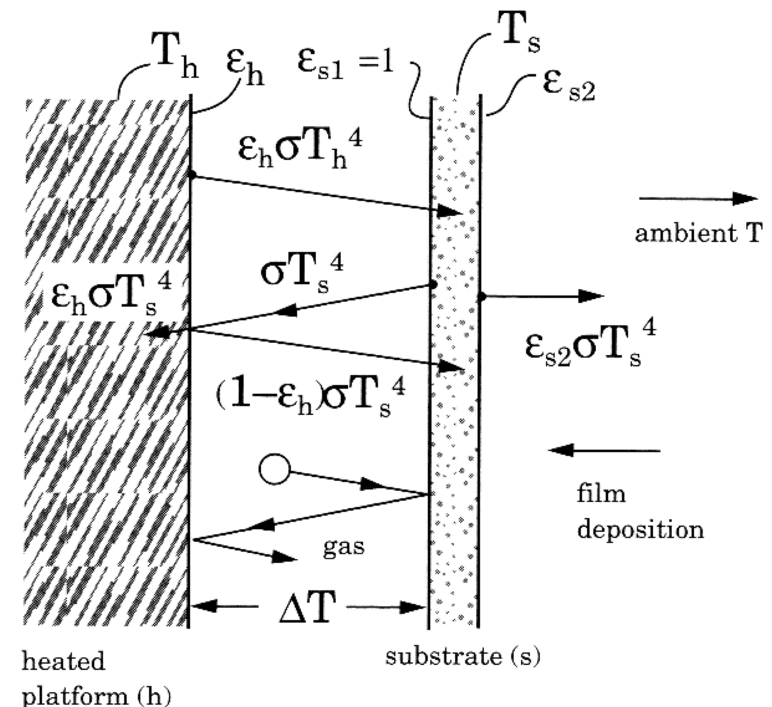

Figure 5.42 Geometry for radiative and gas-conductive heating of a substrate.

Donald L. Smith, *Thin-Film Deposition*, McGraw-Hill, Boston (Ma), USA, 1995.

Temperature (in vacuum *P* < E-3 mbar)

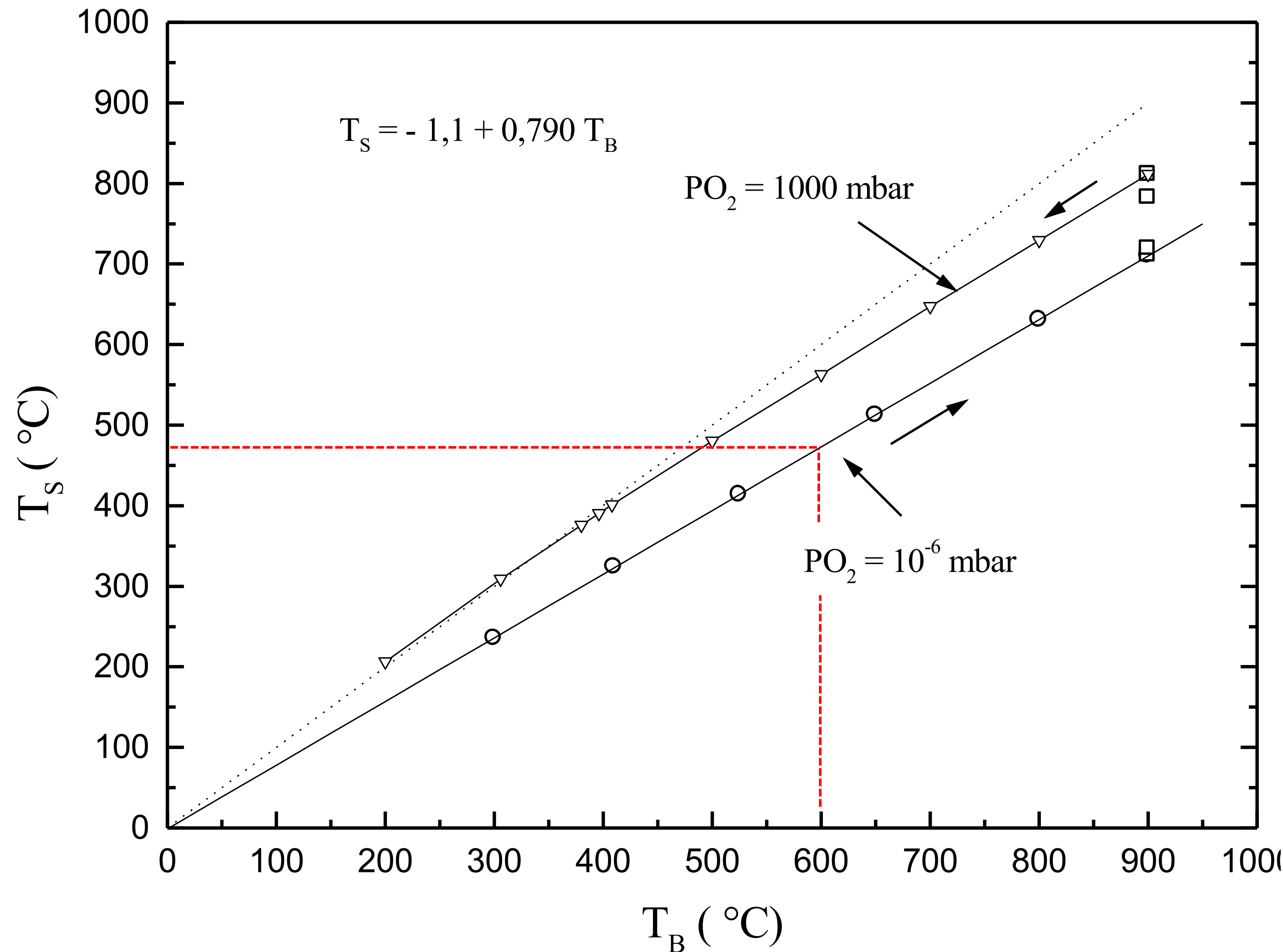

valores medidos: T_B = 600 ºC, Ts= 470 ºC, ΔT = 130 ºC, $PO_2 = 10^{-6}$ mbar

Subida da temperatura do substrato devida ao aumento da pressão de O_2 após a deposição, mantendo a temperatura do aquecedor constante e igual à temperatura de deposição → *"in-situ" annealing*